DRAG COEFFICIENTS WITH APPLICATIONS TO SATELLITE ORBITS

ANDREW SOWTER

Doctor of Philosophy

THE UNIVERSITY OF ASTON IN BIRMINGHAM

March 1989

The University of Aston in Birmingham

TITLE: Drag Coefficients with Applications to Satellite Orbits
AUTHOR: Andrew Sowter
DEGREE: Doctor of Philosophy
YEAR: 1989

THESIS SUMMARY:

In the last twenty or so years the results of theory and experiment have produced much information on the characteristics of gas-surface interactions relevant to a satellite in hyperthermal free-molecular flow. This thesis contains reviews of the rarefied gas dynamics applicable to satellites and has attempted to compare existing models of gas-surface interaction with contemporary knowledge of such systems. It is shown that a more natural approach would be to characterise the gas-surface interaction using the normal and tangential momentum accommodation coefficients, σ' and σ respectively, specifically in the form

$$\sigma = \text{constant} \quad , \quad \sigma' = \sigma'_o - \sigma'_1 \sec \xi_i$$

where ξ_i is the angle subtended between the incident flow and the surface normal and σ, σ'_o and σ'_1 are constants. Adopting these relationships, the effects of atmospheric lift on inclination, i, and atmospheric drag on the semi-major axis, a, and eccentricity, e, have been investigated. Applications to ANS-1 (1974-70A) show that the observed perturbation in i can be ascribed primarily to non-zero σ'_1 whilst perturbations in a and e produce constraint equations between the three parameters. The numerical results seem to imply that a good theoretical orbit is achieved despite a much lower drag coefficient than anticipated by earlier theories.

KEYWORDS:

Satellite Orbital Dynamics, Satellite Aerodynamics, Rarefied Gas Dynamics, Gas-Surface Interactions, Accommodation Coefficients

Dedication

This thesis is dedicated to the memory of my Father, the patience of my Mother and the enthusiasm and support of my supervisor, Dr. P. Moore.

Acknowledgement

I am very grateful to the University of Aston in Birmingham for providing the Research Studentship under which this work was done. I would also like to thank the GEC-Marconi Research Centre for providing the funds covering the typing of this thesis, and the Word Processing Group there for performing this, not inconsiderable, task.

List of Contents

List of Tables

List of Figures

CHAPTER 1
INTRODUCTION

For the last twenty years or so the field of satellite aerodynamics has been almost completely dominated by the results of only a handful of reports and papers generated during the enormous enthusiasm that followed in the wake of the first man-made satellites. The results of those papers have been used again and again in the refinement of satellite orbits and in the derivation of atmospheric densities at satellite altitudes.

The purpose of this thesis has been to review the field of satellite aerodynamics in the light of the last twenty or so years and to consider the problem in the light of experimental and theoretical studies conducted therein. The first task was to simply review the current status of gas dynamics relevant to satellites and to introduce the most common methods of describing the drag and lift forces on such a body in terms of widely accepted parameters. This is certainly true of Chapter 2 where the basic concepts of rarefied gas dynamics are introduced and contrasted with the most popular models of satellite aerodynamics. From this, we observe that the crucial link between the two fields lies in the parameterisation of the problem, particularly in the modelling of the interaction between the atmosphere and the surface of the satellite; models relevant to this problem, gleaned from contemporary references in surface science, are summarised in Chapter 3 and analytically extended to encompass momentum accommodation coefficients. The analytical models are shown to be incomplete and the numerical simulations, although more promising, are shown to lack the quantitative agreement with experiment. In Chapter 4 a new numerical simulation of the problem has been undertaken in an attempt to roughen the surface more than existing, greatly idealised, models, in an attempt to gain the quantitative agreement currently lacking. This was not achieved, although there still remained much agreement with the observed behaviour of the momentum accommodation coefficients with angle of incidence, thus further adding to the necessity to test the new parameterisation on the orbit of a real satellite.

In order to test the model on a real orbit, we must adapt the existing equations of orbital dynamics to encompass the new parameter. This is achieved in Chapter 5 for the particular case of a flat plate constantly orientated to a fixed position in the celestial sphere, such as the Sun. In Chapter 6, this is applied to the orbit of the Astronomical Netherlands Satellite ANS-1, particularly with respect to the variations of the semi-major axis, the eccentricity and the inclination of the satellite. Here, a full description of the ANS-1 platform geometry is encompassed in the modelling, including reductions in the area of certain portions of the body due to shadowing by other faces and panels of the incident gas stream. The results show that the parameterisation was successful in this case and has interesting implications on the values of drag coefficients for satellites.

The field of satellite aerodynamics is a multi-disciplinary subject as it covers the areas of rarefied gas dynamics, surface science, atmospheric modelling and, ultimately, satellite dynamics. In an attempt to form a coherent argument I have had to consider all of these topics and make no apologies for introducing concepts that may be unfamiliar to the orbital analyst. Indeed, it has all been necessary to describe one of the most difficult and interesting problems in satellite orbital dynamics.

CHAPTER 2
SATELLITE AERODYNAMICS

2.1 Introduction

2.1.1 The Satellite Environment

The atmosphere of the Earth extends to high altitudes, albeit at increasingly low densities as we move further into space. The structure of the lower atmosphere, say, below 80 km, is characterised by high densities and continuum flow. However, at altitudes greater than this, in a region called the Thermosphere [1,2], air density decreases rapidly with the negative exponential of altitude as given by the hydrostatic equation [45]

$$\frac{1}{\rho}\frac{\partial \rho}{\partial r} = -\frac{1}{H'} \qquad \text{..... (2.1)}$$

where ρ is air density, r is altitude above the Earth's surface and H is the density scale height. The atmosphere here may not simply be considered as a continuous medium but as a rarefied gas whose properties are determined by the trajectories of individual particles [1].

The temperature within the thermosphere increases with height due to the differential absorption of solar radiation until, at about 200 km, the temperature becomes independent of height. At such heights, the temperature has values between 600 K and 1200 K [45,3], dependent on the level of solar activity which varies over a near 11-year cycle.

Because of the very low densities encountered at such heights, an individual gas particle rarely collides with other particles and thus experiences a negligible amount of inter-molecular forces. For instance at round 600 km, the average distance travelled by a particle between collisions (the so-called mean free path) is of the order of tens of kilometres [1]. The gas-surface interaction between the individual atmospheric molecules and the satellite surface gives rise to aerodynamic forces that retard the motion, causing noticeable perturbations over long periods of time with the result that the satellite falls to lower and lower altitudes until re-entry is unavoidable. As re-entry only accounts for a very small proportion of a satellite's lifetime, this thesis will attempt to characterise the aerodynamics of an arbitrary body throughout the vast majority of its lifetime, that of a body moving through a highly rarefied gas.

2.1.2 Rarefied Gas Dynamics

In order to classify the particular flow regime about a body in a fluid, it is necessary to consider the rarefaction of the gas and the size of the satellite. This manifests itself in the dimensionless Knudsen number, where, if L is a typical length of the body,

$$Kn = \frac{\text{MEAN FREE PATH}}{\text{L}}. \qquad \text{..... (2.2)}$$

For Kn << 1 standard continuum flow is encountered but for Kn > 10 the gas is no longer a continuum but a highly rarefied and collisionless collection of molecules, and flow here is called free molecule. For intermediate values of Kn we fall into a transition regime where the characteristics of both extremes may be observed, depending on the configurations. Because of the higher rarefaction of the upper atmosphere, the overwhelming majority of satellites experience free-molecular flow, exceptions being those in exceedingly low orbits or of very large dimensions. For instance, the size of the American Space Shuttle means that free-molecular flow is encountered only at heights above 200 km, approximately [4]. In reality, the transition regime will not be clearly defined. For instance, if the surface temperature of the body in the gas is high, a cloud of particles re-emitted by the surface may hamper the aerodynamic characterisation. Indeed, Cook [14] suggests that the true requirement for free-molecular flow is

$$Kn \gg \frac{V_i}{V_r} \qquad \text{..... (2.3)}$$

where V_i and V_r are the average speed of the particles incident and reflected by the surface respectively.

For a molecular gas in a Cartesian coordinate system (x, y, z) where the molecular velocity is given by $\mathbf{c} = (c_1, c_2, c_3)$, experiencing a force per unit mass of (X, Y, Z), we can define the distribution function of the gas, F, by declaring that the number of molecules with velocities between (c_1, c_2, c_3) and $(c_1 + dc_1, c_2 + dc_2, c_3 + dc_3)$ is dN, where:

$$dN = F\,dc_1 dc_2 dc_3. \qquad \text{..... (2.4)}$$

For a body experiencing free-molecular flow through a uniform gas in equilibrium F is a Maxwellian distribution function of the form [5]

$$F = n(2\pi RT)^{-\frac{3}{2}} \exp\{-(\mathbf{c}-\mathbf{V})^2/2RT\} \qquad \text{..... (2.5)}$$

where n is the number density of the gas, T is its temperature, V is the velocity of the gas relative to the satellite (the macroscopic velocity) and R is the universal gas constant given by R=8.31 JK^{-1} mol^{-1}.

Consider the coordinate system in Figure 2.1 for a gas striking a unit elemental surface.

Here, the distribution function is given by

$$F = n(2\pi RT)^{-\frac{3}{2}} \exp\{-[(c_1 - V\cos\xi)^2 + (c_2 + V\sin\xi)^2 + c_3^2]/2RT\}, \quad \text{..... (2.6)}$$

For any flux quantity Q = Q(c_1, c_2, c_3), we can find the total flux, $\overline{Q}$, on the surface per unit time where [6]

$$\overline{Q} = \int_0^\infty \int_{-\infty}^\infty \int_{-\infty}^\infty Q c_1 F dc_1 dc_2 dc_3. \quad \text{..... (2.7)}$$

The most important quantities concerning us are the normal momentum (i.e. along x_1) given by mc_1, where m is the mass of the gas molecule, and the tangential momentum (i.e. along x_2) given by mc_2. Hence, the total normal momentum, p_i, and the total tangential momentum, τ_i, striking our surface per unit time are found by replacing Q by mc_1 and mc_2 respectively. Hence, if $\rho = nm$ is the mass density of the gas, then

$$\begin{aligned} p_i &= \int_0^\infty \int_{-\infty}^\infty \int_{-\infty}^\infty mc_1^2 F dc_1 dc_2 dc_3 \\ &= \frac{\rho RT}{\pi^{\frac{1}{2}}} \{ s\cos\xi e^{-s^2\cos^2\xi} + \\ &\quad + \pi^{\frac{1}{2}} \left(\frac{1}{2} + s^2\cos^2\xi \right) [1 + erf(s\cos\xi)] \} \quad \text{..... (2.8)} \\ \tau_i &= \int_0^\infty \int_{-\infty}^\infty \int_{-\infty}^\infty mc_1 c_2 F dc_1 dc_2 dc_3 \\ &= \rho V \sin\xi \left(\frac{RT}{2\pi} \right)^{\frac{1}{2}} \left\{ e^{-s^2\cos^2\xi} + \pi^{\frac{1}{2}} s\cos\xi [1 + erf(s\cos\xi)] \right\} \end{aligned}$$

where

$$erf(x) = \frac{2}{\pi^{\frac{1}{2}}} \int_0^x e^{-t^2} dt$$

and s is the speed ratio, defined as the ratio between the macroscopic and the mean thermal velocities of the gas, and is given by

$$s = \frac{V}{\sqrt{2RT}}. \quad \text{..... (2.9)}$$

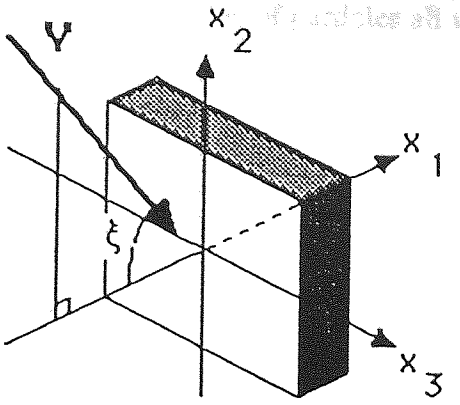

Figure 2.1 Coordinate system for a gas particle striking an elemental surface

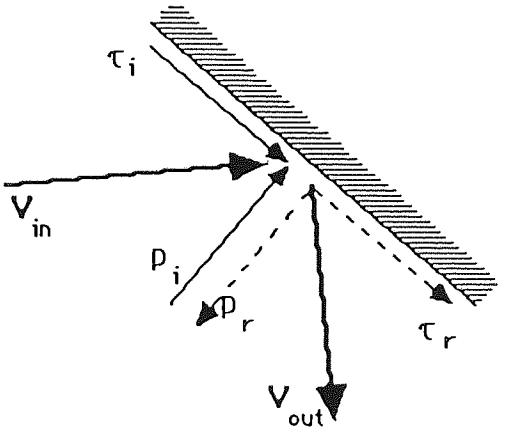

Figure 2.2 Incidental and reflected momentum components

As $s \to \infty$ (hyperthermal flow) we find that we can ignore the thermal velocity and consider the gas as a collection of particles all with velocity V. Hence, in hyperthermal flow,

$$p_i = \rho V^2 \cos^2 \xi, \qquad \text{..... (2.10)}$$

$$\tau_i = \rho V^2 \sin \xi \cos \xi.$$

For a satellite, the speed ratio is large, typically 10 [5], (although this is subject to large variations due to temperature fluctuations in the thermosphere [4]), and the hyperthermal approximation becomes very useful in simplifying the equations involved. Indeed, it is almost universally the sole consideration for calculating satellite drag coefficients. However, there is a range of values of $s \cos \xi$ for which the simplified Equation (2.10) cannot be applied [7] and thus, when considering flow over a body, hyperthermal flow is only really useful when the regions for which $s \cos \xi < 1$ are relatively small.

So far, we have been concerned with identifying the characteristics of the gas dynamics encountered by a satellite in a free-molecular gas stream, and have successfully achieved this in terms of known properties of the incident stream, e.g. speed ratio, temperature etc. However, if we are to proceed further to derive the force on such a body, we will require a knowledge of the mechanism describing what happens when a high velocity particle strikes a solid surface.

The parameterisation of the gas surface interaction required to derive the force on a body in terms of easily utilised coefficients has been the subject of much debate; for the case of satellites, a parameterisation based on the thermal transfer at a surface is usually adopted, whereas the gas dynamicists prefer a more direct method based on momentum transfer. Whichever system is adopted, the normal momentum, p_r, and the tangential momentum, τ_r, of the reflected gas atoms per unit time are then calculated so that the momentum transfer and hence force on the surface can be calculated. If p is the normal momentum transfer and τ the tangential momentum transfer on our elemental surface (i.e. lost to the surface), then considering Figure 2.2,

$$p = p_i + p_r, \qquad \text{..... (2.11)}$$

$$\tau = \tau_i - \tau_r.$$

If F_D is the drag force, and F_L the lift force on our surface, then, according to Figure 2.3

$$F_D = p\cos\xi + \tau\sin\xi, \qquad \text{..... (2.12)}$$

$$F_L = -p\sin\xi + \tau\cos\xi.$$

Hence the forces on a body with total surface area A are given by

$$\overline{F}_D = \int_A F_D dA,$$

$$\overline{F}_L = \int_A F_L dA \qquad \text{..... (2.13)}$$

where, for a complex body, the lift direction will require further definition. In the case of hyperthermal flow, there will be no gas striking any surface turned away from the stream and so the integration in (2.13) will be over that portion of the surface turned towards the stream.

2.2 Accommodation Coefficients

In considering the scattering of a gas particle from a solid surface, we will assume that there is no chemical reaction between the two and hence assume that mass is conserved in the reaction. Also, we will assume that the gas particle is always re-emitted into the atmosphere, albeit at some microscopically later date. We will assume the convention of Figure 2.4, where the gas particle has mass m, strikes the surface at an angle of incidence ξ_i with velocity V_i and is reflected at an angle of reflection ξ_r with velocity V_r. The angles here are measured with respect to the surface normal, **n**. (See Figure 2.4).

When Maxwell [8] first considered the problem of gas-surface interactions in the last century he suggested that there were two extreme forms of reflection: Specular and Diffuse reflection.

Specular reflection is simply the case when the gas particle's characteristics are unchanged after reflection, except that it has reversed its normal velocity component away from the surface (i.e. $V_r = V_i$ and $\xi_r = \xi_i$).

In Diffuse reflection, the particle is completely absorbed by the surface only to be released back in thermal equilibrium with the surface at some random angle of reflection (i.e. the mean value of V_r is $(2RT_s)^{1/2}$ where T_s is the temperature of the surface and the mean ξ_r is 0°).

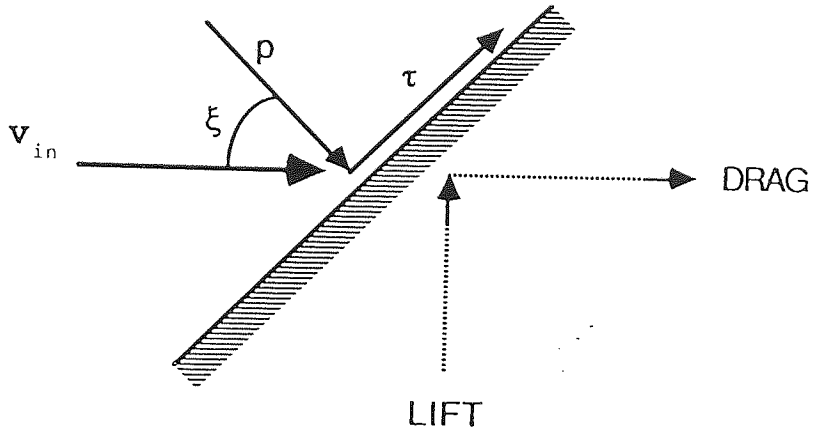

Figure 2.3 Drag and lift directions on a flat plate

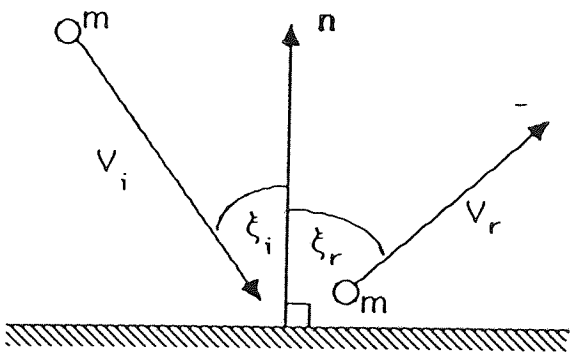

Figure 2.4 Coordinates of incident and reflected particle

Maxwell then postulated that we can approximate a gas-surface interaction by considering that a proportion, σ, of the reflected atoms reflected per unit time will be diffusely reflected, the remainder being specularly reflected. Hence, if we are measuring a flux quantity q, where q_i is its incident value and q_w is the value of q measured in thermal equilibrium with the wall per unit time, then

$$q_r = (1-\sigma)q_i + \sigma q_w \qquad \text{..... (2.14)}$$

where

$$0 \le \sigma \le 1$$

We see that $\sigma = 1$ is purely Diffuse reflection, whereas $\sigma = 0$ is Specular reflection.

It is highly unlikely that, in reality, a reflected beam would actually be divided as proposed. In fact, values of σ appear to depend exactly on what the quantity q is. However, we can formally introduce the accommodation coefficient, Σ, associated with a scalar flux quantity q, as

$$\Sigma = \frac{q_i - q_r}{q_i - q_w} \qquad \text{..... (2.15)}$$

where we place no restrictions on the possible range of values of Σ unless q is specified.

By far the most important accommodation coefficients are the normal and tangential momentum accommodation coefficients, σ' and σ respectively [9], and the thermal energy accommodation coefficient, α, where, if p is the component of momentum normal to the surface, τ is its tangential component, and E its kinetic energy, then

$$\alpha = \frac{E_i - E_r}{E_i - E_w},$$

$$\sigma' = \frac{p_i - p_r}{p_i - p_w}, \qquad \text{..... (2.16)}$$

$$\sigma = \frac{\tau_i - \tau_r}{\tau_i - \tau_w} \quad (\tau_w = 0),$$

where

$$E_w = 2\rho RT_s,$$

$$p_w = \frac{1}{2}\rho(2\pi RT_s)^{\frac{1}{2}}$$

and ρ is the mass density of the gas.

Thus, since σ and σ' describe completely the momentum exchange at our surface, we can derive the force on our satellite in terms of these two accommodation coefficients using Equations (2.8) and (2.11). Indeed, for a flat plate of unit area [9]

$$p = \frac{\rho V^2}{2s^2}\left[\left(\frac{2-\sigma'}{\sqrt{\pi}} s\cos\xi_i + \frac{\sigma'}{2}\sqrt{\frac{T_s}{T}}\right) e^{-s^2\cos^2\xi_i} + \{(2-\sigma')\left[s^2\cos^2\xi_i + \frac{1}{2}\right] + \frac{\sigma'}{2}\sqrt{\pi\frac{T_s}{T}}\ s\cos\xi_i\}\,[1 + erf(s\cos\xi_i)]\right],$$

$$\tau = \frac{\sigma\rho V^2 \sin\xi_i}{2\sqrt{\pi}s}\left\{e^{-s^2\cos^2\xi_i} + \sqrt{\pi}\, s\cos\xi_i\,[1 + erf(s\cos\xi_i)]\right\} \qquad \text{..... (2.17)}$$

and hence we may derive the drag and lift forces F_D and F_L on a flat plate.

The hyperthermal approximation, where we let $s\cos\xi \to \infty$, is very useful both in simplifying the equations and for later comparisons with other models. Thus, in hyperthermal molecular flow on a flat plate of area A, using Equations (2.12),

$$F_D = \sigma A\rho V^2\cos\xi_i + A\rho V^2(2-\sigma'-\sigma)\cos^3\xi_i, \qquad \text{..... (2.18)}$$

$$F_L = -A\rho V^2(2-\sigma'-\sigma)\cos^2\xi_i\sin\xi_i,$$

and if we define the drag and lift coefficients, C_D and C_L respectively, by

$$F_D = \frac{1}{2}\rho V^2 A' C_D,$$

$$\text{..... (2.19)}$$

$$F_L = -\frac{1}{2}\rho V^2 A' C_L,$$

where $A' = A\cos\xi_i$ is the cross-sectional area, then

$$C_D = 2[\sigma + (2-\sigma'-\sigma)\cos^2\xi_i], \qquad \text{..... (2.20)}$$

$$C_L = 2(2-\sigma'-\sigma)\cos\xi_i\sin\xi_i.$$

If we further assume that the coefficients σ' and σ are constant over all angles of incidence, then the drag coefficient for a sphere is given by:

$$C_{D_{\text{SPHERE}}} = 2 - \sigma' + \sigma. \qquad \text{..... (2.21)}$$

In retrospect we can say, since σ' and σ so completely describe the forces on a satellite, that a study of the momentum accommodation coefficients is all that is required to understand the problems of free-molecular flow for Earth satellites. However, the almost total predominance of the thermal energy accommodation coefficient, α, is due almost entirely to historical timing than any physical necessity.

The concept of a "thermal accommodation coefficient" was first introduced by Smoluchowski [10] in 1898 and further enhanced by Knudsen [11] in 1911 to parameterise the heat transfer between a gas and a solid surface. Heat transfer is a much studied phenomenon, and thus α became a familiar piece of notation in the world of physics.

In 1957 the first artificial satellite was launched, and the subsequent wealth of orbital data obtained excited scientists keen to exploit the potential of such knowledge. In 1959 Schamberg [12] introduced a model of gas-surface interaction that was not only capable of using the thermal accommodation coefficient, but also discussed the scattered distribution of the gas atoms which is of great interest to surface scientists. Other attempts to study the scattered distribution, such as Nocilla [13] in 1963, which is discussed later, have fallen against the almost universal acceptance of Schamberg's model for satellite considerations.

Although momentum transfer at a surface was originally modelled by Maxwell [8], the experimental difficulties involved in measuring σ' and σ set back a full study until 1958, with Schaaf and Chambré's [9] work on the flow of Rarefied Gases. However, because of its use of α and its form of the scattered distribution, Schamberg's model has been by far the most accepted model of gas-surface interaction for satellite purposes.

2.3 Schamberg's Model for the Scattered Distribution of Gas Particles from a Solid Surface

Consider a body in hyperthermal free-molecular flow, where, on an elemental unit surface, each particle strikes the solid with velocity V_i, making an angle θ_i with the surface. After interaction, Schamberg [12] proposed that the gas particles are re-emitted with the velocity V_r in a conical beam of half-angle width φ_o about a mean axis which makes an angle of θ_r with the solid surface (see Figure 2.5).

The angular distribution of the reflected particles obeys Knudsen's cosine law where the number of particles, dN_r, emitted per unit time between angles φ and $\varphi + d\varphi$ is given by

$$dN_r = K\cos\left(\frac{\pi}{2}\cdot\frac{\phi}{\phi_o}\right)d\phi. \qquad \text{..... (2.22)}$$

Since we assume continuity, K can be derived from

$$N_i = \int dN_r \qquad \text{..... (2.23)}$$

where the integration is over the re-emitted beam. Further, N_i is the total number of particles striking the surface per unit time, given by

$$N_i = n_i V_i \sin\theta_i \qquad \text{..... (2.24)}$$

n_i being the number density of the incident gas.

Schamberg considered three types of beam: a linear beam ($\varphi_o = 0$), a wedge-shaped beam where the scattered particles are simply scattered in the same plane as the incident particles and the surface normal, and a conical three-dimensional beam. Here we will consider only the three-dimensional case as it is the most widely accepted, whence

$$K = \frac{N_i}{2\pi}\cdot\frac{1-\left(\frac{\pi}{2\phi_o}\right)^2}{1-\left(\frac{\pi}{2\phi_o}\right)\sin\phi_o}. \qquad \text{..... (2.25)}$$

The angle of reflection θ_r is related to the angle of incidence θ_i by the parameter υ, where

$$\cos\theta_r = (\cos\theta_i)^{\upsilon} \qquad \text{..... (2.26)}$$

The thermal energy accommodation coefficient was defined earlier in Equation (2.16). For the type of high energy impact expected in space, the thermal velocity of a diffusely re-emitted beam is likely to be much less than its incident velocity. Hence we can take the ratio E_w/E_i to be, effectively, 0. Therefore

$$\alpha = 1 - \frac{V_r^2}{V_i^2} \qquad \text{..... (2.27)}$$

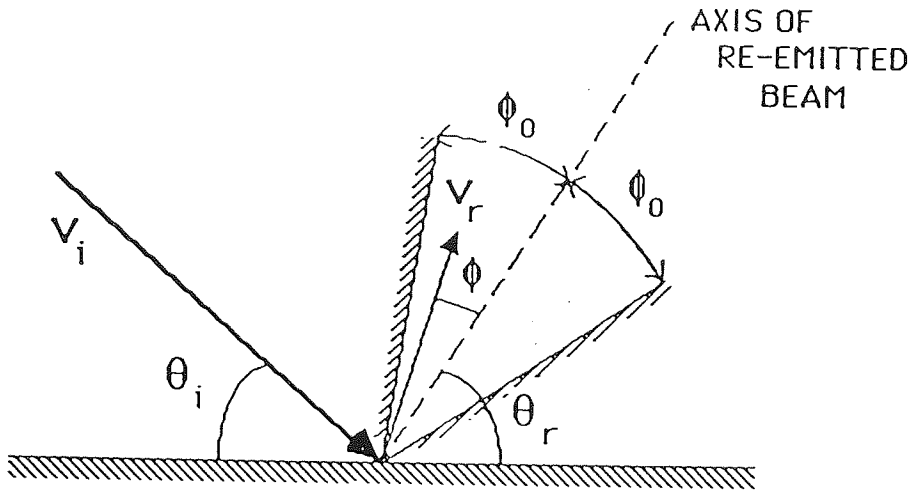

Figure 2.5 Schamberg's gas-surface interaction scheme

We can now see that the three parameters α, φ_o and υ completely describe the distribution of the reflected gas particles, noticing that for classically Specular reflection,

$$\begin{aligned} \alpha &= 0 \\ \upsilon &= 1 \\ \phi_o &= 0 \end{aligned} \qquad \text{..... (2.28)}$$

and for Diffuse reflection

$$\begin{aligned} \alpha &= 1 \\ \upsilon &= \infty \\ \phi_o &= \frac{\pi}{2.} \end{aligned} \qquad \text{..... (2.29)}$$

We may now proceed to find the normal and tangential momentum reflected per unit time, p_r and τ_r respectively. These are found to be

$$p_r = \rho V_i^2 \sin^2\theta_i \,.\, \Phi(\phi_o)\frac{V_r}{V_i}\cdot\frac{\sin\theta_r}{\sin\theta_i}, \qquad \text{..... (2.30)}$$

$$\tau_r = \rho V_i^2 \sin\theta_i \,.\, \cos\theta_i \,.\, \Phi(\phi_o)\frac{V_r}{V_i}\cdot\frac{\cos\theta_r}{\cos\theta_i},$$

where ρ is the density of the incident beam, and $\Phi(\varphi_o)$ is the beam width function given for a conical beam, by

$$\Phi(\phi_o) = \frac{1-\left(\frac{2\phi_o}{\pi}\right)^2}{1-4\left(\frac{2\phi_o}{\pi}\right)^2} \cdot \frac{\frac{1}{2}\sin(2\phi_o)-\left(\frac{2\phi_o}{\pi}\right)}{\sin\phi_o-\left(\frac{2\phi_o}{\pi}\right)} \qquad \text{..... (2.31)}$$

and

$$\Phi\left(\frac{\pi}{2}\right)=\frac{2}{3} \quad ; \quad \Phi(0)=1. \qquad \text{..... (2.32)}$$

Thus, the normal and tangential forces in our surface are given by

$$\begin{aligned} p &= \rho V_i^2 \sin^2\theta_i \left[1+\Phi(\phi_o)\frac{V_r}{V_i}\cdot\frac{\sin\theta_r}{\sin\theta_i}\right] \\ \tau &= \rho V_i^2 \sin\theta_i\cos\theta_i \left[1-\Phi(\phi_o)\frac{V_r}{V_i}\cdot\frac{\cos\theta_r}{\cos\theta_i}\right]. \end{aligned} \qquad \text{..... (2.33)}$$

If we assume that φ_o, α and υ are constants for all θ_i, we find the drag coefficient of a sphere is

$$C_{D_{SPHERE}} = 2\left[1 + 2\Phi(\phi_o)\frac{V_r}{V_i}\left\{I_1(\upsilon) - \frac{1}{\upsilon+3}\right\}\right] \quad \text{..... (2.34)}$$

where

$$I_1(\upsilon) = \int_0^1 x\sqrt{(1-x^{2\upsilon})(1-x^2)}\,dx.$$

Notice that this is a highly complex method of deriving satellite drag and lift coefficients for the general case. In order to utilise α we must introduce two new coefficients, φ_o and υ, for which we know nothing about any realistic numerical values or behaviour over varying angles of incidence. Schamberg recognised this, and realised that by setting φ_o and υ to their diffuse or specular values we could simplify the equations immensely, and proposed the definitions of quasi-specular and quasi-diffuse reflection.

In quasi-specular reflection, φ_o and υ take their specular values ($\varphi_o = 0$ and $\upsilon = 1$) and hence, using Equation (2.27), p and τ become

$$p = \rho V_i^2 \sin^2\theta_i \left[1 + (1-\alpha)^{\frac{1}{2}}\right]$$
$$\tau = \rho V_i^2 \sin\theta_i \cos\theta_i \left[1 - (1-\alpha)^{\frac{1}{2}}\right] \quad \text{..... (2.35)}$$

giving

$$C_{D_{SPHERE}} = 2.$$

Similarly, for quasi-diffuse reflection, $\varphi_o = \frac{\pi}{2}$ and $\upsilon \to \infty$, implying that

$$p = \rho V_i^2 \sin^2\theta_i \left[1 + \frac{2}{3}(1-\alpha)^{\frac{1}{2}}\right]$$
$$\tau = \rho V_i^2 \sin\theta_i \cos\theta_i \quad \text{..... (2.36)}$$

and

$$C_{D_{SPHERE}} = 2\left[1 + \frac{2}{3}(1-\alpha)^{\frac{1}{2}}\right].$$

The range of applicability of the "Quasi" models remains unknown. Since purely specular reflection has never been observed, the quasi-diffuse model has remained popular, as we can admit non-diffuse values of α in an easy analytical form, as in the case of Cook [14]. However, we have no reason to believe that quasi-diffuse reflection occurs in all situations, and by accepting that it does we eliminate a large number of possible alternatives.

Perhaps the greatest criticism levelled at Schamberg's model is in his interpretation of the model and the restrictions he placed on the numerical values obtained. Firstly, he calculates values for purely diffuse reflection, then for purely specular reflection and hence assumes that any non-specular and non-diffuse reflection will fall between these values. This is based on the false assumption that, if $\alpha = 0$ for specular reflection (although $\alpha = 0$ does not necessarily imply purely specular reflection) and $\alpha = 1$ for diffuse, then for intermediate values the beam will sweep between them, i.e. that $0 \leq \alpha \leq 1$ implies $\upsilon \geq 1$. This is disputed by Goodman [15] (and also by Bird [6]), who claims that, in the majority of cases, $\upsilon < 1$ would have been better. Indeed, Goodman [16] has pointed out that reflection below the specular angle is a characteristic of the interaction at such energies, backed by experimental results such as those of Calia and Oman [17], Romney and Anderson [18] and Miller and Subbarao [19], along with Nocilla's [13] interpretation of the experiments of Hurlbut [20]. Thus, to regard specular reflection as an "extreme" in the sense of a boundary of the reflected possibilities must surely be rejected in favour of some method that is not restricted by such intuitive prejudice. In its most general form, Schamberg's model has attracted some praise from Goodman [15] and, indeed, some of the notation was used by Kogan in 1969 [21].

The form of Schamberg's equations compares very well with the model using the momentum accommodation coefficients in hyperthermal flow. Indeed, equating Equation (2.33) with Equation (2.17) obtained earlier, we find, when we let $s \to \infty$, that

$$\sigma' = 1 - \Phi(\phi_o)\frac{V_r}{V_i}.\frac{\sin\theta_r}{\sin\theta_i}$$

$$\sigma = 1 - \Phi(\phi_o)\frac{V_r}{V_i}.\frac{\cos\theta_r}{\cos\theta_i} \qquad \text{..... (2.37)}$$

which means that, for quasi-specular reflection

$$\sigma' = \sigma \qquad \text{..... (2.38)}$$

and for quasi-diffuse reflection

$$\sigma' = 1 - \frac{2}{3}(1-\alpha)^{\frac{1}{2}}\operatorname{cosec}\theta_i$$

$$\sigma = 1. \qquad \text{..... (2.39)}$$

In anticipation of the remainder of this thesis, it will be interesting to compare Equations (2.39) with the results of the Chapters immediately following which describe the theoretical and experimental behaviour of the momentum accommodation coefficients.

2.4 Other Models of the Reflected Distribution

2.4.1 Introduction

Insofar as satellite orbital dynamics is concerned, Schamberg's model has been almost omnipresent throughout aerodynamic studies in the upper atmosphere. Indeed, Cook [22] in 1965 made a full enhancement to the model by estimating values of the thermal accommodation coefficient subject to the surface chemistry, to finally [14] introduce angular dependence using quasi-diffuse reflection.

Cook's deductions have been almost universally accepted, as has his value for the drag coefficient of a sphere as 2.2 which has been the basis for many studies of the thermosphere (e.g. the CIRA 1972 atmospheric model [3]). However, Cook's model demonstrates all of the flaws of Schamberg's model and must therefore be unacceptable as a justification for the drag coefficients utilised in such studies. Further models of gas-surface interaction have been developed over the years, of which those due to Karr [23] and Nocilla [13] are examples.

2.4.2 Karr's Model

This model differs from most others as Karr [23] does not attempt to describe the form of the scattered distribution, preferring to say that we can approximate its characteristics by a thin pencil beam of re-emitted particles, all with velocity V_r at an angle θ_r with the surface tangent.

In almost total analogy with Schamberg's quasi-specular model (that is, setting $\varphi_o = 0$) he assumes we can describe V_r using the thermal energy accommodation coefficient, but introduces a new parameter P_j to describe the angle θ_r, where:

$$\theta_r = \frac{\pi}{2} P_j + (1 - P_j)\theta_i. \qquad \text{..... (2.40)}$$

Restricting P_j to the range $0 \le P_j \le 2$, he does allow backscattering (i.e. $\theta_i > \frac{\pi}{2}$) up to a point, but thus attracts many criticisms for not allowing sub-specular ($\theta < \theta_i$) reflections.

Using the notation of former chapters, the normal and tangential forces on a unit element are given by

$$p = \rho V_i^2 \sin^2\theta_i \left[1 + (1-\alpha)^{\frac{1}{2}} \frac{\sin\left[\frac{\pi}{2}P_j + (1-P_j)\theta_i\right]}{\sin\theta_i} \right] \qquad \text{..... (2.41)}$$

$$\tau = \rho V_i^2 \sin\theta_i \cos\theta_i \left[1 - (1-\alpha)^{\frac{1}{2}} \frac{\cos\left[\frac{\pi}{2}P_j + (1-P_j)\theta_i\right]}{\cos\theta_i} \right].$$

Notice that this is still a difficult analytical model and we have lost any of the generality of Schamberg's model.

If we assume the constancy of α and P_j, the drag coefficient of a sphere is given by [57]

$$C_D = 2 + (1-\alpha)^{\frac{1}{2}} \frac{4\left(1-\cos P_j \frac{\pi}{2}\right)}{P_j(4-P_j)}. \qquad \text{..... (2.42)}$$

The simplicity of equations such as (2.42) does allow the possibility of using satellite data to find values for P_j and α. Indeed, Karr used the technique on the OVI-15 satellite obtaining 0.64 for α and 0.44 for P_j. However, assumptions made for the form of the scattered beam make the interpretation of such results difficult, particularly when so little experimental data is available for P_j.

2.4.3 Nocilla's Model

In 1963, Nocilla [13] proposed a model based on the assumption that the reflected gas stream has a Maxwellian distribution with macroscopic velocity V_r. Hence, the number distribution F is given by:

$$F = \frac{n_r}{\pi^{\frac{3}{2}}} \cdot \frac{1}{c_r^3} \exp\left\{-\frac{(c-V_r)^2}{c_r^2}\right\}. \qquad \text{..... (2.43)}$$

Here, c_r and n_r are the most probable thermal velocity and number of molecules per unit volume of the re-emitted gas. The two parameters used to describe this beam are the angle of reflection
with the surface normal, ξ_r, and s_r where

$$s_r = \frac{V_r}{c_r}. \qquad \text{..... (2.44)}$$

If we are allowed to vary ξ_r and s_r, Nocilla discovered excellent correspondence with the experimental results of Hurlbut [20].

The only criticism levelled at Nocilla (e.g. Cercignani [7] and Goodman [15]) is that the beam is not related to the incident beam in any way. However, Nocilla recognised this and suggested the introduction of two new parameters, ζ_t and ζ_n, where

$$V_r \sin\xi_r = (1-\zeta_t) V_i \sin\xi_i$$
$$V_r \cos\xi_r = (1-\zeta_n) V_i \cos\xi_i. \qquad \text{..... (2.45)}$$

(Note that ζ_t and ζ_n are closely analogous to tangential and normal accommodation coefficients.)

Hurlbut and Sherman [24] have attempted to use Nocilla's model to calculate theoretical drag coefficients using the three parameters α, s_r and θ_r but, despite including linear variations in α and s_r, restricted their views, basically, to lie within diffuse and specular reflection thus neglecting a large range of possibilities.

2.5 Conclusions

For each of the models of Schamberg [12] and Nocilla [13] we have witnessed attempts to initially model the scattered distribution of a gas stream and then introduce some parameterisation that links the reflected and incident gases. However, to make such parameterisations feasible, Schamberg, Hurlbut and Sherman [24] and, to some extent, Karr have to place restrictions on them according to their own intuitive ideas of the distribution behaviour. The restrictions are generally viewed with scepticism by the surface analysts and the rarefied gas dynamicists as described. Thus, when introducing a parameterisation we must place as few restrictions on it as possible such that we can truly explore the nature of the interaction of the thermosphere with a satellite surface and properly relate them to theoretical and experimental data.

As already mentioned, for aerodynamic purposes we are not strictly concerned with the scattered distribution of gas particles from a surface but only with the momentum exchange, which is completely described by the normal and tangential momentum accommodation coefficients, σ' and σ respectively for all cases of free-molecular flow. Initially, they were not adopted because of insufficient data, but, due to recent improvements in experimental techniques we can now make certain assumptions about their behaviour, and also relate our results directly to the laboratory. Further, σ' and σ have already been the subject of theoretical analysis, and surface models already exist for comparison with observed data.

Thus, the remainder of this thesis will be concerned with a study of the momentum accommodation coefficients and then to apply any conclusions to the orbit of the satellite ANS-1 (1974-70A).

CHAPTER 3
MOMENTUM ACCOMMODATION COEFFICIENTS

3.1 Introduction - Thermal and Structure Scattering

The gas-surface interface has remained the subject of much study, not only for aerodynamic purposes but also to study the structure of crystal lattices, the electric potential between gas atom and surface molecule and boundary problems affecting solutions of the Boltzmann equation. Most of the relevant references are covered by Tully [25]. However, most of the work relevant to the satellite aerodynamicist was covered in the 1960's and is best summarised in a review paper by Goodman [16].

An important consideration in the field of gas-surface interactions is the relative energy of a gas particle to a surface particle, manifesting itself in the parameter t, where, if E_o is the kinetic energy of the gas particle striking the surface and T_s the temperature of the surface, then [16]

$$t = \frac{E_o}{kT_s} \qquad \text{..... (3.1)}$$

where k is Boltzmann's constant.

If $t << 1$ the gas particle strikes the surface in such a slow fashion that it can easily detect, and is changed by, the thermal vibrations of the surface particles. Also, if the gas-surface particle electromagnetic potential is large enough, the gas particle may not actually penetrate very far towards the surface molecule and it may thus behave as if it is striking a "smooth" surface. Such a process of gas-surface interaction is called Thermal Scattering [16].

As the energy of the incident gas particles increases, the degree of penetration into the surface increases until, with $t >> 1$, the gas particles are effectively striking the individual molecules of the surface which, because of the high incident velocity of the gas, can be taken to be relatively stationary at collision. This type of scattering is called Structure Scattering [16].

In structure scattering we can assume, effectively, that $T_s = 0$ (i.e. that, on collision, the motion of the surface particle is negligible compared to the gas particle) and that the gas-solid interaction is governed by the laws of "billiard ball mechanics" - perfectly elastic collisions. Here we will assume that the gas particle is much lighter than the surface particle. If this were not so, the gas particle may penetrate into the surface requiring extensive further analysis to describe the possibilities of absorption or outgassing.

An interesting point to notice is that, generally, in thermal scattering most particles are scattered above the specular angle (SUBSPECULAR) whereas as we approach structure scattering most particles are scattered below the specular angle (SUPRASPECULAR). This observation was first noted by Oman [26], with the subsequent backing of experiment (e.g. Calia and Oman [17], Romney and Anderson [18] and Miller and Subbarao [19]).

For the majority of satellites $t >> 1$. Indeed, for a hydrogen atom striking a surface where $T_s = 1000°K$ at a velocity of 7 km/s we find that $t \sim 3$, which implies that the majority of neutral particle interactions will be characterised by structure scattering.

3.2 Elastic Collisions

Let us consider the two-dimensional elastic collision between a dynamic gas particle of mass m, and a stationary surface particle of mass M. Assume the gas particle has initial velocity V_i at an incident angle ξ_i to the surface normal **n**. After the collision the gas particle has velocity V_r and angle of reflection ξ_r with the surface normal, whereas the surface particle now has velocity u (Figure 3.1).

Thus, for this collision the thermal energy, normal and tangential momentum accommodation coefficients, α, σ', and σ respectively, by definition, are given by:

$$\alpha = 1 - \frac{V_r^2}{V_i^2}$$

$$\sigma' = 1 - \frac{V_r \cos\xi_r}{V_i \cos\xi_i} \qquad \text{..... (3.2)}$$

$$\sigma = 1 - \frac{V_r \sin\xi_r}{V_i \sin\xi_i}.$$

We will assume that the masses m and M are spherical and, for the moment, we will take $m < M$, which allows the gas particle to "bounce" away from the surface particle after collision. Also we consider for simplicity that there is only one collision between particles and that there are no further collisions between the reflected gas particle and the surface.

Now, for the general case, the gas particle can strike any parts of the hemisphere turned towards it. We will define φ to be the angle between the surface normal and the point of collision on the surface particle, as in Figure 3.2.

An elastic collision between the two particles, where energy and linear momentum are conserved, has the following consequences for our accommodation coefficients:

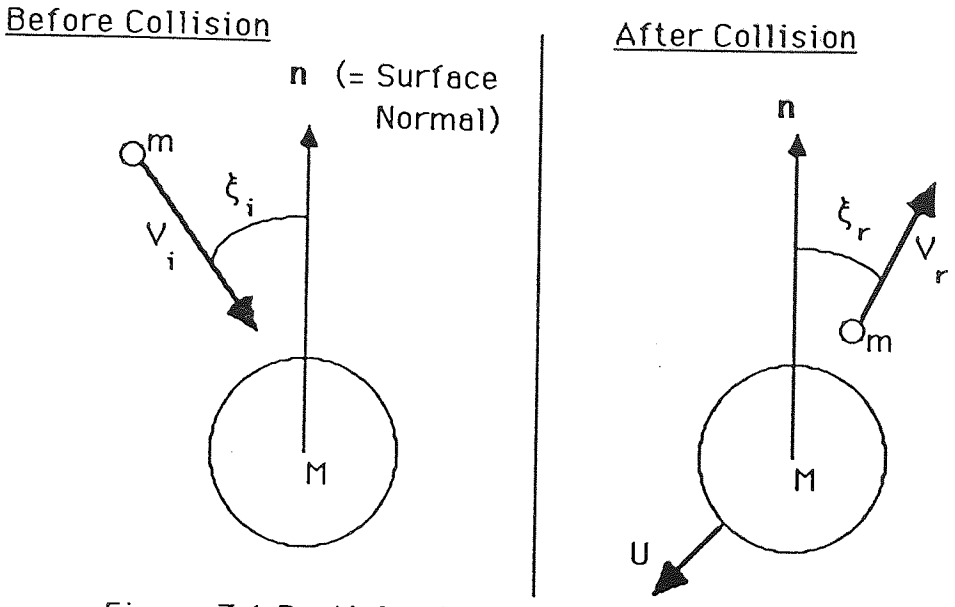

Figure 3.1 Particle states before and after collision

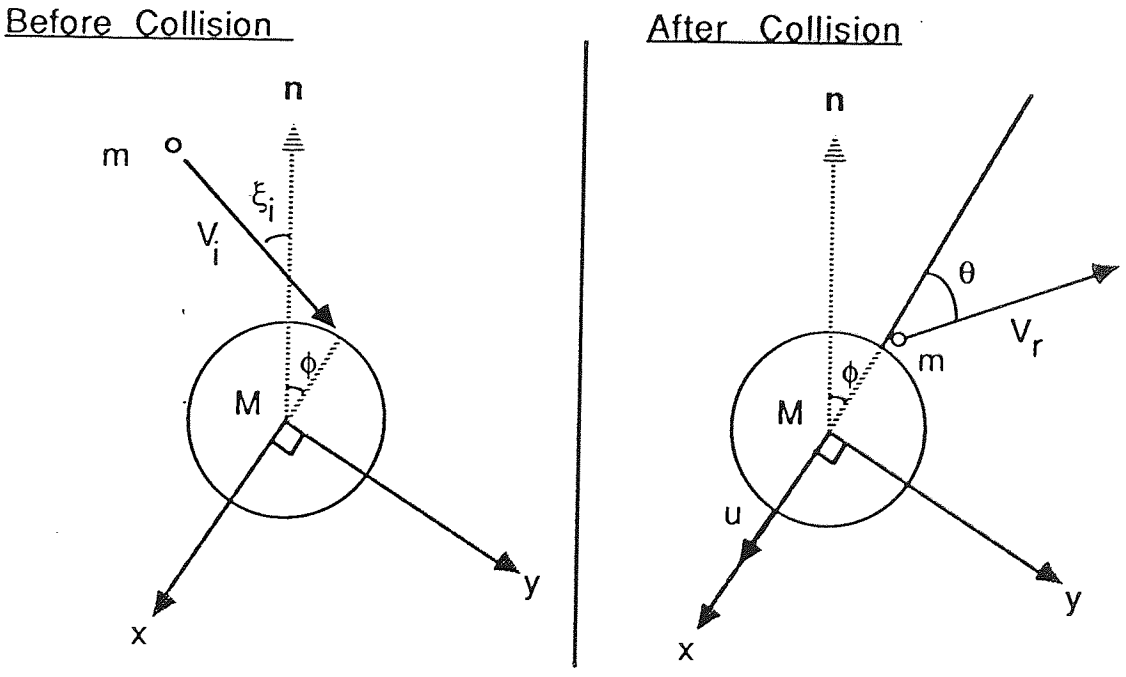

Figure 3.2 Scheme for the collision between two particles

If we take the scheme of Figure 3.2 we find that, for a conservation of kinetic energy,

$$mV_i^2 = mV_r^2 + Mu^2$$

which implies that

$$\mu V_i^2 \alpha = u^2 \qquad \text{..... (3.3)}$$

where $\mu = \frac{m}{M}$.

Conservation of linear momentum in the y-direction implies that

$$V_i \sin(\xi_i + \phi) = V_r \sin\theta$$

which may be rewritten as:

$$(1-\alpha)\cos^2\theta = (1-\alpha) - \sin^2(\xi_i + \phi). \qquad \text{..... (3.4)}$$

Conservation of momentum in the x-direction implies that

$$mV_i \cos(\xi_i + \phi) = Mu - mV_r \cos\theta$$

which may be re-written as

$$u = \mu\{V_i \cos(\xi_i + \phi) + V_r \cos\theta\}. \qquad \text{..... (3.5)}$$

Hence

$$u^2 = \mu^2\{V_i^2 \cos^2(\xi_i + \phi) + V_r^2 \cos^2\theta + 2V_i V_r \cos(\xi_i + \phi)\cos\theta\}.$$

Using Equation (3.3) we find that

$$\alpha = \mu\left\{\cos^2(\xi_i + \phi) + (1-\alpha)\cos^2\theta + 2\frac{V_r}{V_i}\cos\theta\cos(\xi_i + \phi)\right\}$$

and after a substitution of Equation (3.4) we see that

$$(1+\mu)\alpha = 2\mu\cos(\xi_i + \phi)\left\{\cos(\xi_i + \phi) + \frac{V_r}{V_i}\cos\theta\right\}$$

which equals

$$\frac{V_r}{V_i}\cos\theta = \frac{(1+\mu)\alpha}{2\mu\cos(\xi_i + \phi)} - \cos(\xi_i + \phi).$$

Squaring both sides we see that

$$(1-\alpha)\cos^2\theta = \frac{(1+\mu)^2\alpha^2}{4\mu^2\cos^2(\xi_i + \phi)} - \frac{(1+\mu)\alpha}{\mu} + \cos^2(\xi_i + \phi)$$

and by a further substitution of Equation (3.4) we see that

$$\frac{\mu}{1+\mu} = 1 - \frac{1+\mu}{4\mu\cos^2(\xi_i + \phi)}\alpha,$$

and hence

$$\alpha = \frac{4\mu}{(1+\mu)^2}\cos^2(\xi_i + \phi). \qquad \text{..... (3.6)}$$

This may now be used to derive comparable results for σ' and σ.

Our definition of σ may be adapted to Figure 3.2 to give

$$\sigma = 1 - \frac{V_r \sin(\phi + \theta)}{V_i \sin\xi_r}.$$

Now, a re-writing of Equation (3.3) gives

$$1 - \frac{V_r^2}{V_i^2} = \frac{1}{\mu}\frac{u^2}{V_i^2}$$

whereas (3.6) gives us

$$1 - \frac{V_r^2}{V_i^2} = \frac{4\mu}{(1+\mu)^2}\cos^2(\xi_i + \phi).$$

Equating these two gives us

$$u = V_i \hat{\sigma}\cos(\xi_i + \phi)$$

where

$$\hat{\sigma} = \frac{2\mu}{1+\mu}.$$

If this is now substituted into (3.5) we see that

$$(\hat{\sigma} - \mu)V_i \cos(\xi_i + \phi) = \mu V_r \cos\theta$$

and multiplying both sides by $\sin\phi$ we find that

$$V_r \cos\theta \sin\phi = (1 - \hat{\sigma})V_i \cos(\xi_i + \phi)\sin\phi.$$

A re-arrangement of (3.4) gives us

$$V_r \sin\theta \,.\, \cos\phi = V_i \sin(\xi_i + \phi)\cos\phi.$$

The sum of these last two equations gives us, after some manipulation,

$$\frac{V_r \sin(\phi + \theta)}{V_i \sin\xi_i} = \frac{1}{2}\left\{\hat{\sigma} + (2 - \hat{\sigma})\frac{\sin(2\phi + \xi_i)}{\sin\xi_i}\right\}$$

from which we find that

$$\sigma = \frac{1}{2}(2 - \hat{\sigma})\left[1 - \frac{\sin(2\phi + \xi_i)}{\sin\xi_i}\right]. \qquad \text{..... (3.7)}$$

Now, $\sigma' = 1 - \dfrac{V_r \cos(\phi + \theta)}{V_i \cos\xi_i}$

and, in analogy to the method used to derive σ we find that

$$\sigma' = 2 - \frac{1}{2}(2 - \hat{\sigma})\left[1 + \frac{\cos(2\phi + \xi_i)}{\cos\xi_i}\right]. \qquad \text{..... (3.8)}$$

Thus, if we believe that the gas particle can strike all of the surface turned towards it, then

$$-\frac{\pi}{2} - \xi_i \le \phi \le \frac{\pi}{2} - \xi_i. \qquad \text{..... (3.9)}$$

We can now find average values of α, σ' and σ (given by $\bar{\alpha}, \bar{\sigma}'$ and $\bar{\sigma}$ respectively) over all values of φ, namely,

$$\bar{\alpha} = \frac{2\mu}{(1+\mu)^2}$$

$$\bar{\sigma}' = \frac{1}{2}(2 + \hat{\sigma}) \qquad \text{..... (3.10)}$$

$$\bar{\sigma} = \frac{1}{2}(2 - \hat{\sigma}).$$

The value of $\bar{\alpha}$ in (3.10) was first suggested by Baule in 1914 [27], but because of shielding by other surface atoms, restricting the possible values of φ, a more useful value is

$$\bar{\alpha} = \frac{k\mu}{(1+\mu)^2} \qquad \text{..... (3.11)}$$

where $2 \le k \le 4$. Equation (3.11) was used by Cook [22] who, by using Schamberg's model for the reflected distribution, evaluated the drag coefficient for a variety of regular objects, concluding that despite some uncertainty, the drag coefficient for a sphere will lie around 2.4 for a satellite.

We note here that Oman found a good empirical value for α would be [28]

$$\alpha = \frac{4\mu}{(1+\mu)^2}\cos\xi_i. \qquad \text{..... (3.12)}$$

Using this expression and the quasi-diffuse and quasi-specular models of Schamberg, Cook [14] concluded that the drag coefficient of a sphere would be around 2.2, with an error of less than 33%.

This empirical result aside, the value of averaging values of φ must surely be questionable, especially when we have taken no account of the direction of the

re-emitted beam. If we examine $\overline{\sigma}'$ we find that it is always greater than 1, which implies that, on average, most particles are reflected into the surface, and if we find the drag coefficient of a sphere using $\overline{\sigma}'$ and $\overline{\sigma}$ in Equation (2.41), we obtain

$$C_{D_{\text{SPHERE}}} = 2 - \hat{\sigma}$$

i.e. a value that is always less than 2 would certainly contradict Cook's results.

Despite the good results for α, backed up by experimental results such as those by Oman et al [29], the implications of this type of averaging on the force on a surface, and hence σ' and σ, are surely preposterous when we do not consider the full effects of multiple collisions and shadowing by adjacent particles.

3.3 The Hard-Spheres Model

Due to the complicating effects of multiple collisions and shielding, an analytical model of elastic gas-surface interactions would be hard to achieve. Thus, numerical simulation of these effects could substantially improve our knowledge of elastic gas-surface collisions, providing useful empirical behavioural relationships. In 1967 Goodman [30, 31] developed a 3-dimensional computer simulation of the problem, assuming that the surface could be represented as a regular 2-dimensional array of similar spheres that are initially stationary. This is the Hard-Spheres model.

Denoting the type of array by S, he considered two forms of the arrangement of molecules on the surface: S = square and S = triangular, where L is the distance between adjacent surface molecules and φ is the polar angle describing a direction relative to the surface particles. (See Figure 3.3.)

Given that the radii of the gas atom and the surface atom are r_g and r_s respectively, he assumed that the gaps between the surface atoms are small enough to prevent a gas atom from penetrating through, i.e. that for S = square,

$$r_s + r_g > \frac{L}{\sqrt{2}}$$

and for S = triangular

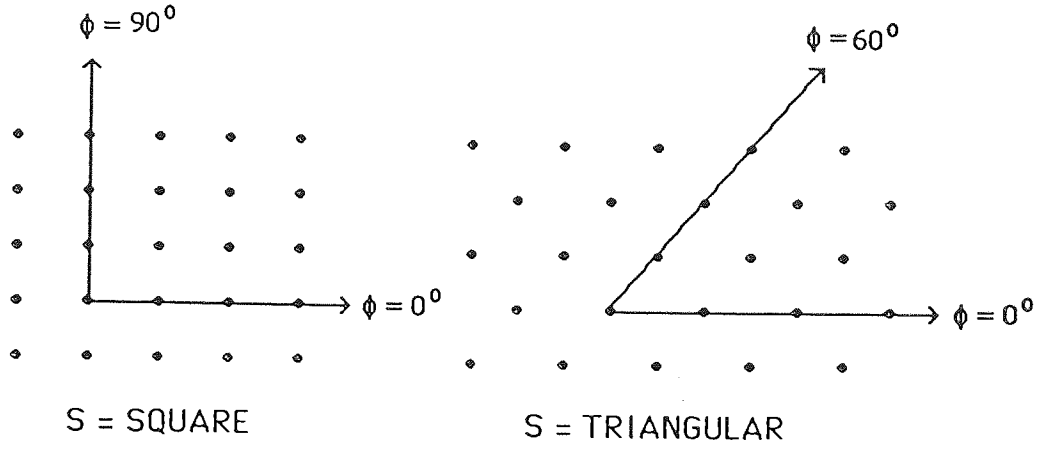

Figure 3.3 Square and Triangular surface arrays

$$r_s + r_g > \frac{L}{\sqrt{3}}.$$

He interpreted his results, calculated over many possible trajectories, in terms of five basic parameters:

(i) The array size parameter R, where

$$R = \frac{r_s + r_g}{L}$$

restricting it to the range $0.9 \leq R \leq 1.3$, which covers many values of interest to the gas-surface analyst (see Table 3.1).

SYSTEM	μ	R
He -W	0.0218	1.0
Ar - W	0.217	1.1
Xe - W	0.714	1.2
He - Ni	0.0682	1.2
Ar - Ni	0.680	1.4

Table 3.1 - μ and R Values for Different Gas-Surface Combinations (Goodman [31])

(ii) The mass ratio, μ, where $0 \leq \mu \leq 1$.

(iii) S, the type of array.

(iv) The spherical angle of incidence, θ_o ($= \pi - \xi_i$).

(v) The direction along the array, given by φ_o.

A selection of the results for the accommodation coefficients are given by Figures 3.4 to 3.7.

Goodman concluded that the results for the accommodation coefficients were generally independent of φ_o and that an approximate correlation of the results could be obtained by the equations:

$$\alpha = \frac{3.6\mu}{(1+\mu)^2}\cos\xi_i$$

$$\sigma' = \sigma'_0 - \sigma'_1 \sec\xi_i \qquad \text{..... (3.13)}$$

$$\sigma = C \,.\, \cos\xi_i$$

where $\sigma'_0 > \sigma'_1 > 0$ and $C > 0$, each parameter being a function of μ and R. For the scattered distribution, excellent agreement with experiment is achieved (see Figure 14 of reference [16]).

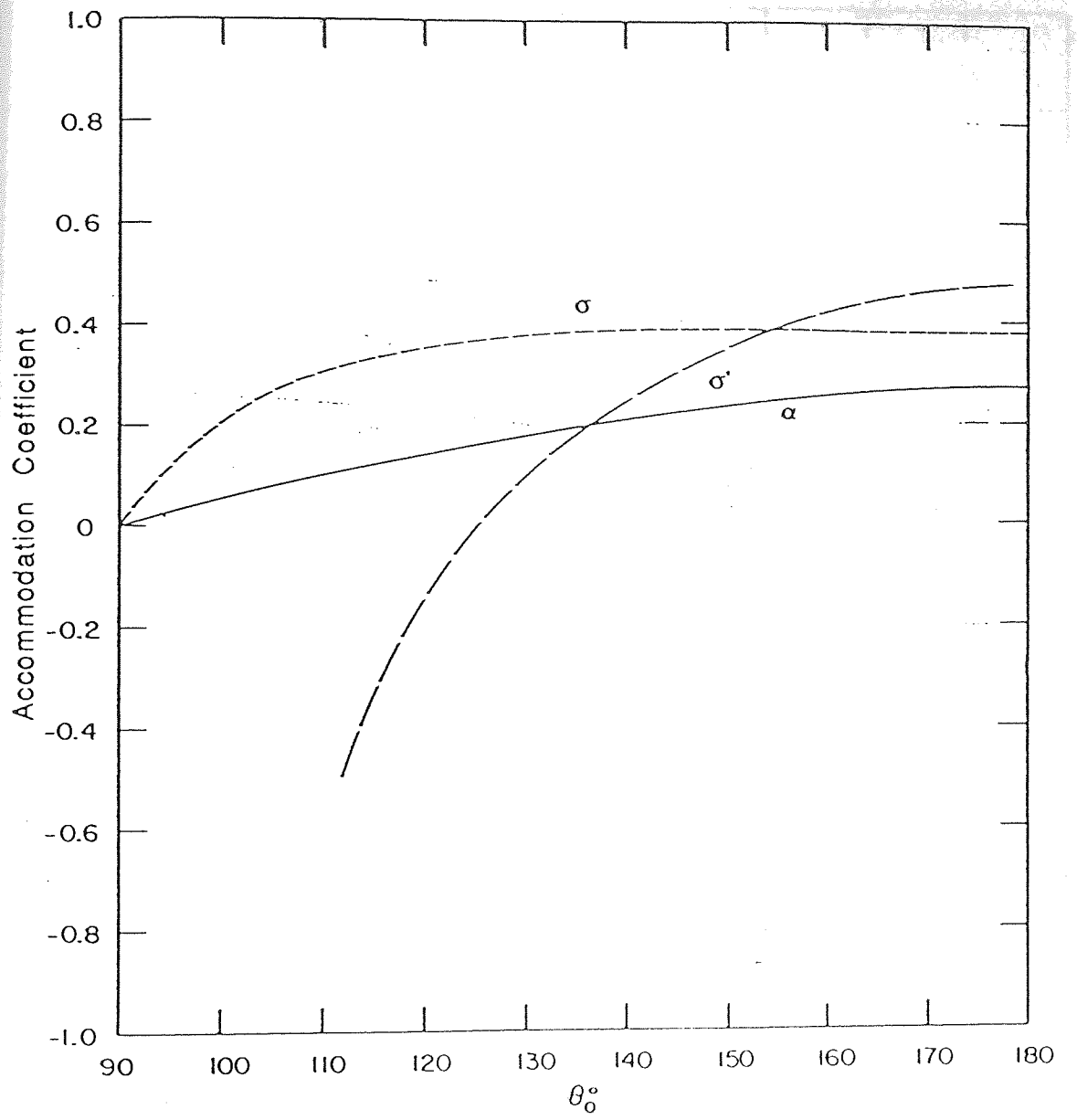

Figure 3.4 Goodman's simulation results for μ=0.1, R=0.9, S=triangular and ϕ_0=0

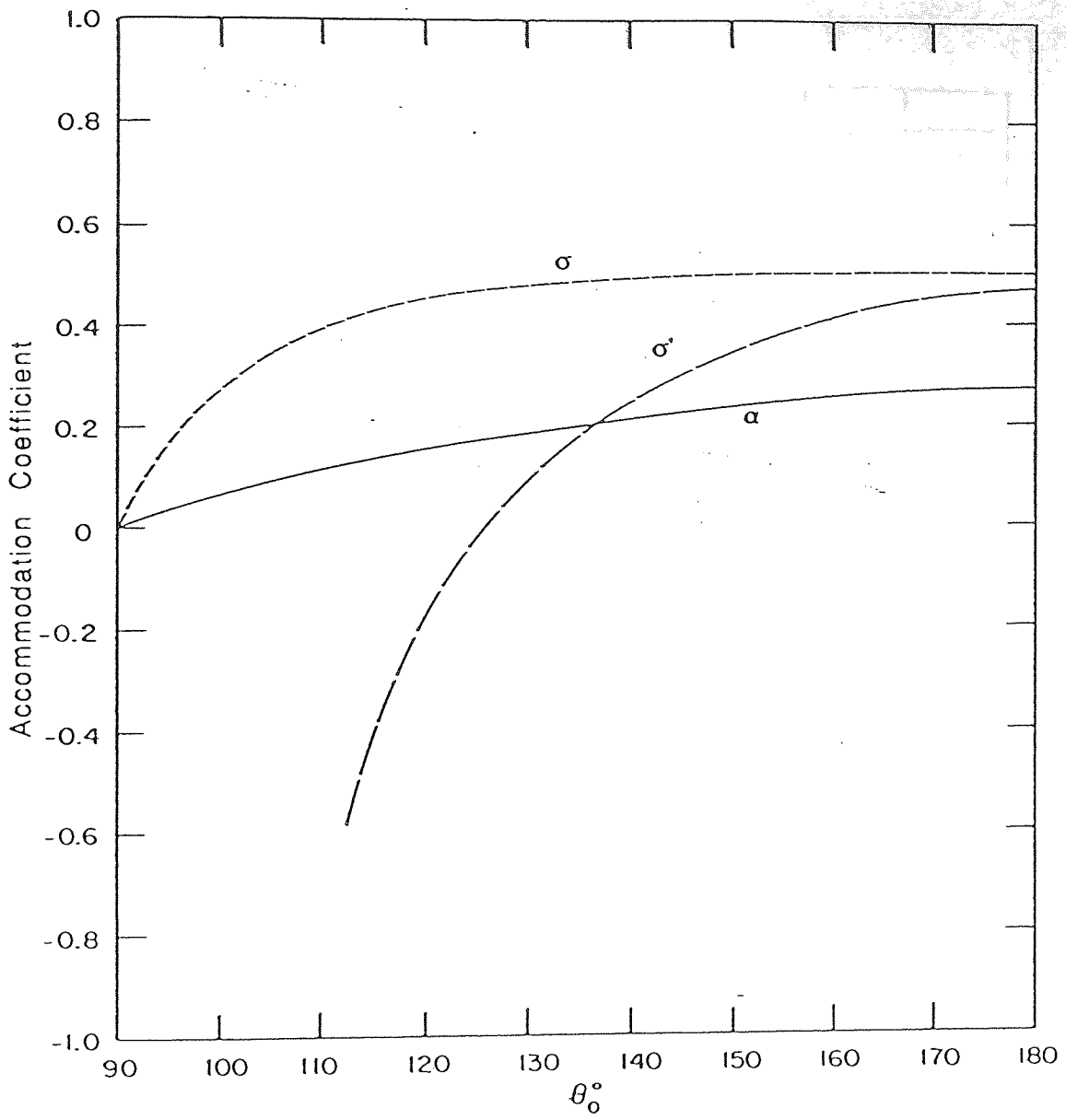

Figure 3.5 Goodman's simulation results for μ=0.1, R=0.9, S=square and ϕ_0=45°

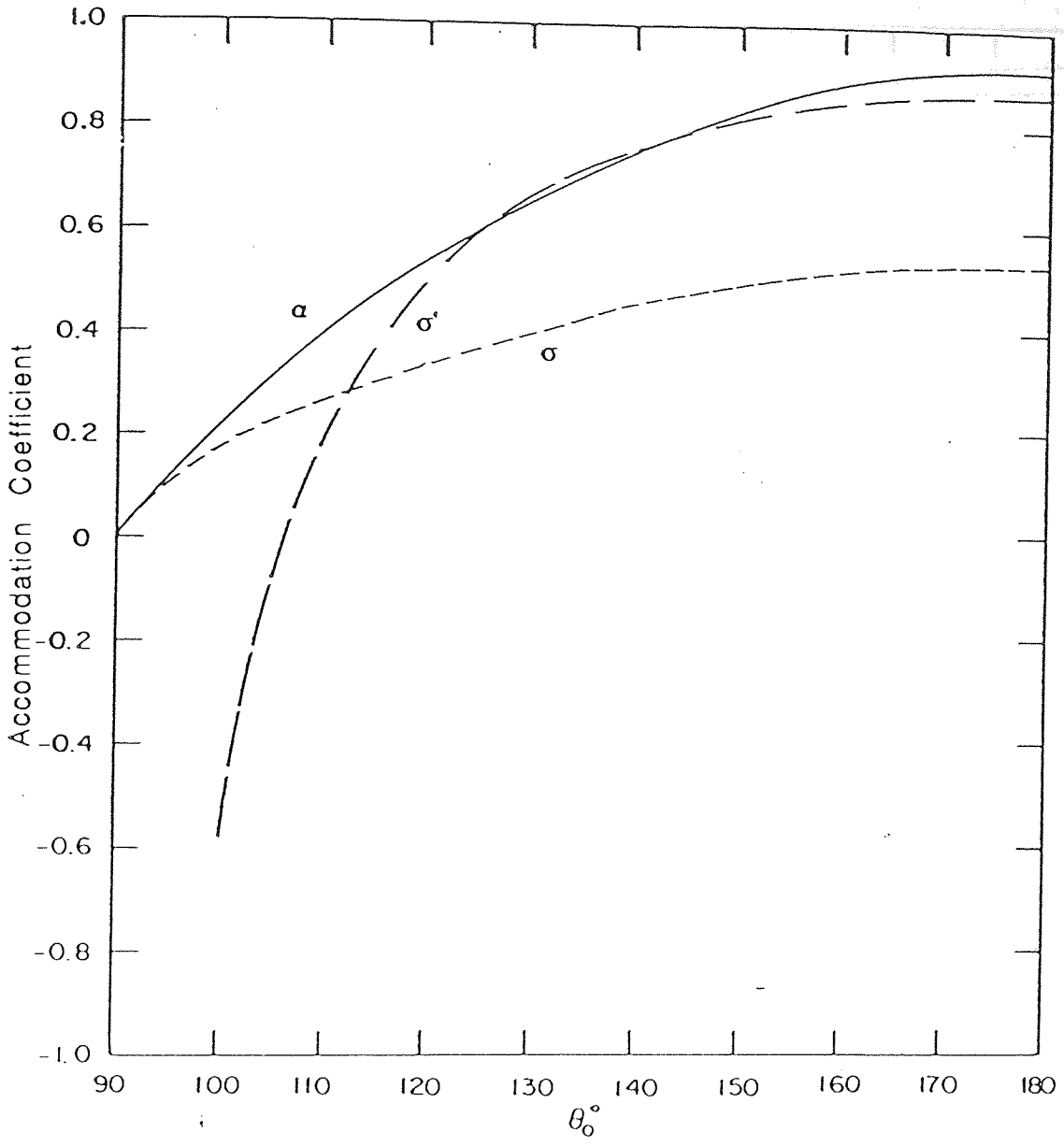

Figure 3.6 Goodman's simulation results for μ=0.9, R=0.9, S=square and ϕ_0=45°

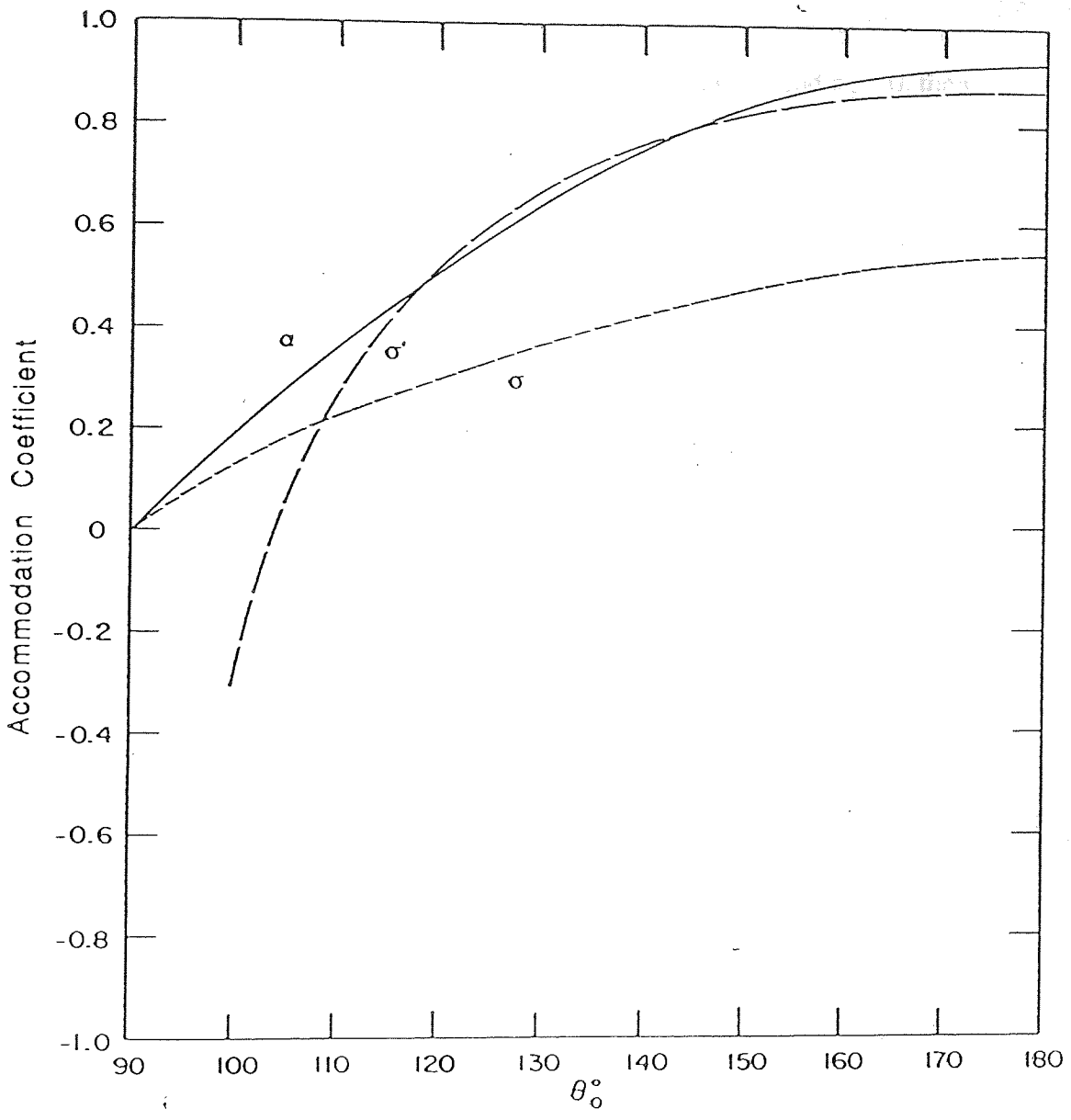

Figure 3.7 Goodman's simulation results for μ=0.9, R=1.3, S=square and ϕ_0=0

If we consider $C_{D_{SPHERE}}$ using the accommodation coefficients in (3.13) we find

$$C_{D_{SPHERE}} = 2 - \sigma'_0 + \frac{4}{3}\sigma'_1 - \frac{8}{15}C. \qquad \text{..... (3.14)}$$

Estimating his results for $\mu = 0.9$, R = 0.9, S = square and $\varphi_o = 0$, then

$C_{D_{SPHERE}} \sim 1.1$

whereas for $\mu = 0.1$, the same system gives

$C_{D_{SPHERE}} \sim 1.6$.

Goodman's hard-spheres model was developed in 1967 when there was little experimental evidence for the behaviour of the momentum accommodation coefficients with angle of incidence. However, due to improvements in Laboratory techniques, some evidence has surfaced. Hence, before we can come to any conclusions, a consideration of such results is needed.

3.4 The Dependence of the Momentum Accommodation Coefficients On Angle of Incidence

Experimental values for σ' and σ have remained elusive for many years. When Schaaf and Chambre considered their use in 1958 [9] they considered values of σ that were obtained by Millikan in 1923 [32] only, as there were no comparable values for σ' and no indications of behaviour with angle of incidence.

The behaviour of the drag and lift forces with angle of incidence, and hence σ' and σ, remains a crucial ingredient to properly formulate the aerodynamic problem for satellites, particularly when many satellites are oriented in some direction, meaning that the incident angle with the atmosphere sweeps only slowly over the body of the craft, thus producing effects pronounced over only one portion of the orbit.

There has been a significant improvement in the measurement of σ and σ' throughout the last twenty years, ranging from the measurement of σ by rotating disks in a stationary gas [33] to the firing of molecular beams at targets placed, at various incident angles, in their path [34, 35, 36, 37, 38]. Indeed, we have now seen actual satellite samples in such devices such as the firing of N_2 molecules on surfaces of the type used on Echo I and Echo II [39]. Also, Boettcher et al [4] have placed a model of the TD-1A satellite in a high speed vacuum wind tunnel. However, to fully utilise such work, we need to study the behaviour of the two coefficients σ' and σ and see what generalisations can be made.

The tangential momentum accommodation coefficient, σ, was perhaps the least elusive of the two, as it best describes the "friction" between a gas and a surface. Thus, many values for a general angle of incidence are available, such as the studies by Thomas and Lord [33] and Lord [40]. Most of the recent studies of the variation of σ with angle of incidence have been done in conjunction with σ', and have shown a degree of inconsistency in the trends affecting σ. Indeed, although Doughty and Schaetzle [37] show that there is a marked linear decrease in σ as the angle of incidence with the surface normal ξ_i increases, other references seem to suggest that, although there may be some variation of σ with ξ_i this is only very slight. This is certainly echoed in the work of Steinheil et al [34], where σ may increase or decrease depending on the purification of the surface. Also, Liu at al [38], firing Helium atoms at an aluminium plate, and Seidl and Steinheil [35], firing Helium at sapphire, have shown that, for these systems at least, a constant value of σ can be adopted with only a small margin of error.

The normal momentum accommodation coefficients, σ', have displayed characteristics that are far more consistent from experiment to experiment. All results (e.g. [35, 36, 37, 38, 41]) show that σ' decreases as the angle of incidence increases, starting off very slowly but increasing as a grazing angle is approached. Such observations prompted Knuth [42], when assessing many results together, to suggest the following empirical behaviour for σ'. Under the assumption that all of the surfaces are "cold" ($p_w = 0$), Knuth suggested that

$$\begin{aligned} \sigma' &= 1 && \text{for } 0 \le \xi_i < 30^\circ \\ &= 1 - \frac{\xi_i}{90^\circ} && \text{for } 30^\circ \le \xi_i < 90^\circ. \end{aligned} \qquad \text{..... (3.15)}$$

If we adopt this model, we find that, assuming σ is constant, the drag coefficient for a sphere is given by

$$C_{D_{\text{SPHERE}}} = 1.99 + \sigma. \qquad \text{..... (3.16)}$$

However, if we assume that $\sigma = \sigma'$, we find

$$C_{D_{\text{SPHERE}}} \approx 1.67. \qquad \text{..... (3.17)}$$

As an attempt to describe general trends, Knuth's model is adequate, but the suggestion that there is such a marked change in behaviour at $\xi_i = 30^\circ$ has certainly never been detected. Perhaps a more interesting observation is that the behaviour of σ' seems highly reminiscent of the behaviour of σ' in Goodman's hard-spheres model [31], where he suggested that σ' could be suitably described by the relationship

$$\sigma' = \sigma'_0 - \sigma'_1 \sec\xi_i. \qquad \text{..... (3.18)}$$

Indeed, by choosing suitable values of σ'_0 and σ'_1 we find excellent correspondence. For instance, the results of Reference [38], shown in Figure 3.8, suggest that $\sigma'_0 \sim 0.84$, $\sigma'_1 \sim 0.12$ and $\sigma \sim 1$, which implies

$$C_{D_{\text{SPHERE}}} \approx 2.32 \qquad \text{..... (3.19)}$$

and the Helium on sapphire results of Reference [35], shown in Figure 3.9, imply that $\sigma'_0 = 1.09$, $\sigma'_1 = 0.35$ and $\sigma = 0.72$, giving

$$C_{D_{\text{SPHERE}}} \approx 2.1. \qquad \text{..... (3.20)}$$

When extrapolating their experimental results, Knechtel and Pitts [36] observed values of $C_{D_{\text{SPHERE}}}$ of as low as 1.71, thus suggesting that results obtained in a consideration of momentum accommodation may appear initially contradictory to the values of $C_{D_{\text{SPHERE}}} \sim 2.2$ obtained by Cook [14, 22]. However, the majority of experimental values are found for highly specialised surfaces and often using a gas of a single constituent. Thus, any values of σ'_0, σ'_1 and σ found in the laboratory must be treated with caution as there remains much uncertainty about the particular surface chemistry of satellite bodies in the Upper Atmosphere. Perhaps the most interesting result of the experimental work, is that, at least for σ', gas-surface interaction displays many of the characteristics of Goodman's hard-sphere's model.

Where Goodman has failed is in his values for σ, where, although generally flat and invariant curves are demonstrated in agreement with experiment, they are consistently low in value, hardly ever exceeding 0.5. Laboratory results, however, show very high values of σ, often exceeding 1 (a characteristic of backscatter) but seldom falling below 0.5. This seems to suggest that a model of the surface based on a regular array of spheres will never produce the characteristically high levels of "friction" found for real surfaces. This may be explained by the observation that the majority of engineering surfaces will not exhibit a crystal-like regularity of atoms due to a composite nature and the method of manufacture. Thus, rather than discard Goodman's analysis due to its idealism, it would be useful to see if we can, using his principles, construct an artifically roughened surface which will model more effectively the behaviour of a real surface.

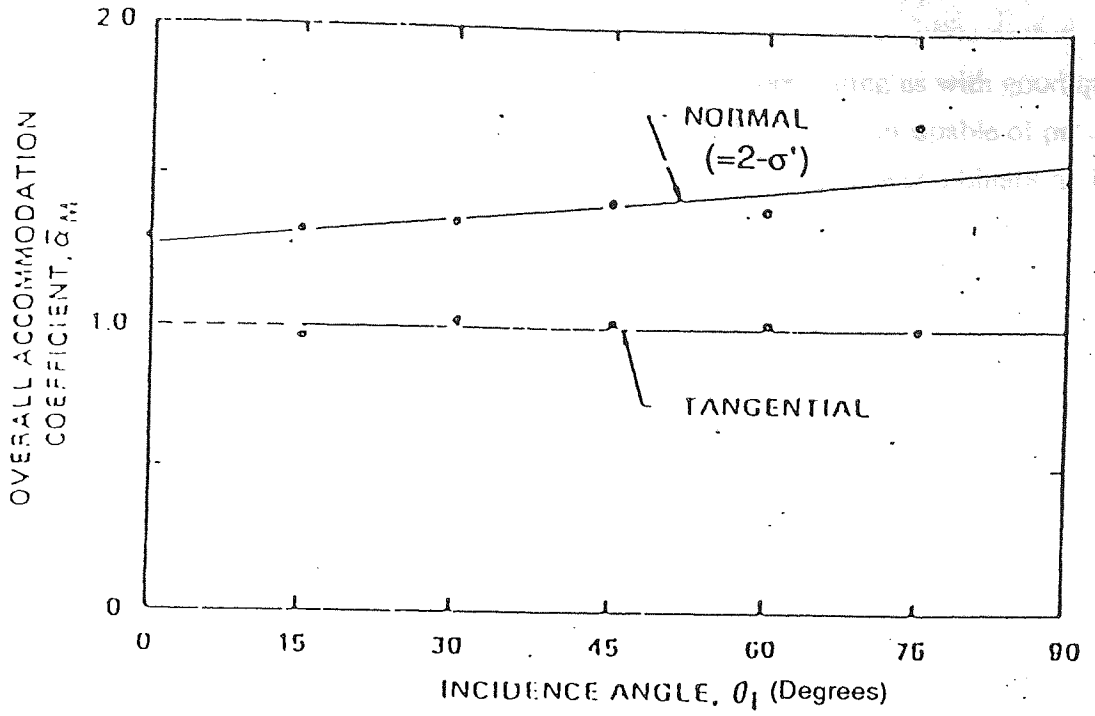

Figure 3.8 Experimental results from Liu [38]

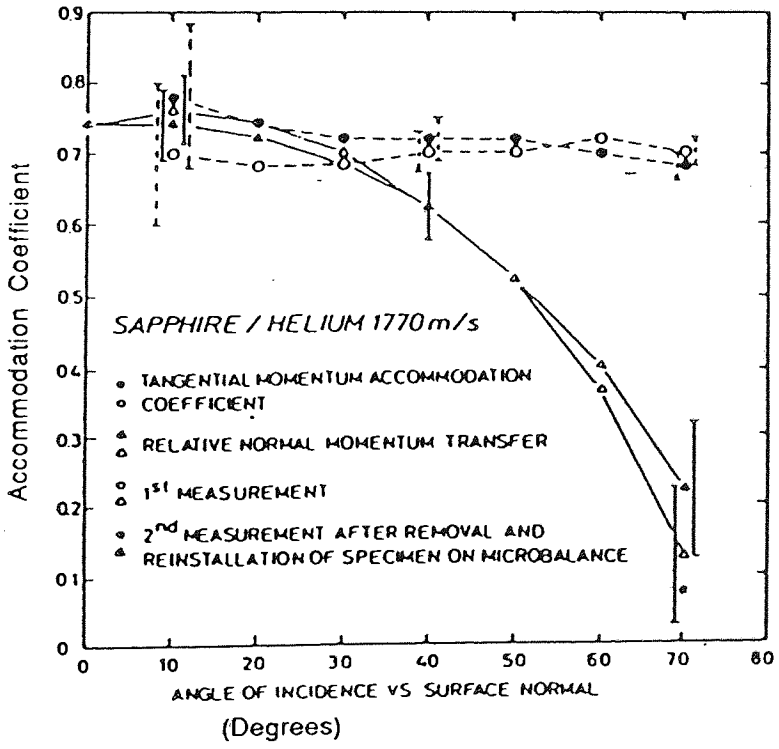

Figure 3.9 Experimental results from Seidl [35]

CHAPTER 4
ELASTIC COLLISIONS AND SURFACE STRUCTURE

4.1 Introduction

Goodman's hard-spheres model, although presenting us with good qualitative agreement with experimental observations, fails in being incapable of producing the correct quantitative results required for a given gas/surface combination. However, this failure does not imply that the model is inadequate and should be discarded - quite the reverse.

As discussed in the previous chapter, the general trends of the model seem to positively mimic the trends of experiment; that is we see a marked decrease in the value of σ' with increasing angle of incidence, whereas variations in σ are generally not so pronounced. This would seem to suggest that elastic scattering has succeeded in one respect and perhaps further parameterisations are needed to compensate for unknown processes that may occur at a real surface.

The hard-spheres model is, indeed, idealistic. We have assumed that each of the surface particles are spherical and arranged in a regular, flat, array which only occurs in crystalline materials at a perfectly formed facet. Furthermore, we have assumed that all gas particles are of one size and all surface particles are of another size. In the real world this is hardly ever the case, particularly in space where the surface is more likely to be some alloy or composite material, and the atmosphere is a mixture of various atomic and bi-atomic particles. This is further complicated by the observation that the surface may react chemically with the atmosphere. Serious degradation at the surface of many different materials in space has been observed, such as in the shuttle-borne STS-8 experiment [61].

However, the modelling of structure scattering by elastic collisions is a widely accepted technique, and has appeared particularly useful when the gas particle is very light ($\mu \ll 1$). Indeed, more recently Steinbruchel [43] used a 1-D array of capped cubes to model a surface with elastic scattering.

The results of Goodman consistently show an underestimated value of σ, suggesting that a 2-D array of spheres does not display the correct amount of "friction" anticipated at a surface. Thus, we may conclude that the correct "friction" may be achieved by adding more structure to the surface and roughening its features. It must be stressed here that we are no longer trying to parameterise the momentum exchange in terms of elastic collisions and surface structure.

We will confine the following analysis to a study of a 1-D surface with periodic "peaks" and "valleys", beginning with a description of a generalised surface and leading towards a computer simulation of the problem.

4.2 Generalised Surface Structure

Like Goodman, we will consider the collision of dynamic, spherical gas particles of mass m with a stationary surface. However, to simplify calculations a more convenient "surface" to consider is the surface generated by the centres of mass of the gas particles at closest approach to the surface. This enables us to consider only a point mass m striking the "collision surface", a familiar concept to surface science, which vastly simplifies calculation. (See Figure 4.1.)

Let us consider that a portion of the collision surface can be represented by successive arrangements of a curve Γ, i.e. that the surface is periodic in Γ. The normal to the whole macroscopic surface is given by N and the tangent by T. (Figure 4.2.)

A point mass, m, strikes a point P on the surface at an angle of incidence of ξ_i and is reflected at an angle ξ_r to the surface normal at a velocity V_r. The normal to the curve Γ at P is given by $\mathbf{n}_P$, which subtends the angle of α_P with the surface.

We are considering here that the curve Γ lies in the plane of the paper and hence that all vectors shown in Figure 4.2 are coplanar. This is feasible from the observations that, firstly, a single collision between two particles lies in a single plane and, secondly, that no experiment of surface scattering has ever shown any dependence on the "yaw" angle, i.e. a rotation of the surface about the macroscopic normal N. In developing more sophisticated models some 2-D structure may need to be introduced such as lattice structure, but here we are principally concerned with a simple assessment of the effect of surface structure.

The mechanics of the collision at P is described by the point mass m striking a stationary "hard-cube" of mass M, which has a normal of $\mathbf{N}_P$ (see Figure 4.3). Note here that $\mathbf{N}_P$, the normal at point of contact, passes through the centre of gravity of the cube, i.e. the momentum exchange is translational rather than rotational.

The "hard-cube" was first introduced in 1966 by Logan and Stickney [44] as a model for thermal scattering, where $\mathbf{N}_P = \mathbf{N}$. Note here that the model of Figure 4.3 is exactly equivalent to the hard-spheres model when the line between the two centres of mass at collision makes an angle α_P with the surface normal, i.e. Figures 4.3 and 4.4 are equivalent.

Adopting the notation of Figure 4.3 we see that, by setting $\phi = 0$ in Equation (3.8),

$$1 - \frac{V_r \cos(\xi_r + \alpha_P)}{V_i \cos(\xi_i - \alpha_P)} = \hat{\sigma} \qquad \text{..... (4.1)}$$

and, since the "cube" is smooth

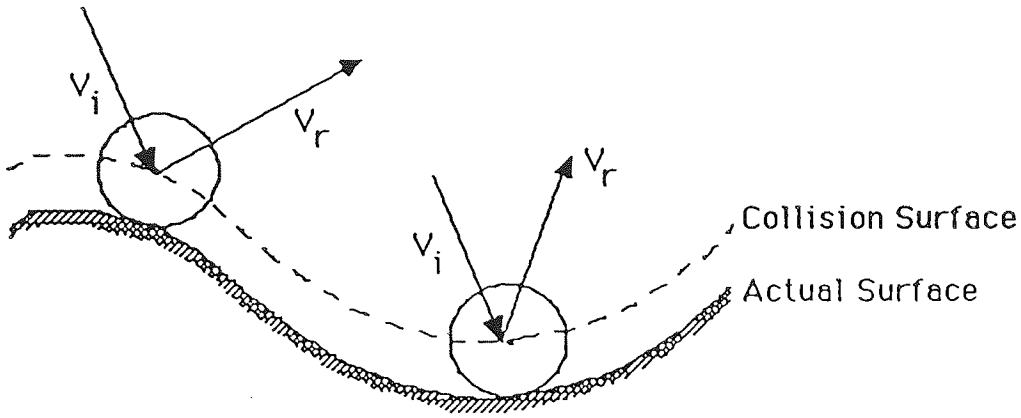

Figure 4.1 Relationship between collision and actual surfaces

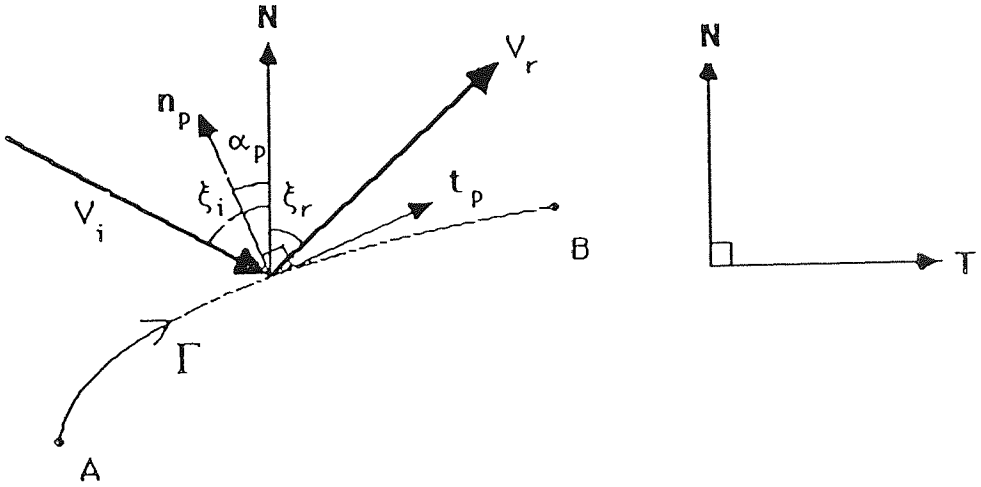

Figure 4.2 Generalised collision surface parameters

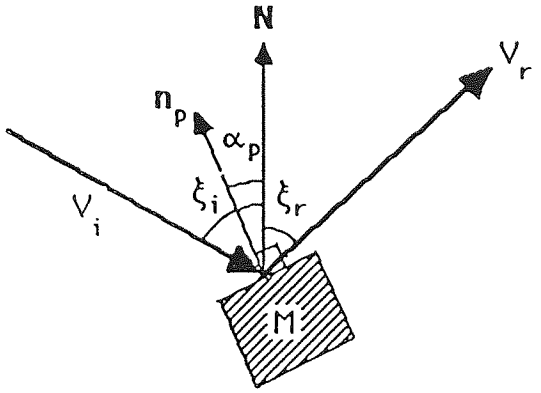

Figure 4.3 The hard-cubes model

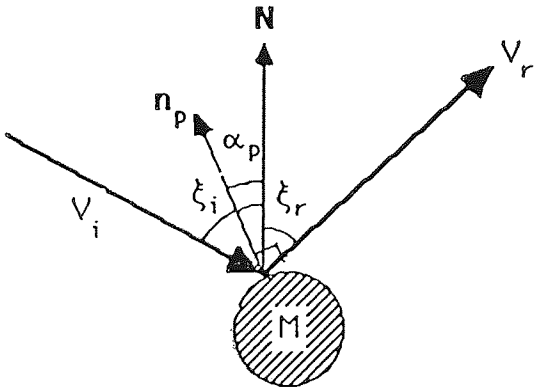

Figure 4.4 The hard-spheres model

$$V_r \sin(\xi_r + \alpha_P) = V_i \sin(\xi_i - \alpha_P). \qquad \text{..... (4.2)}$$

Thus by simple substitution between (4.1) and (4.2), we find that the angle of reflection, ξ_r, is given by

$$\tan(\xi_r + \alpha_P) = \frac{1}{1-\hat{\sigma}} \tan(\xi_i - \alpha_P) \qquad \text{..... (4.3)}$$

which can then be substituted back into (4.2) where

$$\frac{V_r}{V_i} = \frac{\sin(\xi_i - \alpha_P)}{\sin(\xi_r + \alpha_P)}. \qquad \text{..... (4.4)}$$

If the system consists of a very light gas particle striking a perfectly flat plane of "hard-cubes" then one collision only would suffice as the incident particle would always reflect away from the surface. However, we are implying for this analysis that there is noticeable surface structure and that further collisions are possible.

Multiple collisions are modelled in analogy with Goodman in that after collision we assume that the surface returns to its initial state (i.e. stationary "hard-cubes" arranged on the original curve Γ). This is basically for simplicity, assuming that the after-collision velocity of the surface particle is immediately dissipated throughout the body of the satellite.

Thus, we simply model the collision using the same system of equations as before, this time using

$$V_i = V_r \qquad \text{..... (4.5)}$$

$$\xi_i = \pi - \xi_r$$

to describe the incident state of the gas particle. We must determine the new value of α_P by finding where the particle will strike the surface again. We can now find the angle of reflection from (4.3) and the new velocity ratio from (4.4). The ratio of this second collision velocity with the original velocity is given by

$$\frac{V_{r\,\mathrm{NEXT}}}{V_i} = \frac{V_{r\,\mathrm{NEXT}}}{V_r} \cdot \frac{V_r}{V_i} \qquad \text{..... (4.6)}$$

where $V_{r\,\mathrm{NEXT}}$ is the current velocity of the particle.

Shadowing is another phenomenon of the collision where, dependent on the incident angle, the particle will only be able to "see" a certain portion of the surface, the remainder being hidden due to surface structure. This, as for multiple collisions, depends on the particular surface structure involved.

After many collisions, we find that the particle is reflected away from the surface at an angle of reflection $\xi_{r\,\mathrm{FINAL}}$ with velocity $V_{r\,\mathrm{FINAL}}$.

Thus:

$$\sigma' = 1 - \frac{V_{r\,\mathrm{FINAL}} \cos \xi_{r\,\mathrm{FINAL}}}{V_i \cos \xi_i} \qquad \text{..... (4.7)}$$

$$\sigma = 1 - \frac{V_{r\,\mathrm{FINAL}} \sin \xi_{r\,\mathrm{FINAL}}}{V_i \sin \xi_i}. \qquad \text{..... (4.8)}$$

Obviously, to account for surface structure and shadowing, many conditions and collisions are necessary, making numerical simulation unavoidable.

If we take the case of a single collision without shadowing, we may derive analytical results. For instance, in accordance with Equations (3.7) and (3.8), this case gives us:

$$\sigma' = 2 - \frac{1}{2}(2 - \hat{\sigma})\left[1 + \frac{\cos(\xi_i - 2\alpha_P)}{\cos \xi_i}\right] \qquad \text{..... (4.9)}$$

$$\sigma = \frac{1}{2}(2 - \hat{\sigma})\left[1 - \frac{\sin(\xi_i - 2\alpha_P)}{\sin \xi_i}\right]. \qquad \text{..... (4.10)}$$

If Γ is a continuous curve represented in a cartesian coordinate system, *Oxy*, by y(x), then

$$\sigma' = 2 - (2 - \hat{\sigma})\left[\frac{1}{1+d^2} + \frac{d}{1+d^2}\tan \xi_i\right] \qquad \text{..... (4.11)}$$

and

$$\sigma = (2 - \hat{\sigma})\left[\frac{d^2}{1+d^2} + \frac{d}{1+d^2}\cot \xi_i\right] \qquad \text{..... (4.12)}$$

where

$$d = \frac{dy}{dx}\Big|_P = \tan \alpha_P.$$

We must not underestimate that this is a special case - previous experience has shown us that multiple collisions are vital in such models and perhaps more study is necessary before we can attempt averages of Equations (4.9) and (4.10) over Γ.

If we take fully into account shadowing and multiple collisions, the conditions that have to be met make a consideration of a general surface impossible, and hence we will consider two idealised surface structures: a pyramidal and a "corrugated" model.

4.3 The Pyramidal and "Corrugated" Models

We consider that the surface may be represented as a regular 1-D array of two types: a simple arrangement of alternately sloped faces, forming pyramidal structures of inclination α_o; a "corrugated" array of alternately convex and concave circle arcs, each with half-angle α_o. (See Figures 4.5 and 4.6.)

For the pyramidal model, evenly distributed particles were fired at each slope (neglecting a slope when shadowing was present) and averages of σ' and σ were calculated, taking into account the proportion of the incident stream striking each face.

For the corrugated model a simple arrangement of target points on the surface would not truly reflect the proportion of particles striking it. A system similar to Goodman's was used, in that n points were evenly distributed in a line between A and B and a trajectory was chosen to go through each (Figure 4.5.).

Note that we confined calculation to be between points A and B for each surface (see Figures 4.5 and 4.6) as a particle falling here will not hit any part of the surface beyond A and B.

Modelling for the pyramidal structure was much easier, as each particle will strike the surface at the same incident angle and thus be reflected at the same reflection angle and at the same velocity. Shadowing is not a consideration for the initial collision as all particles will hit the surface with the same orientation; however, shadowing is important for reflected particles, as their starting position is necessary to determine if and where a second collision will occur.

For the corrugated surface shadowing is important at all stages. For the initial incident stream the shadowing is straightforward, but as the slope of the surface is continuously varying, the trajectory of each particle will differ as will its origin, thus meaning that the shadowing effects of the surface structure will differ from particle to particle.

When the mass ratio is high and/or the surface features are more prominent a high number of collisions will occur for a single particle. Thus, an upper limit on the number of collisions was set to be, arbitrarily, 50, after which it was assumed that total absorption by the surface would occur and both σ' and σ were set to unity.

For the pyramidal model, values for α_o of 15°, 30°, 45° and 60° were considered; for the corrugated model α was set to 30°, 60° and 90°.

For both models mass ratios of 0.1, 0.5 and 0.8 were considered, analogous with Goodman.

The results of the above are shown in Figures 4.7 to 4.18, with n = 100 for all cases.

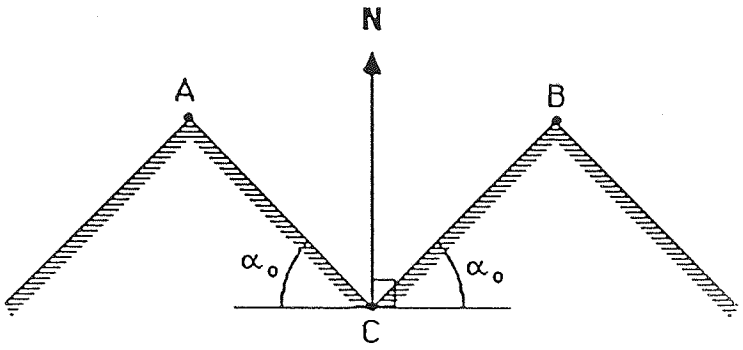

Figure 4.5 The pyramidal model

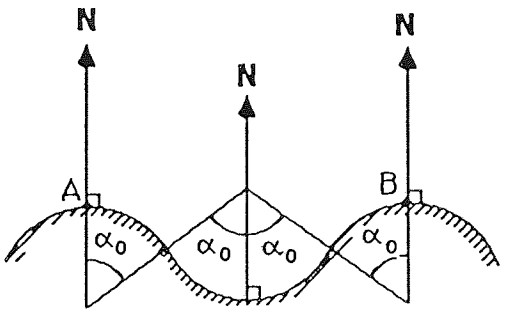

Figure 4.6 The corrugated model

4.4 Results and Discussion

Perhaps the most striking result of this simulation is the effect of increasing α in the pyramidal model on the normal momentum accommodation coefficient. Although σ' behaves as a general decreasing function of ξ_i, increasing the angle of the "pyramids" causes strongly aberrant behaviour for small angles of incidence.

At steeper angles of incidence a high proportion of particles are fully accommodated, and many are reflected out at similar angles, often producing behaviour uncharacteristic of continuous scattered distributions.

This is obvious for σ, where at small angles of incidence particles are reflected back in the same direction, causing values of σ very much greater than 1, or much less than 0, upsetting any continuous behaviour (Figures 4.10 to 4.12).

However, we can say that an increase in α does generally increase σ, although for continuous curves we must restrict ourselves to low values for α. This negates any chance for comparison with the high values of σ observed in experiment, and makes the pyramidal model unimportant for our uses.

The corrugated model produced much better results (Figures 4.13 to 4.18), resulting, in general, in continuous curves where behaviour can be clearly seen.

Perhaps the major deficiency of this model is that our choice of 100 initial trajectories was insufficient to produce smooth curves in some cases, a fact also recognised by Goodman. Figure 4.19 shows the effects of increasing n for σ when $\mu = 0.1$ and $\alpha_o = 30°$. Note that in each case the general behaviour of σ is clear.

Here we find little to contradict the qualitative results of the hard-spheres model in that σ' is a generally decreasing function of ξ_i, varying little with α_o, and that σ is, for the most part, constant, varying much with α_o but little with μ.

It would seem that, in conclusion, elastic models of gas-surface interaction generally behave the same, certainly underlining that for the majority of theoretical models, and for many experiments, good approximation to σ' and σ is achieved by

$$\sigma' = \sigma'_o - \sigma'_1 \sec \xi_i$$
$$\sigma = \text{const.} \qquad \text{..... (4.13)}$$

and that by adopting this, we exclude few theoretical possibilities.

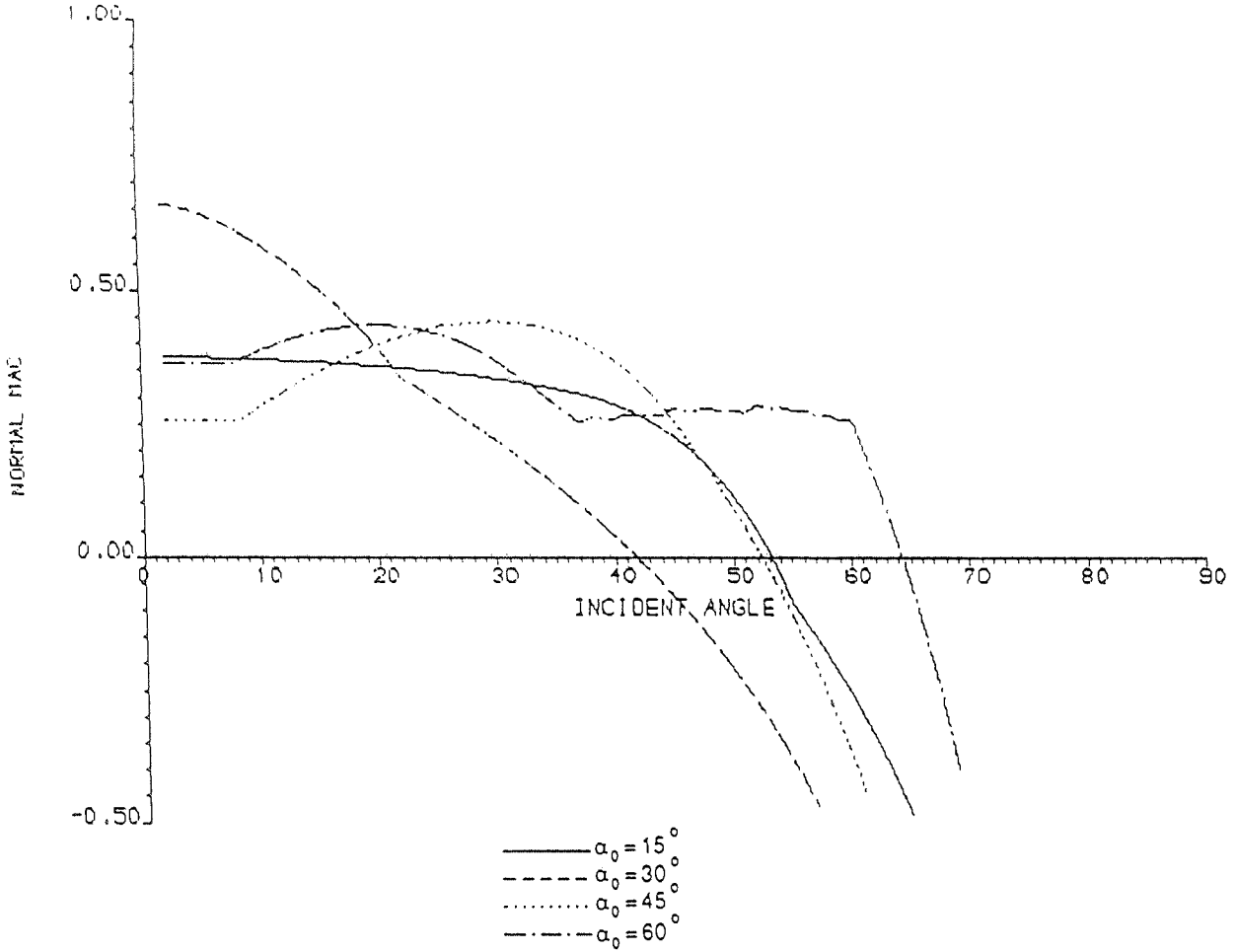

Figure 4.7 Normal Momentum Accomodation Coefficient (MAC) Simulation Results for the Pyramidal Model using μ=0.1

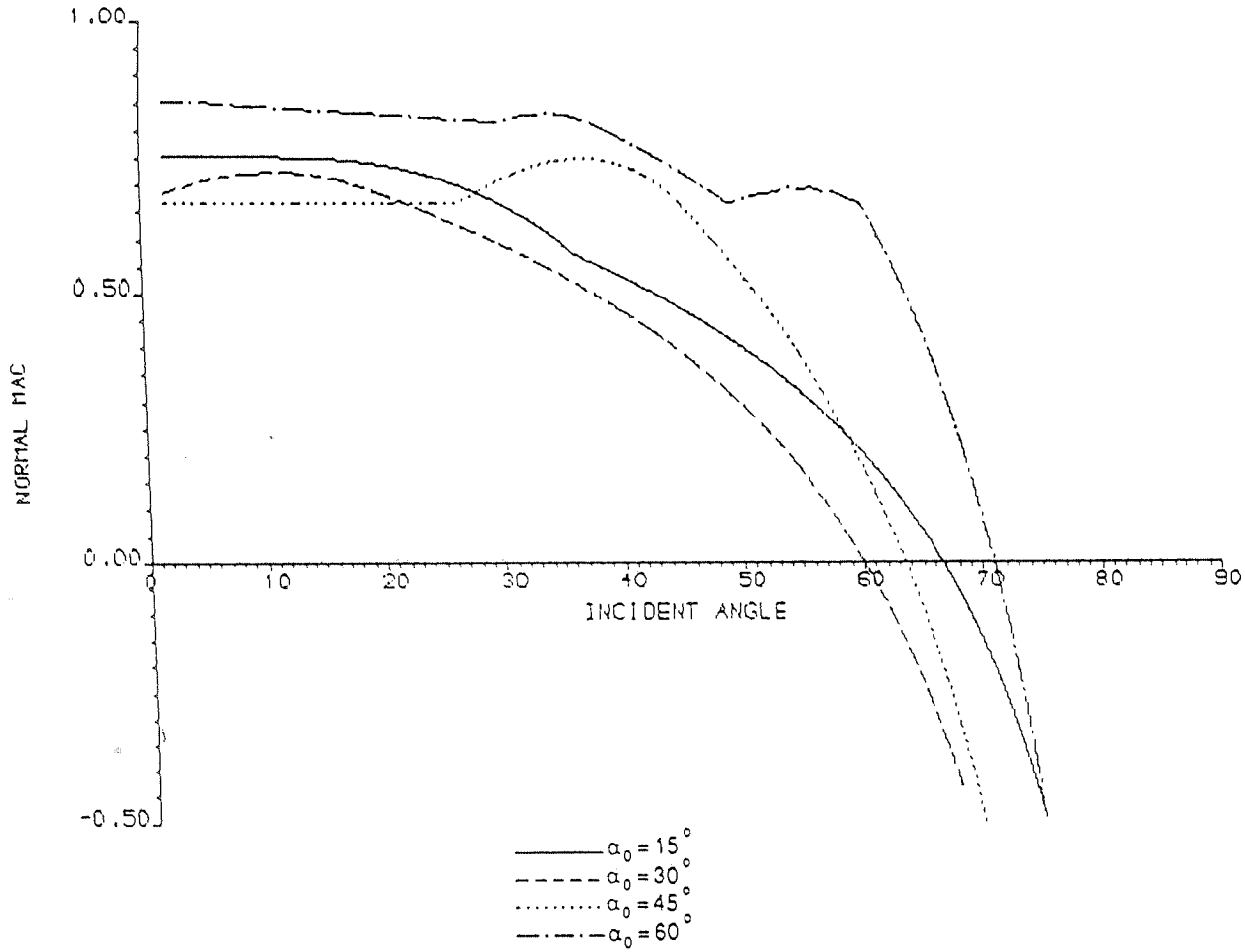

Figure 4.8 Normal MAC Simulation Results for the Pyramidal Model using μ=0.5

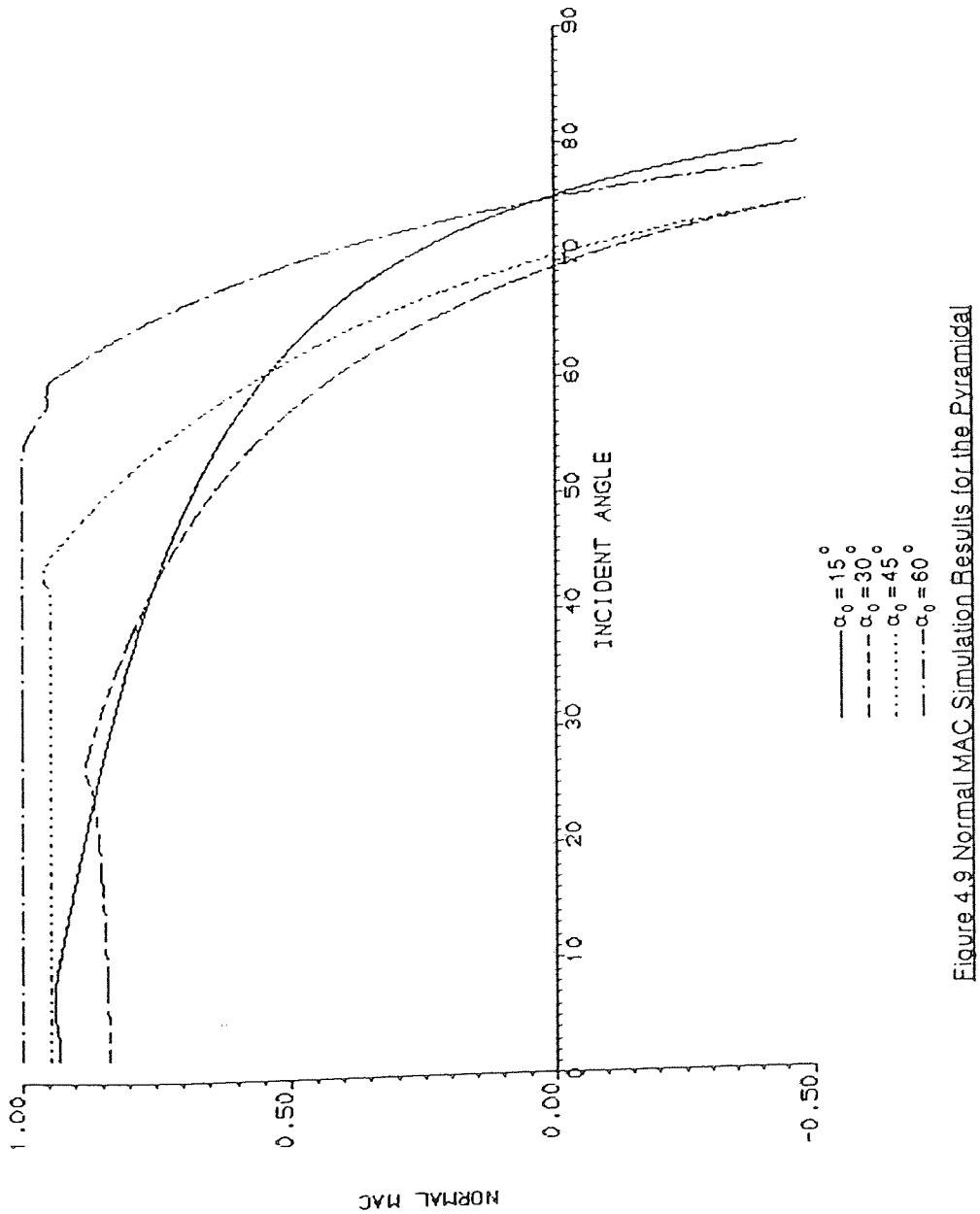

Figure 4.9 Normal MAC Simulation Results for the Pyramidal Model using μ=0.9

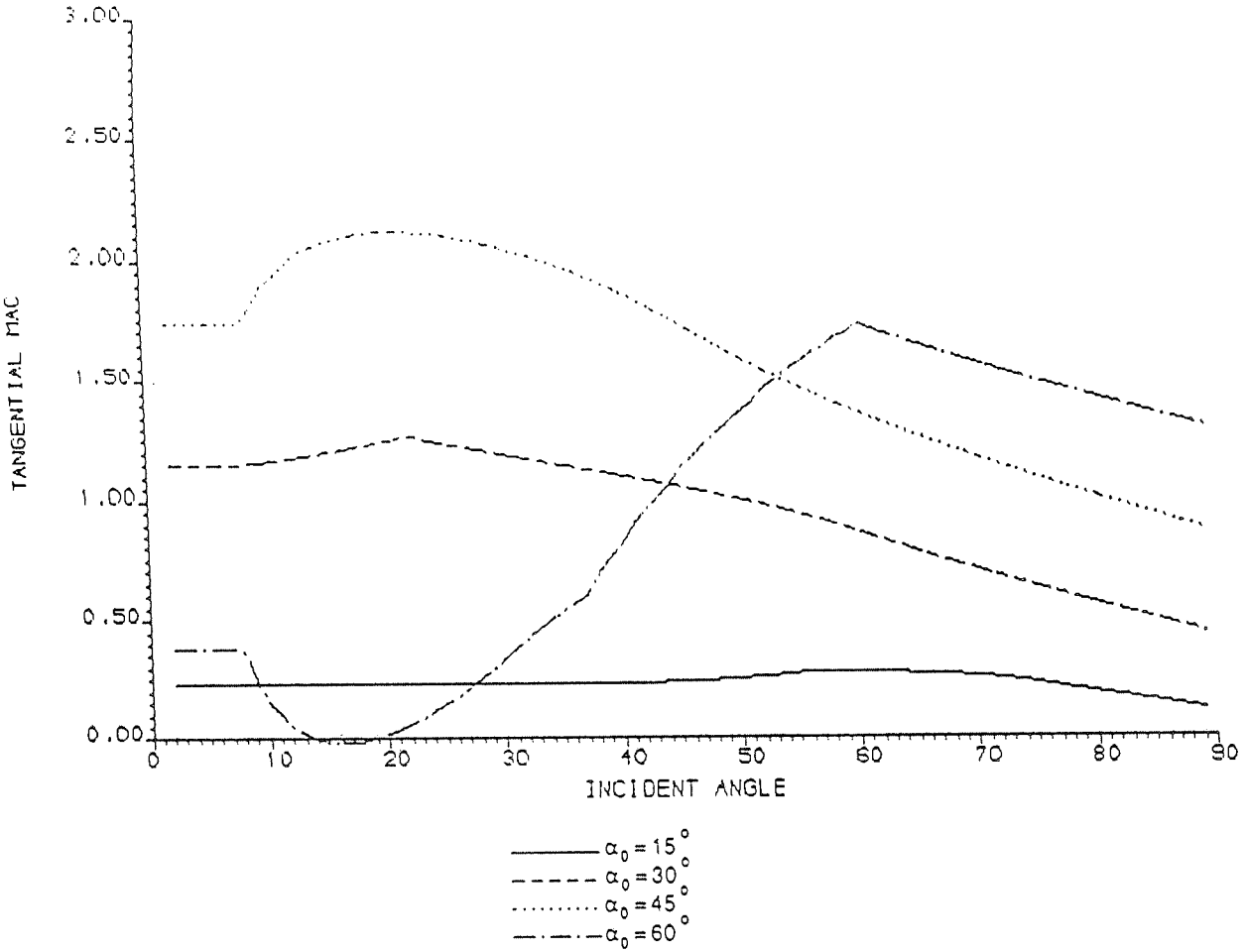

Figure 4.10 Tangential MAC Simulation Results for the Pyramidal Model using u=0.1

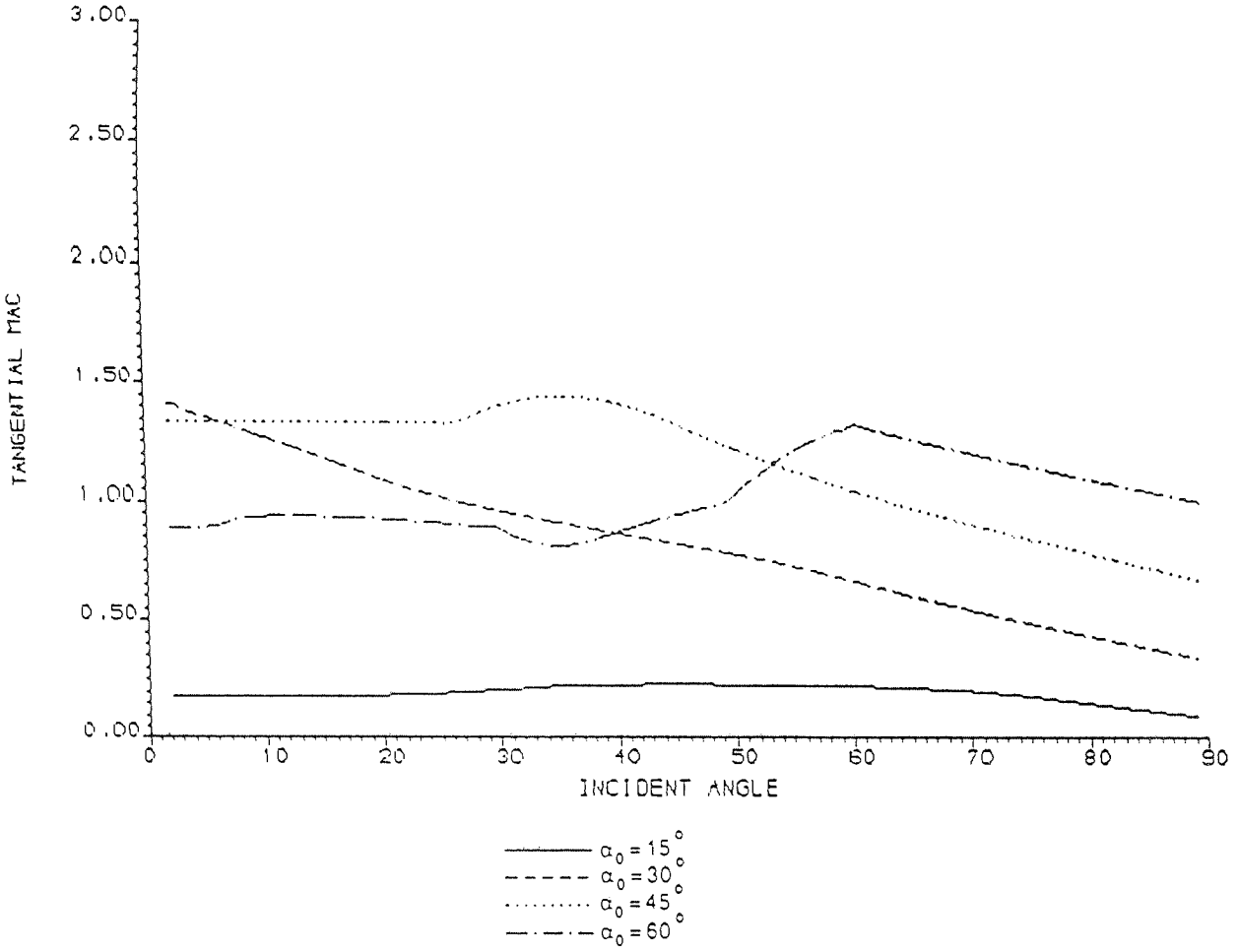

Figure 4.11 Tangential MAC Simulation Results for the Pyramidal Model using μ=0.5

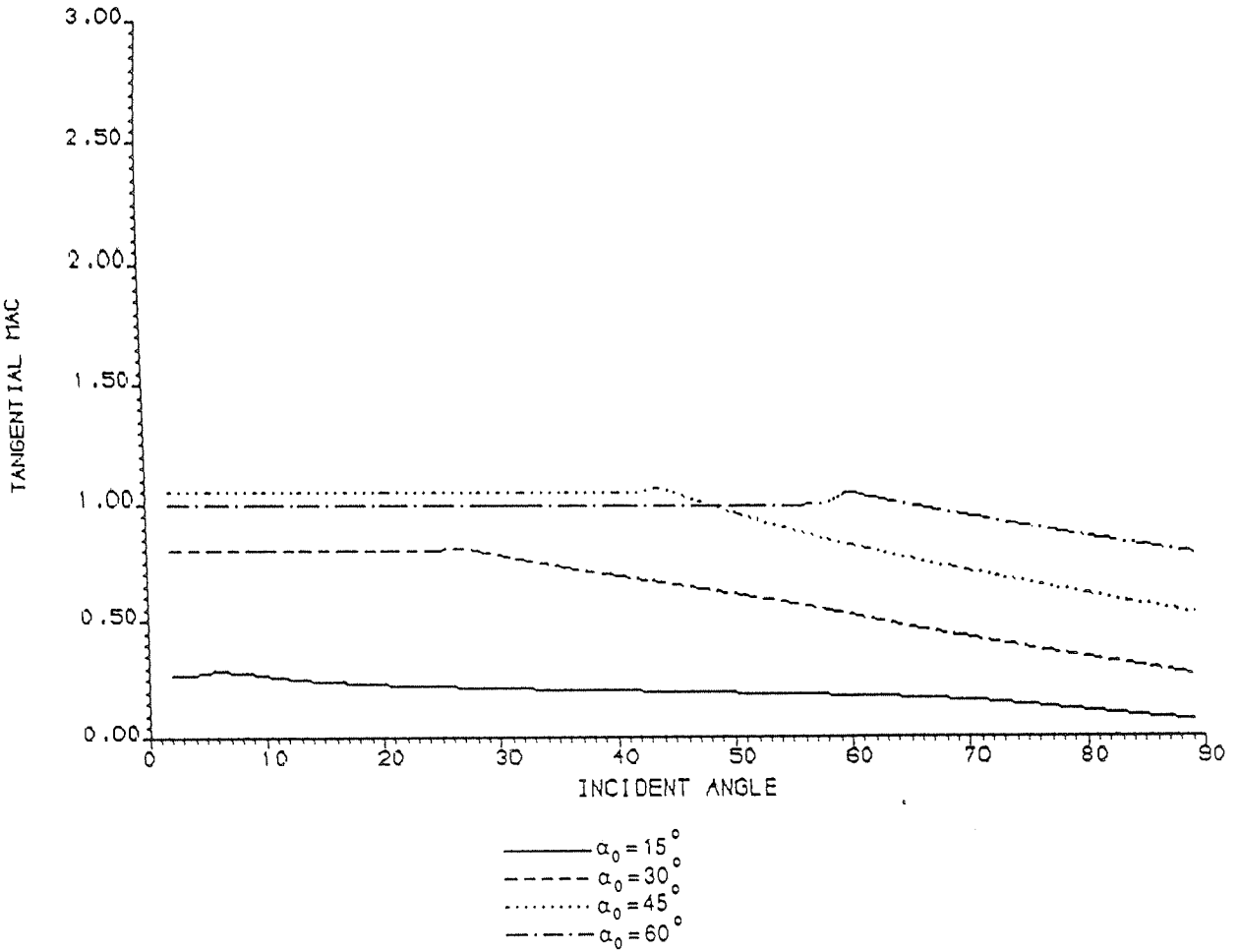

Figure 4.12 Tangential MAC Simulation Results for the Pyramidal Model using μ=0.9

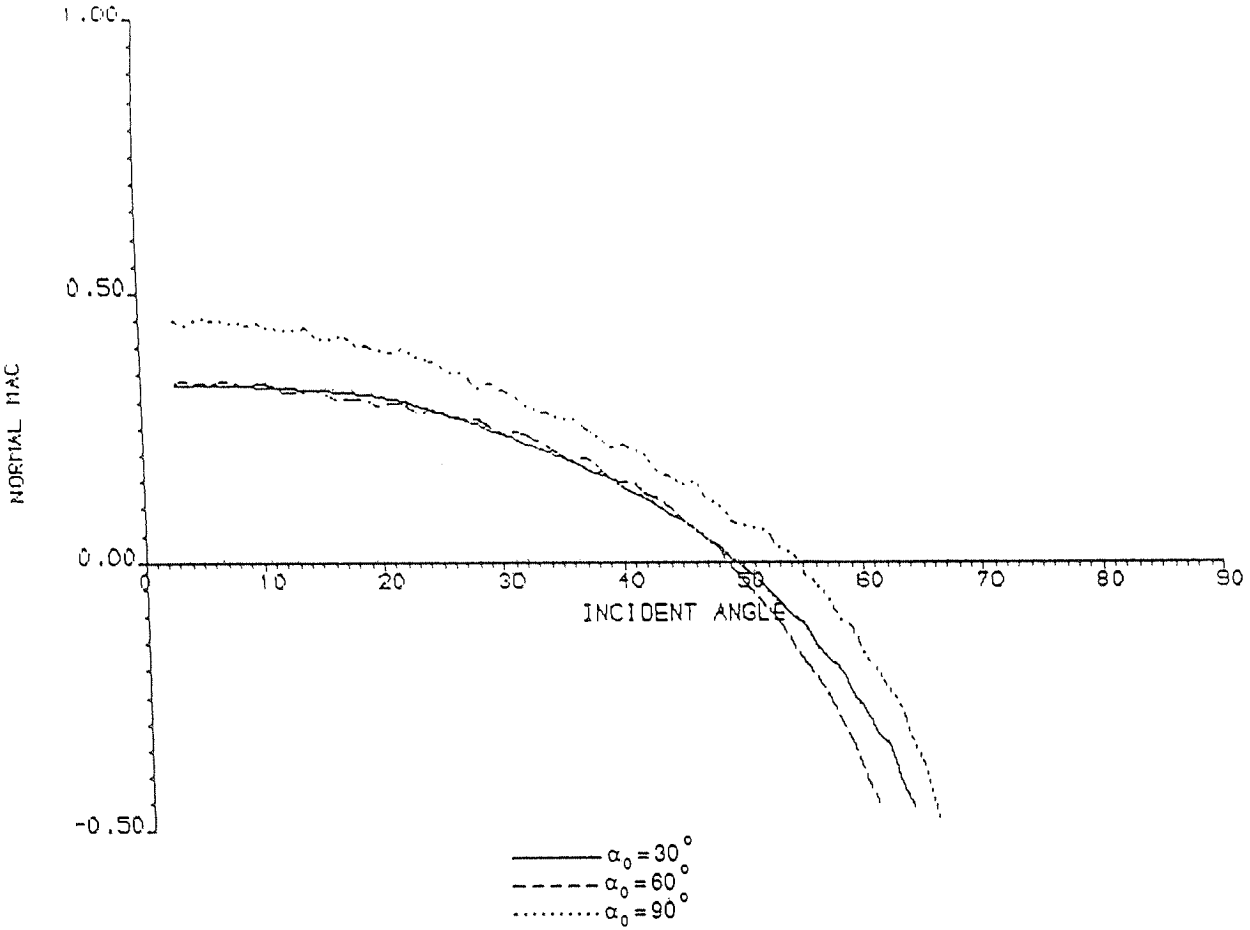

Figure 4.13 Normal MAC Simulation Results for the Corrugated Model using μ=0.1

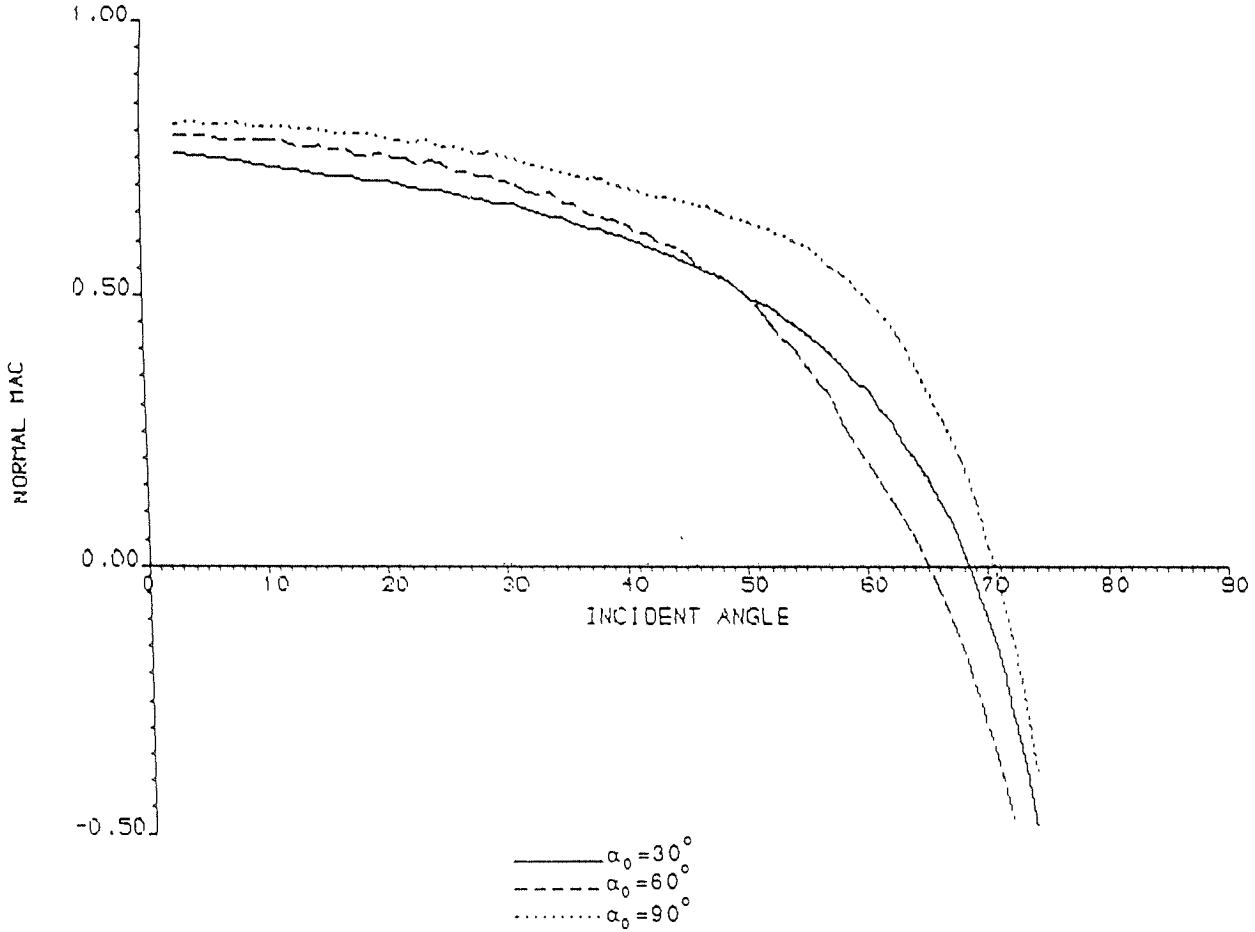

Figure 4.14 Normal MAC Simulation Results for the Corrugated Model using μ=0.5

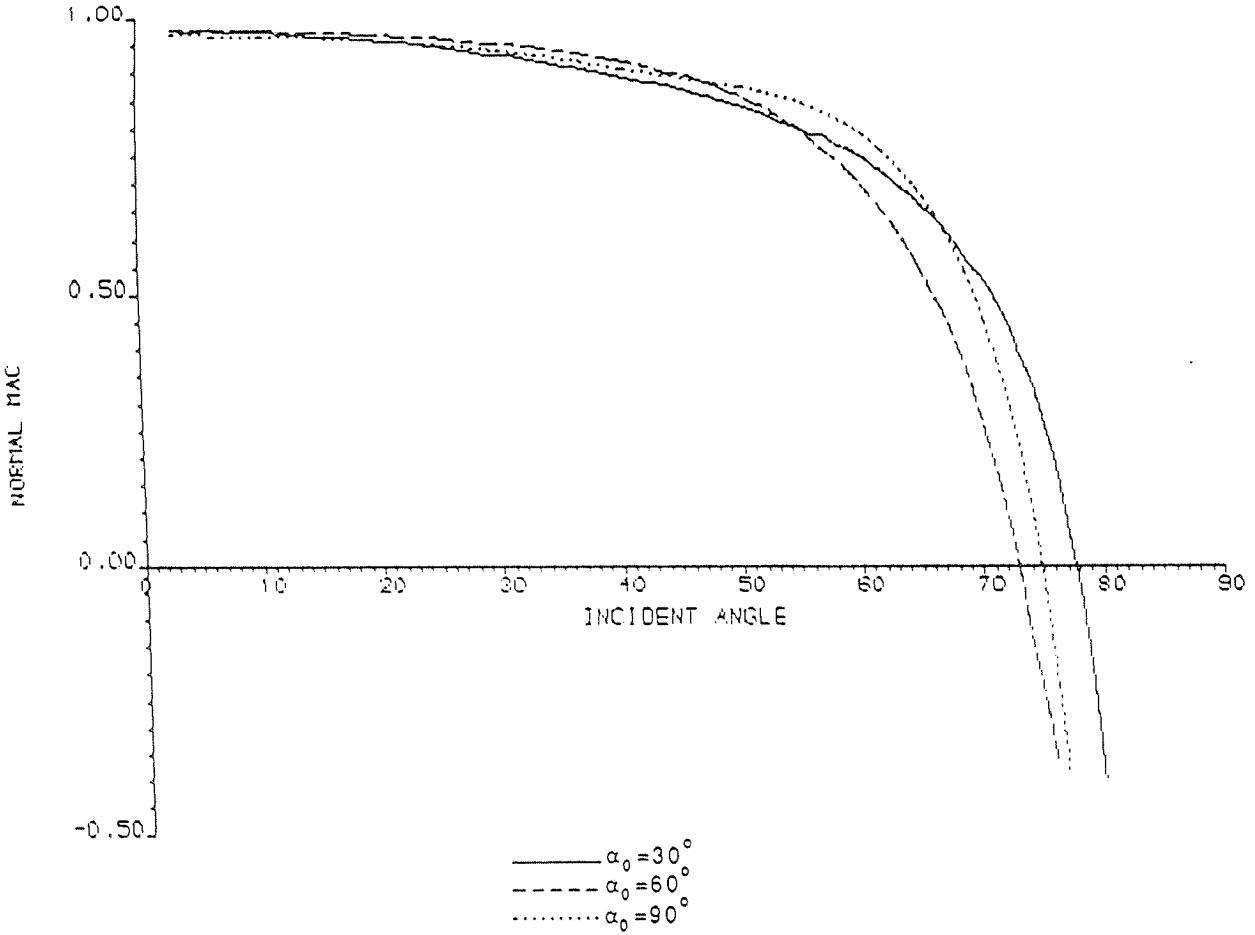

Figure 4.15 Normal MAC Simulation Results for the Corrugated Model using $\mu=0.9$

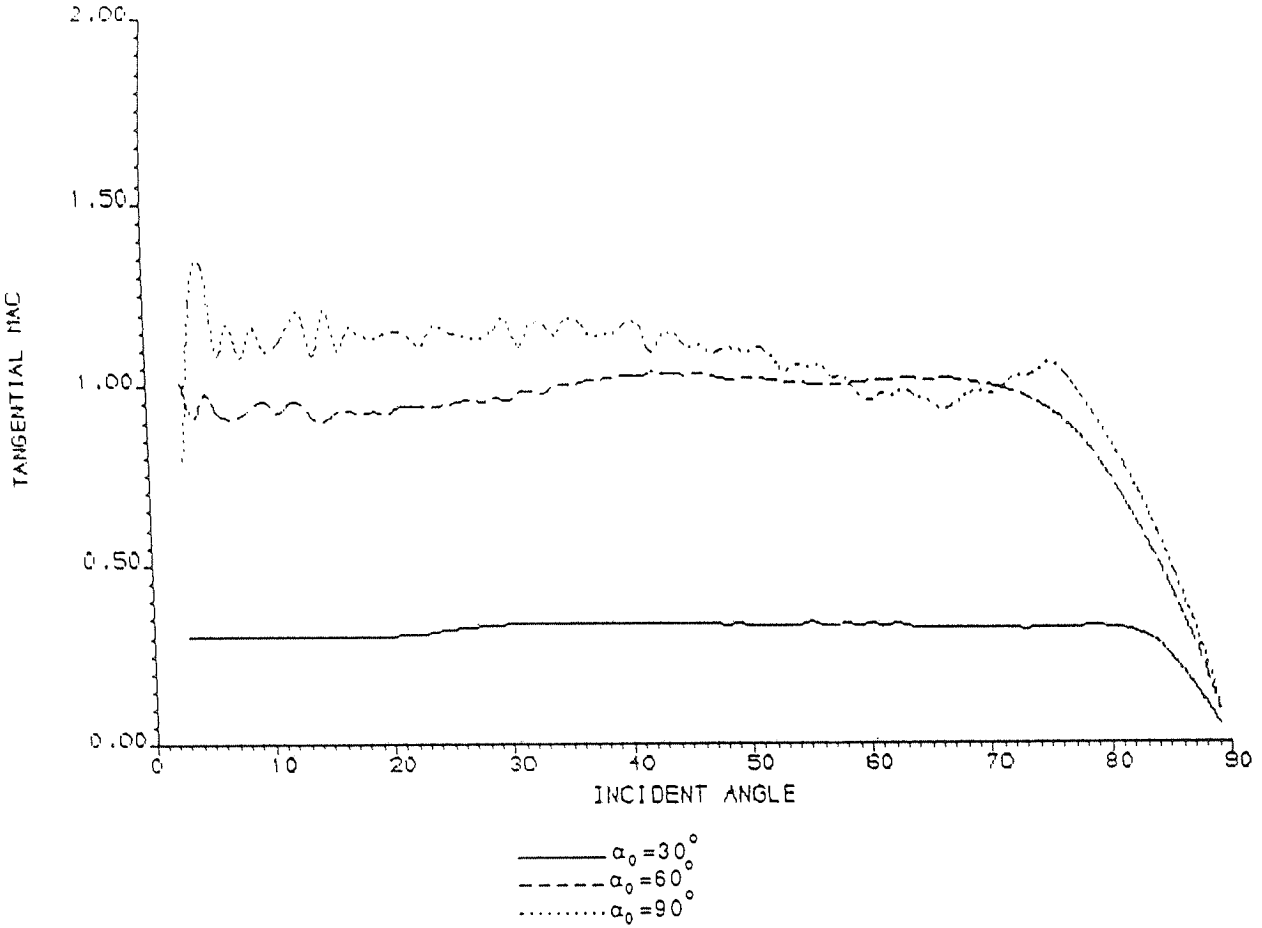

Figure 4.16 Tangential MAC Simulation Results for the Corrugated Model using μ=0.1

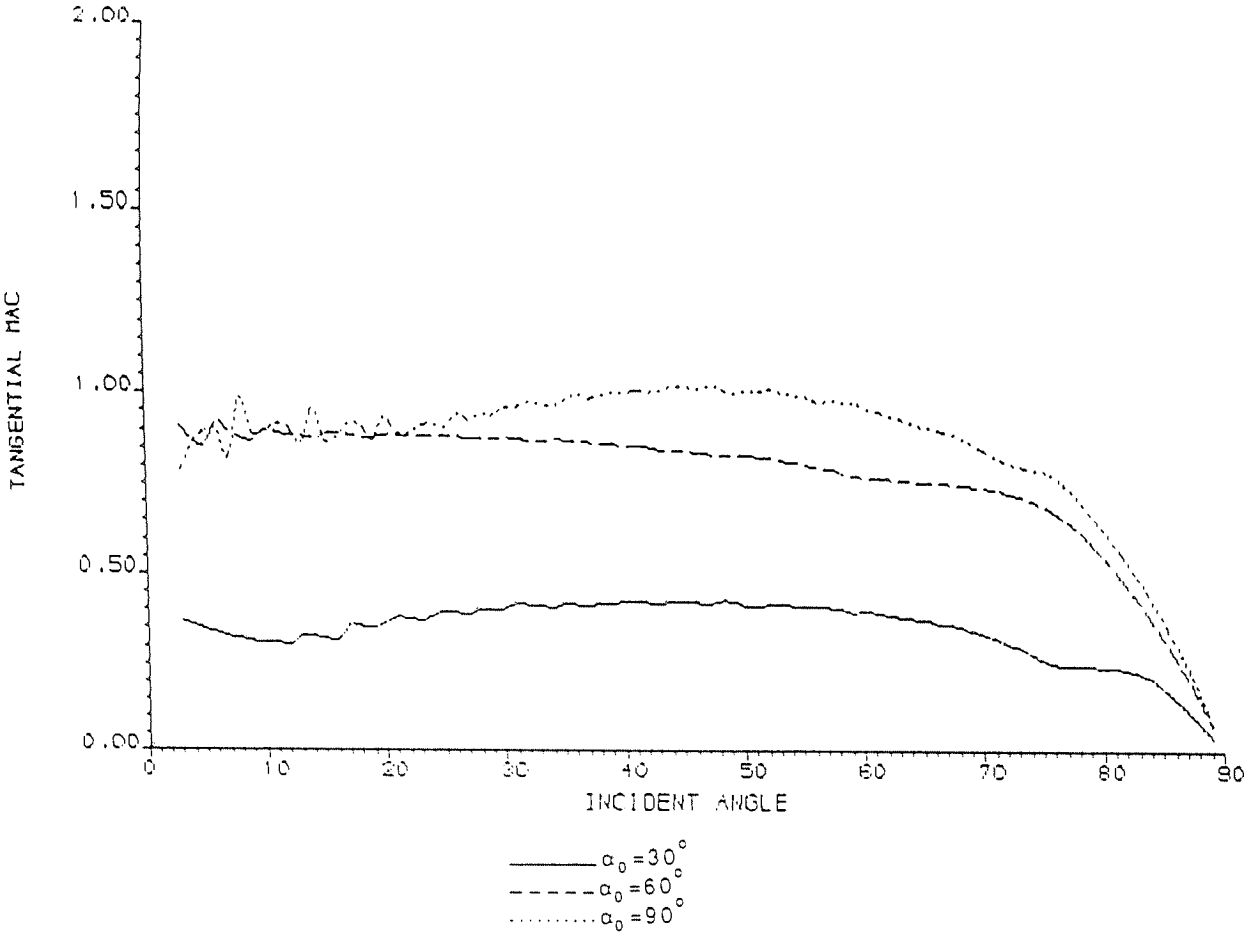

Figure 4.17 Tangential MAC Simulation Results for the Corrugated Model using μ=0.5

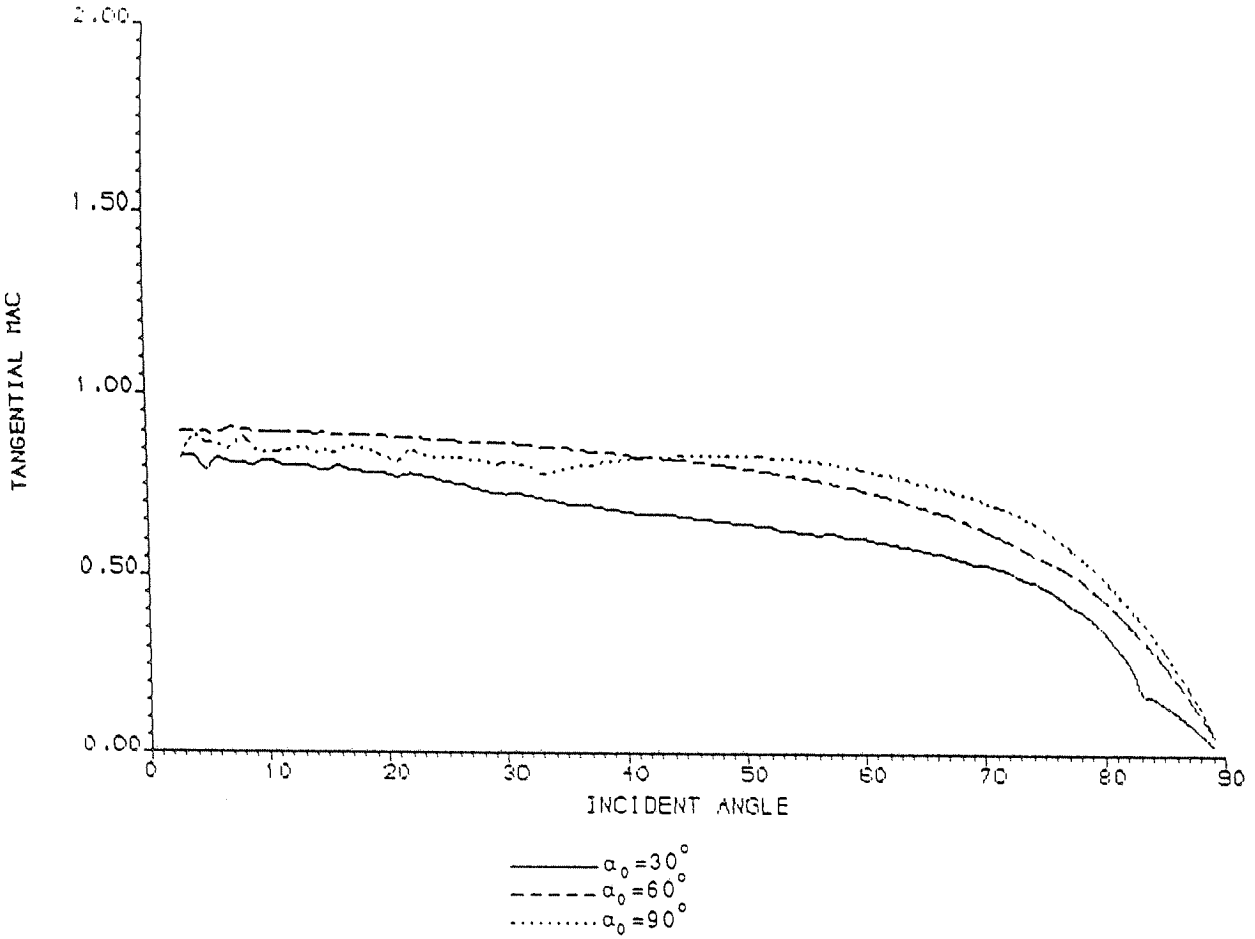

Figure 4.18 Tangential MAC Simulation Results for the Corrugated Model using μ=0.9

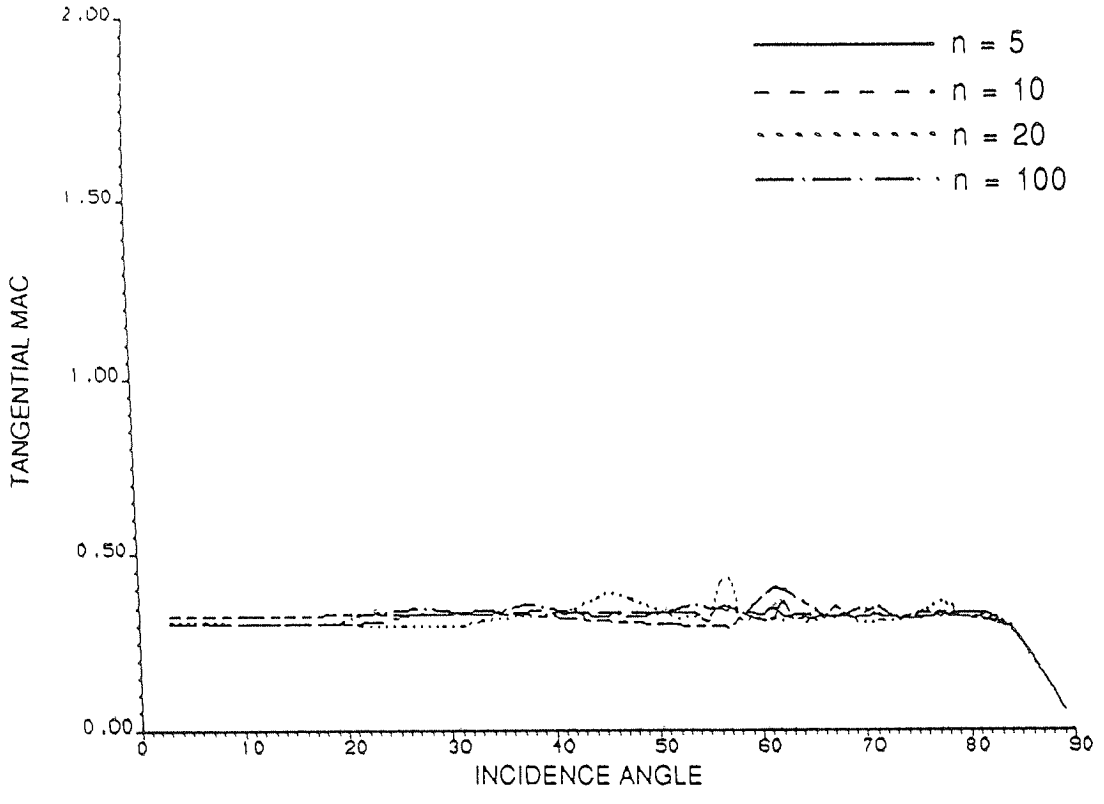

Figure 4.19 The Effect of Increasing n for the Corrugated Model where μ=0.1 and α_0 =30°

CHAPTER 5
THE PERTURBATIONS ON AN ORBITING SUN-ORIENTED FLAT PLATE IN AN OBLATE ATMOSPHERE

5.1 The Unperturbed Orbit

When an artificial satellite, mass M_S, orbits a spherical Earth of mass M_E, its path for a bounded orbit describes an ellipse with the centre of mass of the Earth at one of its focii. In plane polar coordinates, where r is distance of the satellite from the Earth's centre of mass, we find that

$$r = \frac{a(1-e^2)}{1+e\cos f} \qquad \text{..... (5.1)}$$

where f is the true anomaly or the angular distance from perigee or point of closest approach, a is the semi-major axis of the ellipse and e its eccentricity. (Figure 5.1.)

The orbital period, T, is given by

$$T = \frac{2\pi}{n} \qquad \text{..... (5.2)}$$

where n is the mean motion which is found from Kepler's

$$n^2 a^3 = \mu \qquad \text{..... (5.3)}$$

and $\mu = GM_E$ (assuming $M_S \ll M_E$) where G is the gravitational constant.

The polar Equation (5.1) of the orbit is often in an inconvenient form for analysis, and hence we may introduce the eccentric anomaly, E, which is related to the true anomaly, f, by

$$\begin{aligned} r\cos f &= a(\cos E - e) \\ r\sin f &= a(1-e^2)^{1/2}\sin E. \end{aligned} \qquad \text{..... (5.4)}$$

Thus the form of the polar Equation (5.1) is transformed to

$$r = a(1-e\cos E). \qquad \text{..... (5.5)}$$

If the absolute value of the satellite's velocity is equal to V, then it can be shown that:

$$V^2 = \frac{\mu}{p}\frac{1+e\cos E}{1-e\cos E} \qquad \text{..... (5.6)}$$

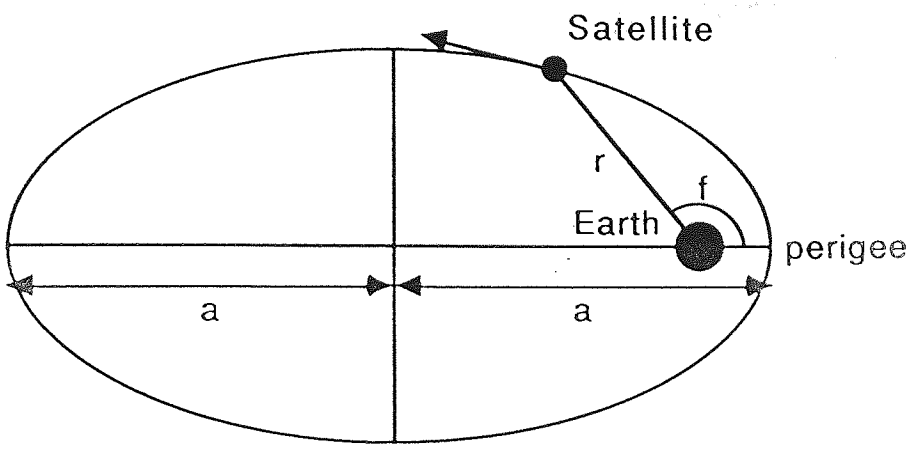

Figure 5.1 The Keplerian orbit

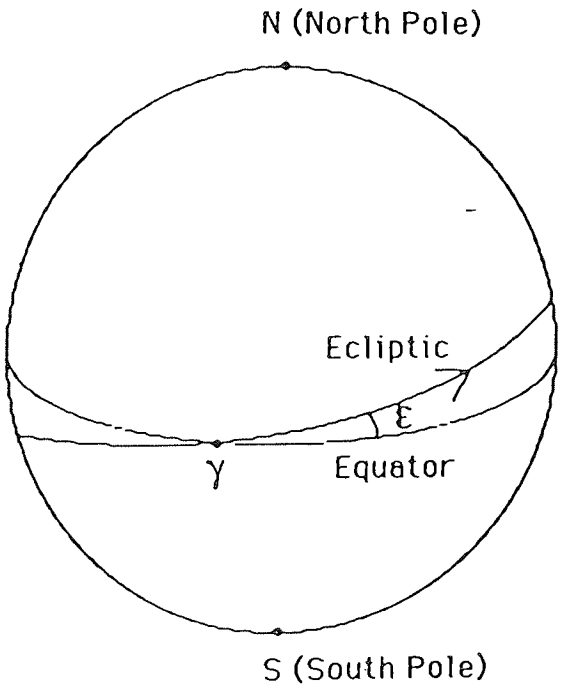

Figure 5.2 The equator and the ecliptic on the celestial sphere

where p is the semi-latus rectum, given by $p = a(1 - e^2)$.

To fix the orbit in space, say, relative to the star background, we consider that, due to the enormity of the distance involved, the stars can be said to be equidistant from the centre of the Earth, positioned on a spherical shell of unit radius - the Celestial Sphere. Thus, we see that any plane in space centred on the Earth intersects the Celestial Sphere as a great circle. Thus, the equatorial plane forms the Celestial Equator on the sphere and the Sun-Earth plane, or the ecliptic, forms the Celestial Ecliptic, which is inclined at an angle ε, the obliquity, to the equator.

When the Sun is travelling Northwards, or ascending, it crosses the equator at the First Point of Aries, which is the point γ in Figure 5.2.

Thus, we can position the satellites' orbit on the celestial sphere by Ω, the longitude of the ascending node, i, the inclination of the orbital plane to the equator and ω, the argument of perigee from the ascending node, which are shown in Figure 5.3. Notice that the satellite will generally be at position S, with argument $\omega + f$.

5.2 The Effects of a Perturbing Force

Consider that the satellite is subject to a small perturbing force F per unit mass. For aerodynamic considerations it is convenient to consider the components of F in the direction of velocity, the direction normal to the orbital plane and the outward normal to the orbit in the orbital plane. In Figure 5.4 we show a satellite-based coordinate system, as described above, with the y axis at a tangent and the x axis at the outward normal in the orbital plane; the z axis is the normal to the orbital plane and points out of the plane of the page.

The angle between the x axis and the radial direction is ψ, the angle of climb, which is given by [45]:

$$\cos\psi = \frac{1}{V}\sqrt{\left(\frac{\mu}{P}\right)}(1 + e\cos f)$$

$$\sin\psi = \frac{1}{V}\sqrt{\left(\frac{\mu}{P}\right)}\, e\sin f. \qquad \text{..... (5.7)}$$

Thus, we see that in this coordinate system the velocity vector $\underset{\sim}{V}$ is given by

$$\underset{\sim}{V} = \begin{bmatrix} O \\ V \\ O \end{bmatrix} \qquad \text{..... (5.8)}$$

where V is given in Equation (5.6).

If the components of F are F_1, F_2 and F_3 such that

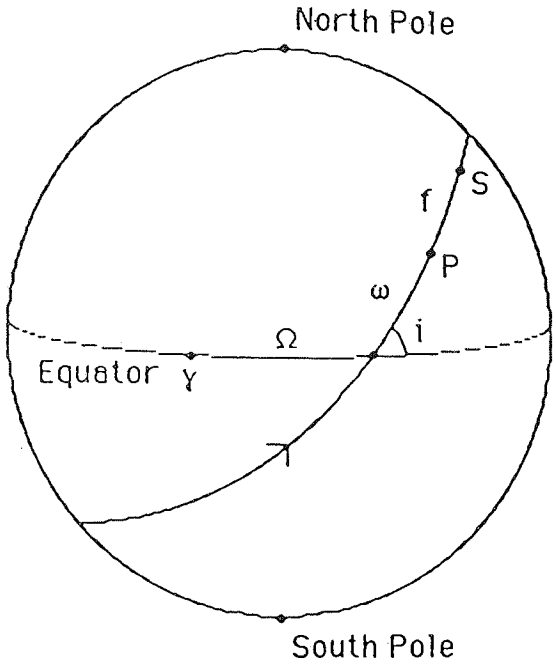

Figure 5.3 The orbital elements on the celestial sphere

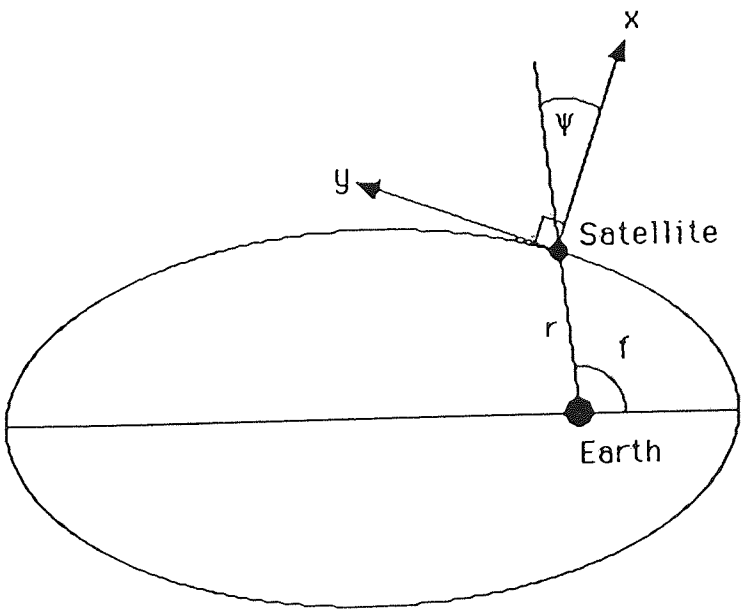

Figure 5.4 The satellite-based coordinate system

$$\mathbf{F} = \begin{bmatrix} F_1 \\ F_2 \\ F_3 \end{bmatrix} \qquad \text{..... (5.9)}$$

then the perturbations upon the elements a, e and i are given from Lagrange's Planetary Equations [46], as

$$\frac{da}{dE} = \frac{2ra^2V}{\mu}\left(\frac{a}{\mu}\right)^{1/2} F_2 \qquad \text{..... (5.10)}$$

$$\frac{de}{dE} = \frac{r}{V}\left(\frac{a}{\mu}\right)^{1/2}\left\{2F_2\left[e + \frac{a}{r}(\cos E - e)\right] + F_1(1-e^2)^{1/2}\sin E\right\} \qquad \text{..... (5.11)}$$

$$\frac{di}{dE} = \frac{ar}{\mu(1-e^2)^{1/2}}\{\cos\omega \,.\, \cos E - (1-e^2)^{1/2}\sin\omega \,.\, \sin E - e\cos\omega\}F_3. \qquad \text{..... (5.12)}$$

5.3 The Aerodynamic Forces on a Flat Plate in an Oblate Atmosphere

The force per unit mass experienced by a flat plate is normally resolved into two components: a drag force $\mathbf{F}_D$ acting along the direction of motion and lift force $\mathbf{F}_L$ which acts perpendicular to $\mathbf{F}_D$ in the plane of $\mathbf{F}_D$ and $\hat{\mathbf{n}}$, the unit normal to the surface

Suppose that, in our satellite based coordinate system,

$$\hat{\mathbf{y}} = \begin{bmatrix} 0 \\ 1 \\ 0 \end{bmatrix} \quad \text{and} \quad \hat{\mathbf{n}} = \begin{bmatrix} n_1 \\ n_2 \\ n_3 \end{bmatrix} \qquad \text{..... (5.13)}$$

then $\hat{\mathbf{l}}$, the unit vector in the lift direction, is given by:

$$\hat{\mathbf{l}} = \frac{\hat{\mathbf{y}} \times (\hat{\mathbf{n}} \times \hat{\mathbf{y}})}{|\hat{\mathbf{n}} \times \hat{\mathbf{y}}|}$$

$$= \frac{1}{(1-n_2^2)^{1/2}}\begin{bmatrix} n_1 \\ O \\ n_3 \end{bmatrix}. \qquad \text{..... (5.14)}$$

From a consideration of Figure 5.5 we notice that

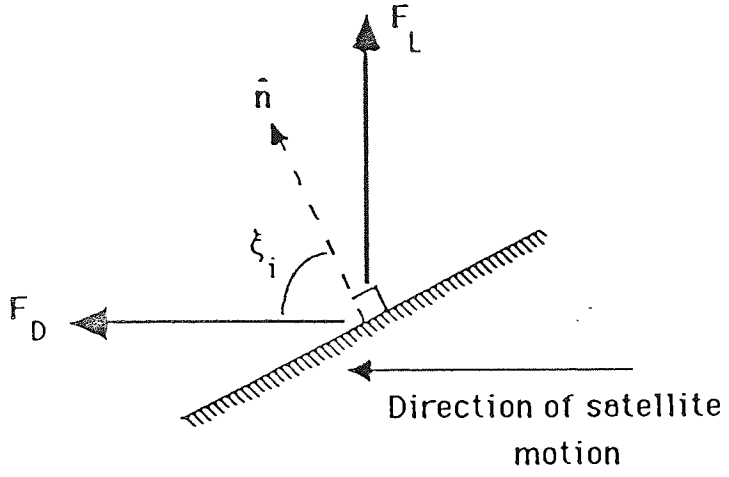

Figure 5.5 Drag and lift vectors on a flat plate

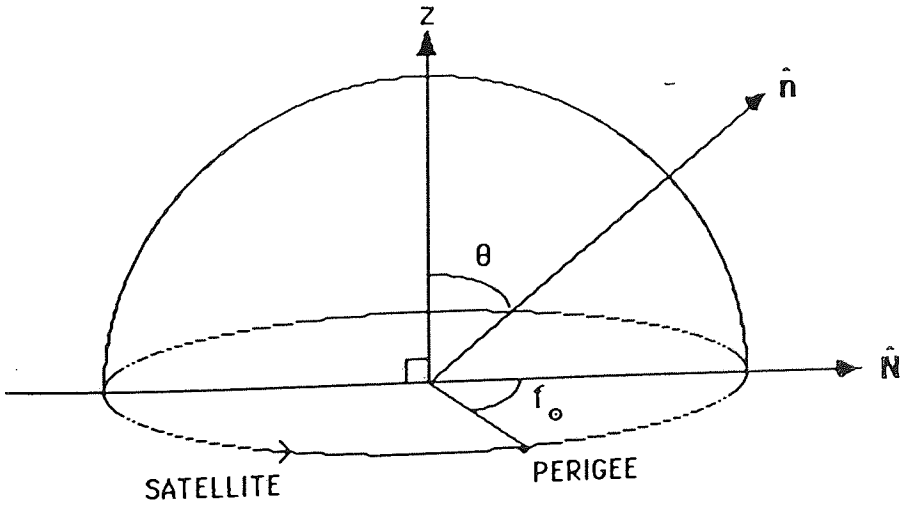

Figure 5.6 The normal to the flat plate relative to the satellite orbital plane

$$n_2 = \hat{\mathbf{n}} \cdot \hat{\mathbf{y}} = \cos\xi_i \qquad \text{..... (5.15)}$$

where ξ_i is the angle of incidence. Also, we must recognise that a condition that the atmosphere will strike the side of the plate with normal $\hat{\mathbf{n}}$ is that

$$n_2 > 0. \qquad \text{..... (5.16)}$$

In hyperthermal free-molecular flow, the drag and lift forces in the satellite-based coordinate system are:

$$\mathbf{F}_D = -\rho V^2 A_m [\sigma \cos\xi_i + (2 - \sigma' - \sigma)\cos^3\xi_i] \begin{bmatrix} 0 \\ 1 \\ 0 \end{bmatrix} \qquad \text{..... (5.17)}$$

$$\mathbf{F}_L = -\rho V^2 A_m (2 - \sigma' - \sigma)\cos^2\xi_i \quad \sin\xi_i \quad \hat{\mathbf{i}}.$$

where A_m is the ratio of the total area of the face of the plate turned towards the incident atmosphere and the mass of the satellite.

From the previous discussion on the behaviour of σ' and σ, we concluded that, empirically,

$$\sigma = \text{const.}$$

and

$$\sigma' = \sigma'_o - \sigma'_1 \cdot \sec\xi_i. \qquad \text{..... (5.18)}$$

Thus, using this information and Equations (5.14) and (5.15) we find

$$\mathbf{F}_D = -\rho V^2 A_m [\sigma n_2 + \sigma'_1 n_2^2 + (2 - \sigma'_o - \sigma) n_2^3] \begin{bmatrix} 0 \\ 1 \\ 0 \end{bmatrix}$$

..... (5.19)

$$\mathbf{F}_L = -\rho A_m V^2 [\sigma'_1 n_2 + (2 - \sigma'_o - \sigma) n_2^2] \begin{bmatrix} n_1 \\ 0 \\ n_3 \end{bmatrix}.$$

Thus, the components F_1, F_2 and F_3 of the force $\mathbf{F}$ on our satellite are given by:

$$\begin{aligned} F_1 &= -\rho A_m V^2 [\sigma'_1 n_2 + (2 - \sigma'_o - \sigma) n_2^2] n_1 \\ F_2 &= -\rho A_m V^2 [\sigma n_2 + \sigma'_1 n_2^2 + (2 - \sigma'_o - \sigma) n_2^3] \\ F_3 &= -\rho A_m V^2 [\sigma'_1 n_2 + (2 - \sigma'_o - \sigma) n_2^2] n_3. \end{aligned} \qquad \text{..... (5.20)}$$

All that remains to enable us to characterise the force on a flat plate is the express forms for the atmospheric density, ρ, and the unit normal to the side of the plate turned towards the incident stream, $\hat{\mathbf{n}}$.

For the density, ρ, we assume that it decreases exponentially with distance from the Earth's centre, the contours of constant density being oblate spheroids having the same ellipticity ε as the Earth ($\varepsilon \sim 0.00335$). Thus, if the density at the perigee height is ρ_p, it is found that [45]

$$\rho = \rho_p k_1 e^{z\cos E}[1 + c\cos 2(\omega + E) - 2ce\sin 2(\omega + E).\sin E + \frac{1}{4}c^2\{1 + \cos 4(\omega + E)\} + 0(c\varepsilon, c^2 e, e^2)] \quad \text{..... (5.21)}$$

where, if H is the density scale height:

$$z = \frac{ae}{H} \quad \text{..... (5.22)}$$

$$c = \frac{1}{2}\frac{r_p \varepsilon}{H}\sin^2 i \quad \text{..... (5.23)}$$

and

$$k_1 = e^{-z - c\cos 2\omega}. \quad \text{..... (5.24)}$$

5.4 The Normal to the Flat Plate

We assume here, that the normal to the plate, $\hat{\mathbf{n}}$, points towards some fixed point on the celestial sphere throughout the period of a single orbit. Thus, $\hat{\mathbf{n}}$ makes a fixed angle θ with the normal to the orbital plane and the projection of $\hat{\mathbf{n}}$ onto the orbital plane makes an angle $f_\odot$ with the semi-major axis (see Figure 5.6).

Here, $\hat{\mathbf{N}}$ is the projection of $\hat{\mathbf{n}}$ in the orbital plane.

In the satellite-based coordinate system, we consider that $\hat{\mathbf{N}}$ makes an angle φ with the x axis, or outward normal (Figure 5.7).

Here, we see that

$$\hat{\mathbf{n}} = \begin{bmatrix} \sin\theta\cos\phi \\ \sin\theta\sin\phi \\ \cos\theta \end{bmatrix}. \quad \text{..... (5.25)}$$

To find what φ is, we must consider the motion of the x and y axes in the orbital plane (Figure 5.8).

Hence, we see that the angle φ between $\hat{\mathbf{N}}$ and the x-axis is

$$\phi = f_\odot - f + \psi \quad \text{..... (5.26)}$$

where ψ is the angle of climb, given in Equation (5.7).

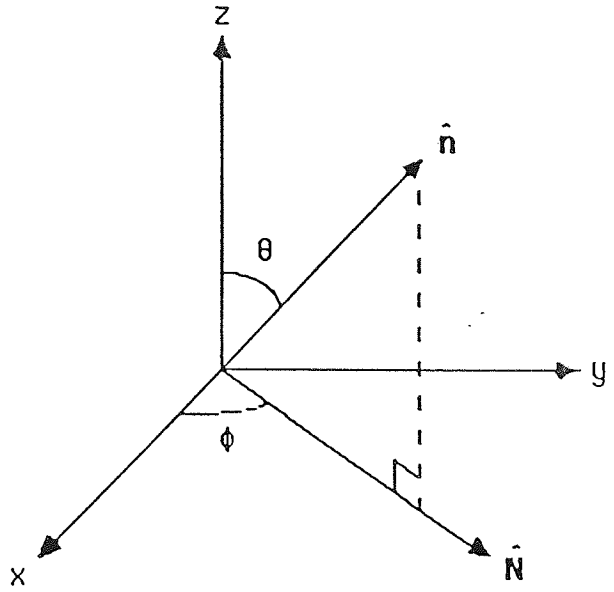

Figure 5.7 The normal to a flat plate in the satellite-based coordinate system

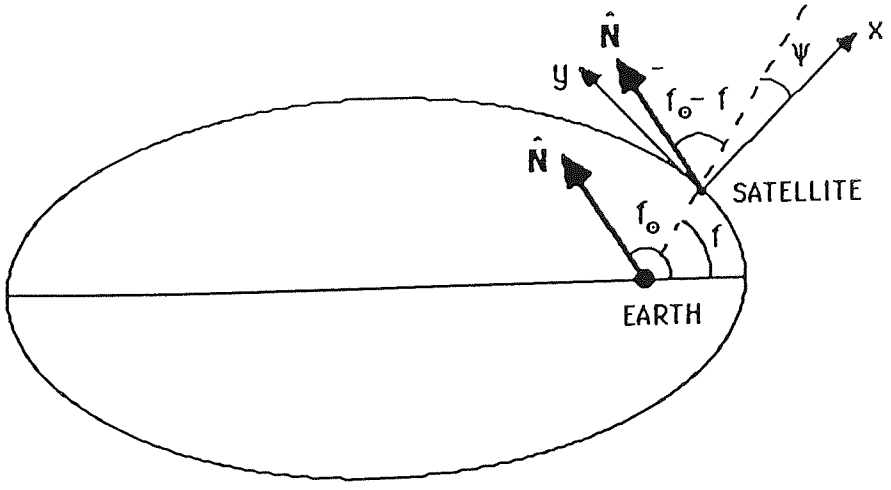

Figure 5.8 The flat plate normal projected into the orbital plane of the satellite

Now, the condition that the atmosphere will strike the side of the plate with normal $\hat{\mathbf{n}}$, given in Equation (5.16), is now

$$\sin\theta \sin\phi > 0 \qquad \text{..... (5.27)}$$

but since we choose $0 \le \theta \le \pi$, this condition becomes

$$\sin(f_\odot - f + \psi) > 0 \qquad \text{..... (5.28)}$$

i.e. that $0 \le f_\odot - f + \psi \le \pi$.

Physically, this means that at angles $\phi = 0$ and $\phi = \pi$ the satellite "flips", such that the side that was turned on stream is now shadowed, i.e. the normal to the "new" side is simply $-\hat{\mathbf{n}}$.

Thus, if $\hat{\mathbf{n}}$ is truly to be our normal to the incident surface, then we must define a new parameter ε which takes the value ± 1 depending on which side of the plate is facing the stream.

So, if one face of the curve always has normal $\hat{\mathbf{n}}^*$, then the normal to the side of the plate facing the stream is

$$\hat{\mathbf{n}} = \varepsilon \begin{bmatrix} \sin\theta.\cos\phi \\ \sin\theta.\sin\phi \\ \cos\theta \end{bmatrix} = \varepsilon\hat{\mathbf{n}}^* \qquad \text{..... (5.29)}$$

where, if $f_1^* = f_\odot + \psi$ and $f_2^* = (f_\odot + \psi) + \pi$,

$$\varepsilon = -1 \qquad \text{for } f_1^* \le f \le f_2^*$$

$$= +1 \qquad \text{elsewhere}$$

(f_1^* and f_2^* being the values of f for which $\sin\phi = 0$).

To allow a simple substitution for F_1, F_2 and F_3 into our perturbation equations, we must first convert all values of the true anomaly, f, to the corresponding values of the eccentric anomaly.

It can be shown, considering Equation (5.26), that

$$\sin\phi = \frac{1}{V}\sqrt{\frac{\mu}{p}}\{\sin(f_\odot - f) + e\sin f_\odot\} \qquad \text{..... (5.30)}$$

$$\cos\phi = \frac{1}{V}\sqrt{\frac{\mu}{p}}\{\cos(f_\odot - f) + e\cos f_\odot\}. \qquad \text{..... (5.31)}$$

The sign of ε changes when the plate is edge-on to the stream, i.e. at

$$\sin(f_\odot - f) + e \sin f_\odot = 0. \qquad \text{..... (5.32)}$$

We obtain two solutions of this equation (if we assume that $-\frac{\pi}{2} \le \sin^{-1} x \le \frac{\pi}{2}$), f_1^* and f_2^*, given by

$$f_1^* = f_\odot + \sin^{-1}(e \sin f_\odot)$$
$$f_2^* = \pi + f_\odot - \sin^{-1}(e \sin f_\odot). \qquad \text{..... (5.33)}$$

For the moment, we assume that all terms of $0(e^2)$ and above can be neglected. Thus recognising that the Taylor expansion of $\sin^{-1}x$ is

$$\sin^{-1} x = x + \frac{1}{2.3} x^3 + ... \qquad \text{..... (5.34)}$$

then

$$f_1^* = f_\odot + e \sin f_\odot + 0(e^3)$$
$$f_2^* = \pi + f_\odot - e \sin f_\odot + 0(e^3). \qquad \text{..... (5.35)}$$

The value ε can now be expressed in terms of f_1^* and f_2^*, as

$$\varepsilon = -1 \qquad \text{for } f_1^* \le f \le f_2^*$$
$$= 1 \qquad \text{elsewhere.} \qquad \text{..... (5.36)}$$

If $E_\odot$ and $r_\odot$ are the values of E and r corresponding to the point with true anomaly $f_\odot$, then from Equation (5.4)

$$r_\odot \cos f_\odot = a(\cos E_\odot - e)$$
$$r_\odot \sin f_\odot = a(1 - e^2)^{1/2} \sin E_\odot. \qquad \text{..... (5.37)}$$

We can show that

$$E_\odot = f_\odot - e \sin f_\odot + 0(e^2). \qquad \text{..... (5.38)}$$

Also, in terms of E and $f_\odot$, using $V = \left(\frac{\mu}{a}\right)^{1/2}(1 + e\cos E) + 0(e^2)$ and Equations (5.30) and (5.31)

$$\sin\phi = \sin(f_\odot - E) + 0(e^2) \qquad \text{..... (5.39)}$$
$$\cos\phi = \cos(f_\odot - E) + 0(e^2). \qquad \text{..... (5.40)}$$

We can now write down an expression for $\hat{\mathbf{n}}$ in terms of the eccentric anomaly such that

$$\hat{\mathbf{n}} = \varepsilon \begin{bmatrix} \sin\theta.\cos\phi \\ \sin\theta.\sin\phi \\ \cos\theta \end{bmatrix}$$

where $\sin\phi$ and $\cos\phi$ are given by (5.39) and (5.40) and, to order e^2,

$$\varepsilon = -1 \qquad \text{for} f_\odot < E < f_\odot + \pi \qquad \text{..... (5.41)}$$

$$= 1 \qquad \text{elsewhere.}$$

This is now in a suitable form for substitution into our perturbation Equations (5.10), (5.11) and (5.12), to order e^2,

$$\frac{da}{dE} = -2\rho a^2 A_m (1 + 2e\cos E)[\sigma'_1 \sin^2\theta \,.\, \sin^2\phi + \varepsilon\sigma \sin\theta \sin\phi + \varepsilon(2 - \sigma'_o - \sigma)\sin^3\theta \,.\, \sin^3\phi], \qquad \text{..... (5.42)}$$

$$\frac{de}{dE} = -\rho a A_m [\sigma'_1 \sin^2\theta \{2(1 + e\cos E)\cos E \,.\, \sin^2\phi + \sin E \sin\phi \,.\cos\phi\}$$
$$\varepsilon \,.\, (2 - \sigma'_o - \sigma)\sin^3\theta \{2(1 + e\cos E)\cos E \sin^3\phi + \sin E \,.\, \sin^2\phi \,.\, \cos\phi\} \qquad \text{..... (5.43)}$$
$$+ 2\varepsilon \,.\, \sigma \,.\, \sin\theta(1 + e\cos E)\cos E \sin\phi],$$

$$\frac{di}{dE} = -\rho a A_m (1 + e\cos E)\{\cos(\omega + E) - e\cos\omega\} \times$$
$$\times [\sigma'_1 \sin\theta \,.\, \cos\theta \,.\, \sin\phi + \varepsilon(2 - \sigma'_o - \sigma)\sin^2\theta \,.\, \cos\theta \sin^2\phi]. \qquad \text{..... (5.44)}$$

5.5 The Changes in a, e and i over a Single Orbital Period

If a_i is one of the orbital elements a, e and i then the change, Δa_i, in a_i over a single orbital period is given by:

$$\Delta a_i = \int_o^{2\pi} \frac{da_i}{dE} dE \qquad \text{..... (5.45)}$$

where here the integrand is given by one of the Equations (5.42), (5.43) or (5.44).

Analytically, this is hampered by our lack of knowledge as to the behaviour of the orbital parameters, excepting E, over an orbit. However, numerically, we can say that they change very little with respect to an orbital period, and hence

$$\frac{da_i}{dE} = \frac{\partial a_i}{\partial E} \qquad \text{..... (5.46)}$$

which means that in (5.45) we integrate explicitly only with respect to the eccentric anomaly. This is the method of averaging, as it is common to choose the mean values of the remaining parameters for the result.

We can rewrite the perturbation equations in the form:

$$\frac{da_i}{dE} = e^{z\cos E}\left\{\left[a_o + \sum_{n=1}^{\infty}(a_n \cos nE + b_n \sin nE)\right]\right. \qquad \text{..... (5.47)}$$

$$\left. + \varepsilon\left[c_o + \sum_{n=1}^{\infty} c_n \cos nE + d_n \sin nE\right]\right\}$$

where the a_n, b_n, c_n and d_n coefficients are constant over an orbital period.

In order to integrate (5.47), we must first notice that, if $I_n(z)$ is the modified Bessel function of the first kind and imaginary argument, then

$$\int_o^{2\pi} \cos nE \,.\, e^{z\cos E} dE = 2\pi I_n(z) \qquad \text{..... (5.48)}$$

$$n = 0, 1, \ldots.$$

$$\int_o^{2\pi} \sin nE \,.\, e^{z\cos E} dE = 0 \qquad \text{..... (5.49)}$$

$$n = 1, 2, \ldots. \quad .$$

If we define the functions C_n (z, $f_\odot$) and S_n(z, $f_\odot$) by:

$$C_n(z, f_\odot) = \frac{1}{\pi}\int_{f_\odot}^{f_\odot+\pi} \cos nE\, e^{z\cos E} dE \qquad \text{..... (5.50)}$$

$$n = 0, 1, \ldots.$$

$$S_n(z, f_\odot) = \frac{1}{\pi}\int_{f_\odot}^{f_\odot+\pi} \sin nE \,.\, e^{z\cos E} dE \qquad \text{..... (5.51)}$$

$$n = 1, 2, \ldots.$$

thus, we see that

$$\int_o^{2\pi} \varepsilon \cos nE e^{z\cos E} dE = 2\pi[I_n(z) - C_n(z, f_\odot)] \qquad \text{..... (5.52)}$$

and

$$\int_o^{2\pi} \varepsilon \sin nE \,.\, e^{z\cos E} dE = -2\pi S_n(z, f_\odot) \qquad \text{..... (5.53)}$$

where S_n and C_n are more fully discussed in the Appendix.

Thus, we see that

$$\Delta a_i = 2\pi\{\sum_{n=0}^{\infty} a_n I_n(z) + \sum_{n=0}^{\infty} c_n[I_n(z) - C_n(z, f_\odot)] - \sum_{n=1}^{\infty} d_n S_n(z, f_\odot)\}. \qquad \text{..... (5.54)}$$

The full solutions for a, e and i are given by

$$\begin{aligned}
\Delta a = -\rho_p k_1 a A_m \{ & -\frac{\pi}{8}[c^2 I_6 \cos(4\omega - 2f_\odot) + c^2 I_2 \cos(4\omega + 2f_\odot) + 4c(2eI_5 + I_4)\cos(2\omega - 2f_\odot) \\
& + 4c(2eI_1 + I_0)\cos(2\omega + 2f_\odot) + 2c^2 I_4 \cos 4\omega - 8c(2eI_3 + I_2)\cos 2\omega \\
& + 2(4eI_3 + (c^2+4)I_2 + 4I_1)\cos 2f_\odot - 16eI_1 - 2(c^2+4)I_0]\sigma'_1 \sin^2\theta \\
& -\frac{\pi}{4}[c^2 S_5 \cos(4\omega - f_\odot) - c^2 S_3 \cos(4\omega + f_\odot) + 4c(2eS_4 + S_3)\cos(2\omega - f_\odot) \\
& + c(cS_3 - 8eS_2)\cos(2\omega + f_\odot) + 2(4eS_2 + (c^2+4)S_1)\cos f_\odot \\
& - c^2 C'_5 \sin(4\omega - f_\odot) + c^2 C'_3 \sin(4\omega + f_\odot) - 4c(2eC'_4 + C'_3)\sin(2\omega - f_\odot) \\
& + 4c(2eC'_2 + C'_1)\sin(2\omega + f_\odot) + 2(4e(C'_2 - C'_0) + (c^2+4)C'_1)\sin f_\odot]\sigma \sin\theta \\
& + \frac{\pi}{16}[c^2 S_7 \cos(4\omega - 3f_\odot) + 4c(2eS_6 + S_5)\cos(2\omega - 3f_\odot) - 3c^2 S_5 \cos(4\omega - f_\odot) \\
& - 12c(2eS_4 + S_3)\cos(2\omega - f_\odot) + 2(4e(S_4 + S_2) + (c^2+4)S_3)\cos 3f_\odot \\
& + 3c^2 S_3 \cos(4\omega + f_\odot) + 12c(2eS_2 + S_1)\cos(2\omega + f_\odot) \\
& - 6(4eS_2 + (c^2+4)S_1)\cos f_\odot - c^2 S_1 \cos(4\omega + 3f_\odot) + 4cS_1 \cos(2\omega + 3f_\odot) \\
& - c^2 C'_7 \sin(4\omega - 3f_\odot) + 3c^2 C'_5 \sin(4\omega - f_\odot) + c^2 C'_1 \sin(4\omega + 3f_\odot) \\
& - 3c^2 C'_3 \sin(4\omega + f_\odot) - 4c(2eC'_6 + C'_5)\sin(2\omega - 3f_\odot) + 12c(2eC'_4 + C'_3)\sin(2\omega - f_\odot) \\
& + 4c(C'_1 + 2eC'_0)\sin(2\omega + 3f_\odot) - 12c(2eC'_2 + C'_1)\sin(2\omega + f_\odot) \\
& + 2(4e(C'_4 + C'_2) + (c^2+4)C'_3)\sin 3f_\odot - 6(4e(C'_2 + C'_0) + (c^2+4)C'_1)\sin f_\odot](2 - \sigma'_0 - \sigma)\sin^3\theta \\
& + O(e^2, c^3, c^2 e)\},
\end{aligned}$$

$$\Delta e = -\rho_p k_1 a A_m \{-\frac{\pi}{16}[c^2(I_7+3I_5)\cos(4\omega-2f_\odot)+c^2(3I_3+I_1)\cos(4\omega+2f_\odot)$$
$$+4(2ce(I_6+2I_4-I_2)+c(4I_5+3I_3))\cos(2\omega-2f_\odot)+16c(eI_2+I_1)\cos(2\omega+2f_\odot)$$
$$-8(ce(3I_4+2I_2-I_0)+2c(I_3+I_1))\cos 2\omega+2(4e(I_4+2I_2+I_0)+(c^2+4)(I_3+3I_1))\cos 2f_\odot$$
$$-16e(I_2+I_0)-8(c^2+4)I_1]\sigma'_1\sin^2\theta$$

$$-\frac{\pi}{4}[c^2(S_6+S_4)\cos(4\omega-f_\odot)-c^2(S_4+S_2)\cos(4\omega+f_\odot)$$
$$+2(ce(3S_5+2S_3+S_1)+2c(S_4+S_2))\cos(2\omega-f_\odot)-2(3ce(S_3+S_1)-2cS_2)\cos(2\omega+f_\odot)$$
$$+2((c^2+4)S_2+2e(S_1+S_3)\cos f_\odot-c^2(C'_6+C'_4)\sin(4\omega-f_\odot)+c^2(C'_4+C'_2)\sin(4\omega+f_\odot)$$
$$-2(ce(3C'_5+2C'_3-C'_1)+2c(C_4+C'_2))\sin(2\omega-f_\odot)$$
$$+2(ce(3C'_3+C'_1)+2c(C'_2+C'_0))\sin(2\omega+f_\odot)$$
$$+2(2e(C'_3+3C'_1)+(c^2+4)(C'_2+C'_0))\sin f_\odot]\sigma\sin\theta$$

$$+\frac{\pi}{32}[c^2(S_8+3S_6)\cos(4\omega-3f_\odot)-3c^2S_2\cos(4\omega+3f_\odot)+c^2(5S_6-7S_4)\cos(4\omega-f_\odot)$$
$$+c^2(7S_4+5S_2)\cos(4\omega+f_\odot)+4c(2e(S_7+2S_5-S_3)+(S_6+3S_4))\cos(2\omega-3f_\odot)$$
$$+4c(S_2-4eS_1)\cos(2\omega+3f_\odot)-4(4ce(2S_5+2S_3-S_1)+c(5S_4+7S_2))\cos(2\omega-f_\odot)$$
$$+4c(2e(5S_3+2S_1)+7Ssub2)\cos(2\omega+f_\odot)-2(12e(S_3+S_1)+5(c^2+4)S_2)\cos f_\odot$$
$$+2(4e(S_5+2S_3+S_1)+(c^2+4)(S_4+3S_2))\cos 3f_\odot$$
$$+c^2(5C'_6+7C'_4)\sin(4\omega-f_\odot)+c^2(3C'_2+C'_0)\sin(4\omega+3f_\odot)-c^2(7C'_4+5C'_2)\sin(4\omega+f_\odot)$$
$$+4c(2e(C'_7+2C'_5-C'_3)+C'_6+3C'_4)\sin(2\omega-3f_\odot)+4c(4e(2C'_5+2C'_3+C'_1)+5C'_4+7C'_2)\sin(2\omega-f_\odot)$$
$$+4c(C'_2+4eC'_1+3C'_0)\sin(2\omega+3f_\odot)-4c(2e(5C'_3+C'_1)+7C'_2+5C'_0)\sin(2\omega+f_\odot)$$
$$+2(4e(C'_5+2C'_3+C'_1)+(c^2+4)(C'_4+3C'_2))\sin 3f_\odot$$
$$-2(12e(C'_3+3C'_1)+(c^2+4)(5C'_2+7C'_0))\sin f_\odot](2-\sigma'_0-\sigma)\sin^3\theta+0(e^2,c^3,c^2e)\},$$

and

$$\Delta i = -\rho_{pk_1} a A_m [\frac{\pi}{16}\{S_7c^2\sin(5\omega-2f_\odot)+c^2S_3\sin(5\omega+2f_\odot)+[6ceS_6+c^2S_5+4cS_5+6ceS_4]\sin(3\omega-2f_\odot)$$
$$+2[e(c+2)(S_4-S_2)+(c^2+6)S_3]\sin(\omega-2f_\odot)-2S_5\sin 5\omega-2[6ce(S_4-S_2)+c(c+4)S_3]\sin 3\omega$$
$$+[c(c+4)S_1-6ceS_2]\sin(3\omega+2f_\odot)+2[e(c+2)S_2-(c^2+2c+4)S_1]\sin(\omega+2f_\odot)$$
$$-4[e(c+2)S_2+(c^2+2c+4)S_1\sin\omega$$

$$+c^2C'_7\cos(5\omega-2f_\odot)+c^2C'_3\cos(5\omega+2f_\odot)+c[6e(C'_6+C'_4)+(c+4)C'_5]\cos(3\omega-2f_\odot)$$
$$+c[6e(C'_2-C'_0)+(c+4)C'_1]\cos(3\omega+2f_\odot)+2[ce(C'_4-C'_2)+2(c+2)C'_3-2eC'_3]\cos(\omega-2f_\odot)$$
$$+2[e(c+2)(C'_0-C'_2)+(c^2+2c+4)C'_1]\cos(\omega+f_\odot)-2[6ce(C'_4-C'_2)+c(c+4)C'_3]\cos 3\omega$$

$$-2c^2C'_5\cos 5\omega - 4[e(c+2)(C'_2 - C'_c) + (c^2+2c+4)C'_1]\cos\omega\}(2-\sigma'_0-\sigma)\sin^2\theta\cos\theta$$

$$-\frac{\pi}{8}\{I_6c^2\sin(5\omega - f_\odot) - I_4c^2\sin(5\omega + f_\odot) + [6ce(I_5 - I_3) + c(c+4)I_4]\sin(3\omega - f_\odot)$$

$$-[6ce(I_3 - I_1) + c(c+4)I_2]\sin(3\omega + f_\odot) + 2[e(c+2)(I_3 - I_1) + (c^2+2c+4)I_2]\sin(\omega - f_\odot)$$

$$-2(c^2+2c+4)I_0\sin(\omega + f_\odot)\}\sigma'_1\sin\theta\cos\theta + 0(e^2, c^3, c^2e)],$$

where

$$C'_n = C_n(z, f_\odot) - I_n(z).$$

I_n is the modified Bessel function of argument z and S_n is the special function mentioned above and has arguments z and $f_\odot$.

For the special case of a spherically symmetric atmosphere, for which c = 0, we find that

$$\Delta a = -2\rho_p k_1 a^2 A_m\{-\frac{\pi}{8}[\{8e(I_3 + I_1) + 8I_2\}\cos 2f_\odot - 16eI_1 - 8I_0]\sigma'_1\sin^2\theta$$

$$-\frac{\pi}{4}[\{8eS_2 + 8S_1\}\cos f_\odot + \{8e(C'_2 - C'_0) + 8C'_1\}\sin f_\odot]\sigma\sin\theta$$

$$+\frac{\pi}{16}[\{8e(S_4 + S_2) + 8S_3\}\cos 3f_\odot + \{8e(C'_4 + C'_2) + 8C'_3\}\sin 3f_\odot$$

$$-\{24eS_2 + 24S_1\}\cos f_\odot - \{24e(C'_2 + C'_0) + 24C'_1\}\sin f_\odot](2 - \sigma'_0 - \sigma)\sin^3\theta + 0(e^2, c^3, c^2e)\},$$

$$\Delta e = -\rho_p k_1 a A_m\{-\frac{\pi}{16}[\{8e(I_4 + 2I_2 + I_0) + 8I_3 + 24I_1\}\cos 2f_\odot$$

$$-16e(I_2 + I_2) - 32I_1]\sigma'_1\sin^2\theta$$

$$+\frac{\pi}{32}[\{8e(S_5 + 2S_3 + S_1) + 8S_4 + 24S_2\}\cos 3f_\odot$$

$$-\{24e(S_3 + S_1) + 40S_2\}\cos f_\odot$$

$$+\{8e(C'_5 + 2C'_3 + C'_1) + 8C'_4 + 24C'_2\}\sin 3f_\odot$$

$$-\{24e(C'_3 + 3C'_1) + 40C'_2 + 56C'_0\}\sin f_\odot](2 - \sigma'_0 - \sigma)\sin^3\theta$$

$$-\frac{\pi}{4}[\{4e(S_3 + S_1) + 8S_2\}\cos f_\odot$$

$$+\{4e(C'_3 + 3C'_1) + 8C'_2 + 8C'_0\}\sin f_\odot]\sigma\sin\theta + 0(e^2, c^3, c^2e)\},$$

$$\Delta i = -\rho_p k_1 a A_m \{-\frac{\pi}{8}[4e(I_3 - I_1) + 8I_2]\sin(\omega - f_\odot) - 8I_0 \sin(\omega + f_\odot)]\sigma'_1 \sin\theta\cos\theta$$

$$+\frac{\pi}{16}[(4e(S_4 - S_2 + 12S_3)\sin(\omega - 2f_\odot) - 2S_5 \sin 5\omega + \{4eS_2 - 8S_1\}\sin(\omega + 2f_\odot)$$

$$-\{8eS_2 - 16S_1\}\sin\omega + \{8C'_3 - 4eC'_2\}\cos(\omega - 2f_\odot)$$

$$+\{4e(C'_0 - C'_2) + 8C'_1\}\cos(\omega + 2f_\odot) + 0(e^2, c^3, c^2 e)$$

$$+\{8e(C'_0 - C'_2) - 16C'_1\}\cos\omega](2 - \sigma'_0 - \sigma)\sin^2\theta\cos\theta\},$$

which, although simplified, serves to illustrate the complexity and size of the equations used in this study.

The introduction of the functions $I_n(z)$, $C_n(z, f_\odot)$ and $S_n(z, f_\odot)$ means that we now have all of the tools available to model the aerodynamics of an oriented flat-plate. The only unknowns that arise are the specific form of the orientation vector $\hat{\mathbf{n}}$, expressly in terms of the parameters θ and $f_\odot$.

5.6 The Sun-Oriented Flat Plate

We have already stated that the normal to a flat plate may be described in terms of the angles θ and $f_\odot$ (see Section 5.4). If we consider this to be the Sun direction, $\mathbf{r}_\odot$, then in the satellite based coordinate system this is, using Equations (5.39) and (5.40) in Equation (5.25),

$$\mathbf{r}_\odot = \begin{bmatrix} \sin\theta_\odot \cos(f_\odot - E) \\ \sin\theta_\odot \sin(f_\odot - E) \\ \cos\theta_\odot \end{bmatrix}. \qquad \text{..... (5.55)}$$

In the Earth-centred coordinate system, shown in Figure 5.9, $\mathbf{r}_\odot$ can be defined in terms of the right ascension $\alpha_\odot$ and declination $\delta_\odot$ of the Sun.

Explicitly $\mathbf{r}_\odot$ is given by $\mathbf{r}^{\mathbf{E}}_\odot$, where

$$\mathbf{r}^{\mathbf{E}}_\odot = \begin{bmatrix} \cos\delta_\odot \cos\alpha_\odot \\ \cos\delta_\odot \sin\alpha_\odot \\ \sin\alpha_\odot \end{bmatrix}. \qquad \text{..... (5.56)}$$

Now, we can rotate $\mathbf{r}^{\mathbf{E}}_\odot$ through a number of angles and axes successively such that it is comparable to Equation (5.55) and hence we can solve for $\theta_\odot$ and $f_\odot$. This is made easier if we only consider the satellite at perigee, such that the mean and true anomalies are both zero. Here, we see that (5.55) is equal to

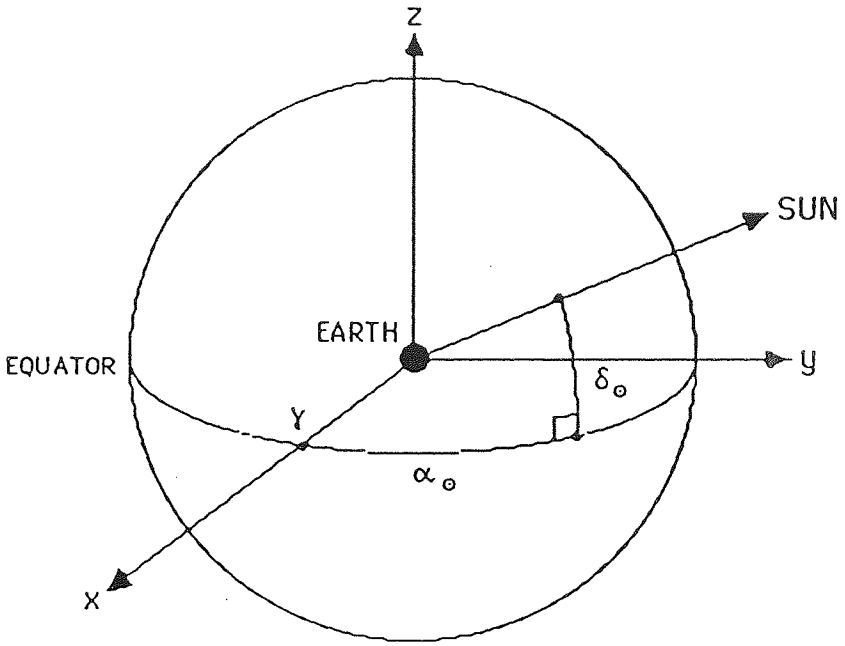

Figure 5.9 The Sun vector in the Earth-centred coordinate system

$$\mathbf{r}_\odot = \begin{bmatrix} \sin\theta_\odot \cos f_\odot \\ \sin\theta_\odot \sin f_\odot \\ \cos\theta_\odot \end{bmatrix} \qquad \ldots\ldots (5.57)$$

which if we rotate the vector (5.56) to the same coordinate system also equals:

$$\mathbf{r}_\odot = \begin{bmatrix} a_1 \\ a_2 \\ a_3 \end{bmatrix} \qquad \ldots\ldots (5.58)$$

where

$$\begin{aligned} a_1 &= \cos\delta_\odot \cos(\alpha_\odot - \Omega)\cos\omega + \cos i \cos\delta_\odot \cos(\alpha_\odot - \Omega)\sin\omega + \sin i \sin\delta_\odot \sin\omega \\ a_2 &= \cos\delta_\odot \cos(\alpha_\odot - \Omega)\cos i \cos\omega + \sin i \sin\delta_\odot \cos\omega - \cos\delta_\odot \cos(\alpha_\odot - \Omega)\sin\omega \\ a_3 &= \sin\delta_\odot \cos i - \sin i \cos\delta_\odot \cos(\alpha_\odot - \Omega). \end{aligned} \qquad \ldots\ldots (5.59)$$

Equating the components of (5.57) with (5.58) we see that

$$\begin{aligned} \cos\theta_\odot &= a_3 \\ \cos f_\odot &= \frac{a_1}{\sin\theta_\odot} \\ \sin f_\odot &= \frac{a_2}{\sin\theta_\odot}. \end{aligned} \qquad \ldots\ldots (5.60)$$

These are sufficient enough to define $\theta_\odot$ and $f_\odot$ which may be used to describe a Sun-oriented flat plate.

5.7 Summary

It is probably economical to form a short overview of the achievements of this chapter. Firstly, Lagranges planetary equations have been adapted to examine their form in terms of an aerodynamic force characterised by a constant tangential momentum accommodation coefficient, and a normal momentum accommodation coefficient that varies with the secant of the angle of incidence. For a flat plate whose normal makes a constant angle θ with the normal to the orbital plane the variations in

a, e and i are given in Equations (5.42), (5.43) and (5.44), where $\phi = f_{\odot} - E$ from Equations (5.39) and (5.40). A method to derive the changes over a single orbital period is demonstrated in Section 5.5.

For a special case of a Sun-oriented flat plate, we simply need to derive expressions for θ and $f_{\odot}$ relevant to such a case. $\theta_{\odot}$ and $f_{\odot}$ may be obtained from a consideration of Equation (5.60). However, in general a flat plate of any orientation may be described through a selection of relevant values of θ and $f_{\odot}$.

In this chapter, we have developed the analysis which will enable us to model the aerodynamics of a satellite in terms of momentum accommodation coefficients. We now require a demonstration on a real orbit to validate the procedure.

CHAPTER 6
AN ANALYSIS OF THE ORBIT OF THE ANS-1 SATELLITE (1974-70A)

6.1 The ANS-1 Satellite

The Astronomical Netherlands Satellite ANS-1 was launched from a Californian base on 30th August 1974 to examine the universe through ultra-violet and X-ray experiments [46]. For this purpose, it was intended to be positioned in a Sun-synchronous circular orbit demonstrating a mean altitude of around 540 km. However, a launch malfunction caused the actual orbit to deviate considerably from its nominal orbit, placing it in an eccentric orbit with a very low perigee height (see Table 6.1).

	Nominal	Actual
a (km)	6913	7098
e	0.0036	0.0640
i (deg)	97.80	98.04
Ω (deg)	241.60	245.10
ω (deg)	167.33	210.89
M (deg)	358.63	320.87
Apogee height (km)	560	1175
Perigee height (km)	510	266

Table 6.1 - Osculating elements at injection of ANS-1 compared to nominal values

In spite of this erroneous orbit, a large portion of the original scientific objectives were achieved. The operational life of ANS-1 was ended on 11th December 1975 and on 14th June 1977 it finally re-entered the atmosphere over the Indonesian archipelago.

A diagram showing the component parts of the ANS-1 satellite, taken from Wakker [46], is given in Figure 6.1. From this, we can see that the main body of the satellite comprises of a rectangular prism densely packed with instrumentation, which we assume was covered by some protective panels. Protruding from opposing sides are two solar panels which are of fixed orientation to the body. The satellite was able

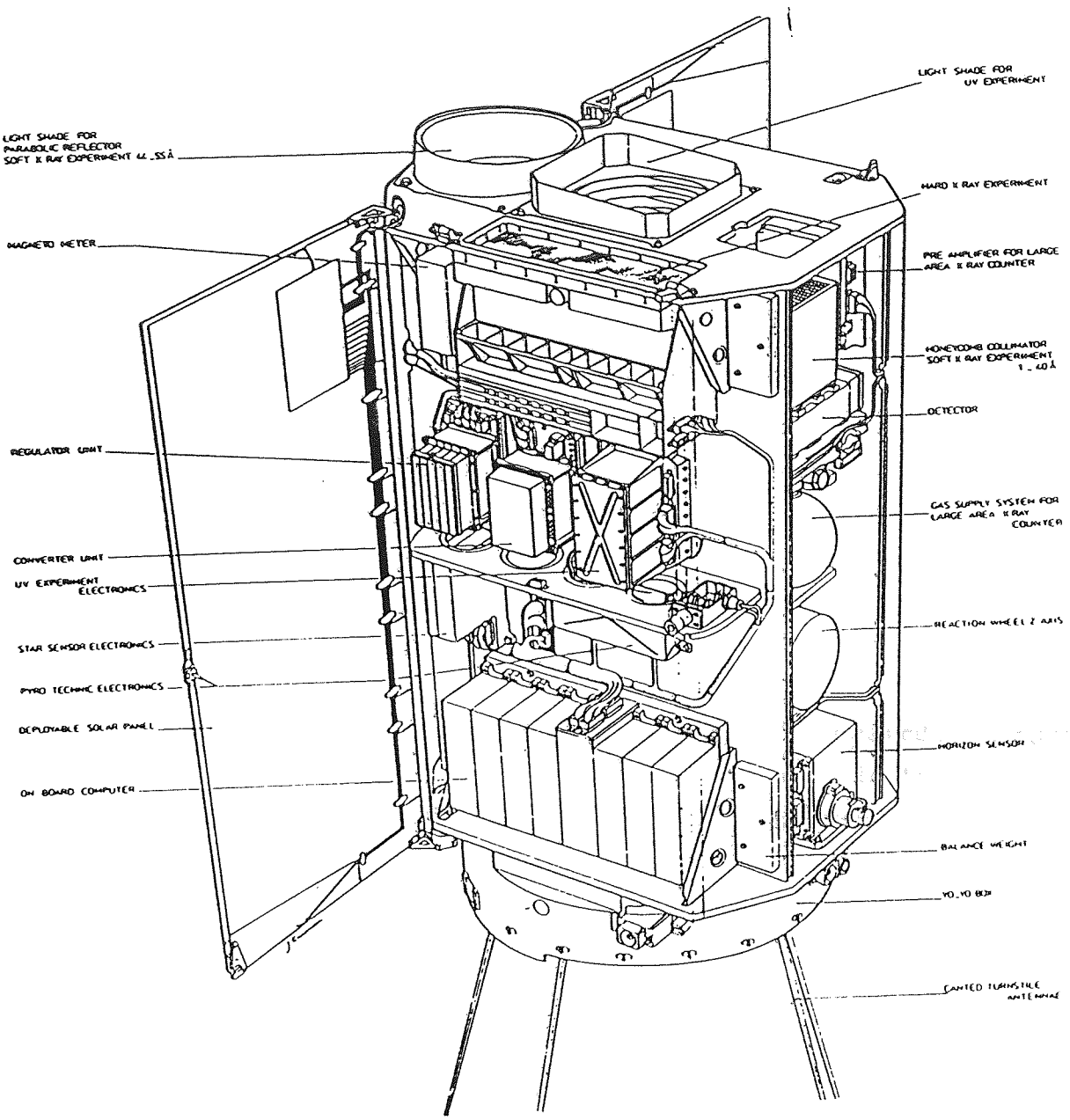

Figure 6.1 the satellite ANS-1 (1974-70A)

to remain Sun-oriented by a method of three-axis stabilisation which helped define the geometry of the telescopes, at right-angles to the Sun direction, enabling the possibility of full sky coverage over a period of one year. ANS-1 weighed a total of 129.6 kg and had dimensions demonstrated in Figure 6.2. From this we can gather that the areas of panels P_1, P_2, P_3, P_4 are

$$\begin{aligned} P_1 &= 0.517 \text{ m}^2 \\ P_2 &= 0.898 \text{ m}^2 \\ P_3 &= 0.750 \text{ m}^2 \\ P_4 &= 0.445 \text{ m}^2 \end{aligned} \qquad \text{..... (6.1)}$$

6.2 The ANS-1 Modelling Geometry

We assume that ANS-1 is composed of a number of plates each oriented to one of three orthogonal directions.

The faces P_1 and P_3 are all oriented in the Sun-direction and, considering also that they have opposing faces not shown in Figure 6.2, we can model them all as a single Sun-oriented flat plate of area $2P_1 + P_3$.

In complete analogy, we may consider that, perpendicular to the Sun direction, are two plates at right angles to one another of area P_2 and P_4.

In some respects this is our model of ANS-1; each of the three plates of areas $2P_1 + P_3$, P_2 and P_4, at right angles to each other, are considered separately in the analysis and simply summed to obtain the final result. The Sun-oriented plate requires very little further analysis as we have already defined its direction by the parameters $\theta_\odot$ and $f_\odot$ given explicitly in Equations (5.55) and (5.72) respectively. Only two problems remain: first, to find the corresponding values of $\theta_\odot$ and $f_\odot$ which will define the orientation of the side panels, and secondly to account for the positive shadowing of a portion of a panel from the atmosphere by other panels.

6.3 Side-Panel Orientation

In terms of the satellite-based coordinate system (Figure 6.3) the Sun direction is given in terms of the angles $\theta_\odot$ and $\phi = f_\odot - E$ (discussed in Section 5.4).

Now by a series of rotations about the axes we can transform the satellite-based coordinate system into one in which the z-axis points along the Sun direction and thus represents the normal to the Sun-oriented panels. This may be achieved by a rotation of $-(\pi/2 - \phi)$ about the z-axis and a rotation of $-\theta_\odot$ about the x-axis, forming a new coordinate system $Ox'y'z'$, shown in Figure 6.4. Also shown are the normals to the remaining two plates $\mathbf{n'_1}$ and $\mathbf{n'_2}$ respectively which will obviously lie in the $x'y'$ plane; we have also shown that the $\mathbf{n'_1}$ vector makes an angle β with the x-axis.

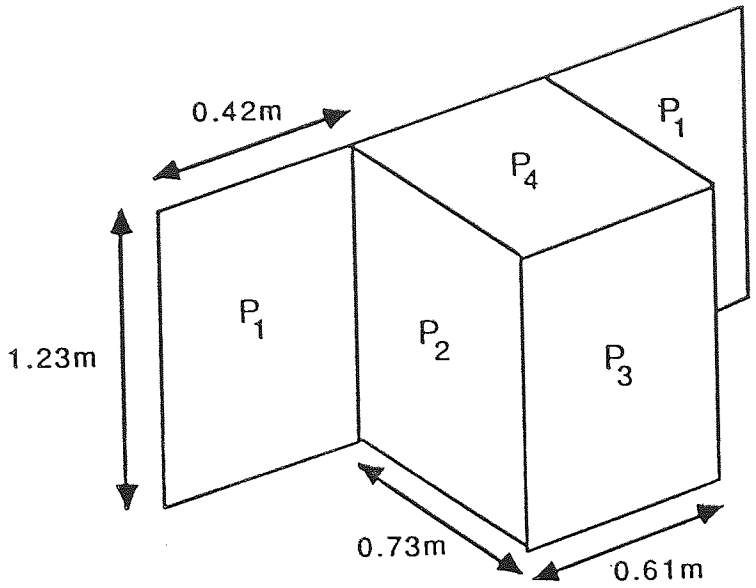

Figure 6.2 The dimensions of ANS-1

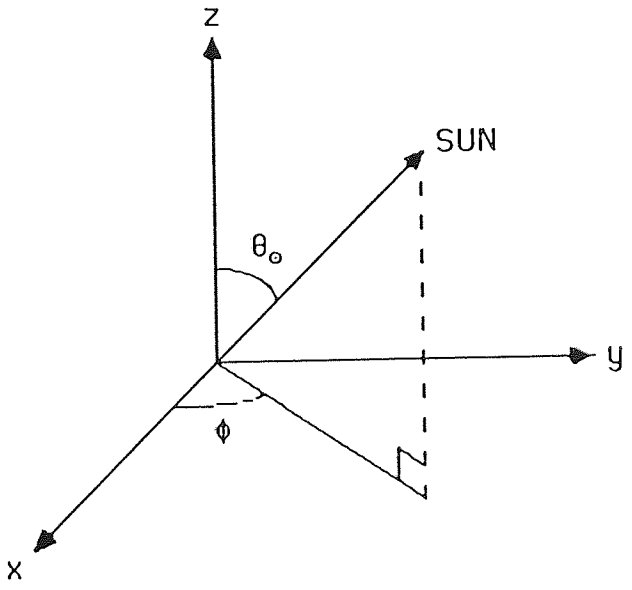

Figure 6.3 The Sun direction in the satellite-based Coordinate system

Thus, in this coordinate system

$$\mathbf{n}'_1 = \begin{bmatrix} \cos\beta \\ \sin\beta \\ 0 \end{bmatrix} \quad ; \quad \mathbf{n}'_2 = \begin{bmatrix} \sin\beta \\ -\cos\beta \\ 0 \end{bmatrix}.$$

Now, we proceed to transform $\mathbf{n}'_1$ and $\mathbf{n}'_2$ back to the satellite-based coordinate system. If we consider $\mathbf{n}'_1$ only for the moment, we find that

$$\mathbf{n}'_1 = \begin{bmatrix} \sin\phi\cos\beta + \cos\phi\cos\theta_\odot\sin\beta \\ -\cos\phi\cos\beta + \sin\phi\cos\theta_\odot\sin\beta \\ -\sin\theta_\odot\sin\beta \end{bmatrix}. \qquad \text{..... (6.1)}$$

Let us, for the moment, assume that $\mathbf{n}'_1$ has the following form in the satellite-based coordinate system

$$\mathbf{n}'_1 = \begin{bmatrix} \sin\theta_1\cos\phi_1 \\ \sin\theta_1\sin\phi_1 \\ \cos\theta_1 \end{bmatrix} \qquad \text{..... (6.2)}$$

where we can see that, in complete analogy with the Sun-oriented plate, θ_1 is the angle $\mathbf{n}'_1$ makes with the normal to the orbital plane and $\phi_1 = f_1 - E$ for some f_1.

By comparison of Equations (6.1) and (6.2) we can quickly see that

$$\cos\theta_1 = -\sin\theta_\odot\sin\beta \qquad \text{..... (6.3)}$$

and from further analysis we find that

$$\sin f_1 = \frac{-\cos f_\odot\cos\beta + \sin f_\odot\cos\theta_\odot\sin\beta}{\sin\theta_1} \qquad \text{..... (6.4)}$$

$$\cos f_1 = \frac{\sin f_\odot\cos\beta + \cos f_\odot\cos\theta_\odot\sin\beta}{\sin\theta_1}.$$

We can proceed to find values for θ_2 and f_2 by setting β to be $\beta - \pi/2$ in Equations (6.3) and (6.4).

6.4 Shadowing

Unfortunately, it would be unrealistic to continue with the analysis as discussed above which treats each panel as an independent entity; this is not the case, as certain portions of the surface will be shadowed from the incident atmosphere simply due

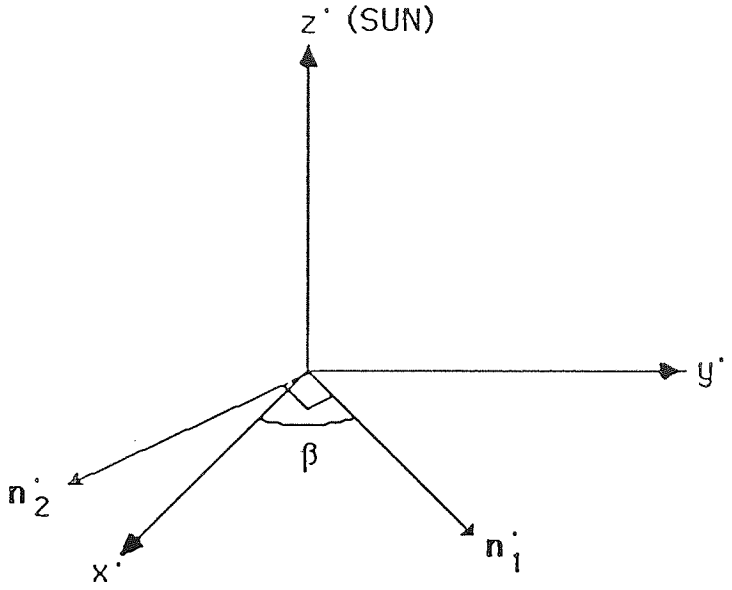

Figure 6.4 The panel-based coordinate system

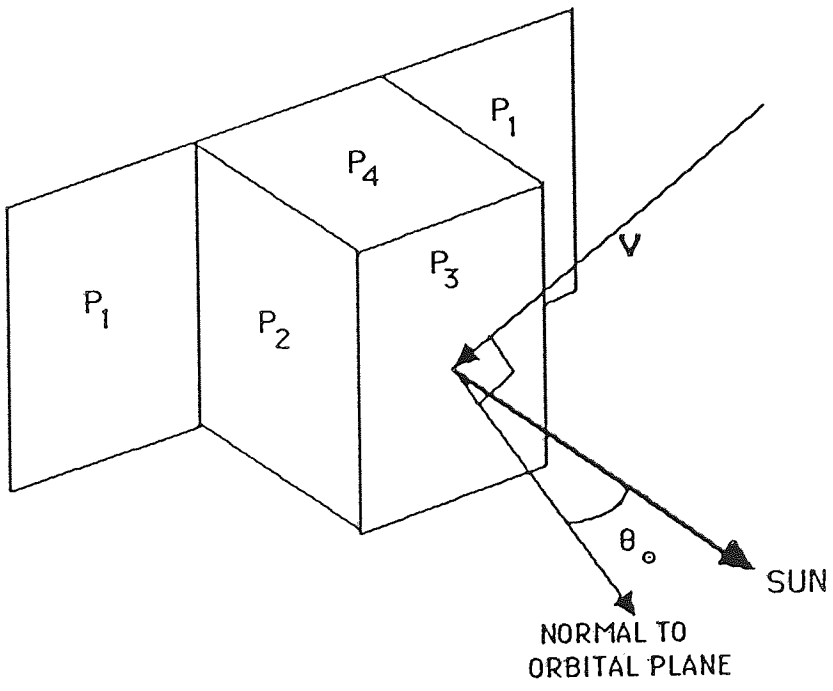

Figure 6.5 ANS-1 face orientation

to the 3-dimensional nature of the satellite. We do not have the attitude information which will allow us to perform a full analysis of the problem and thus some coarse estimation of the problem will be undertaken which will manifest itself in a reduction of the total area of a panel used in our calculations for atmospheric perturbations.

If we consider the shape of the satellite idealised in Figure 6.5, we know that the normal to the Sun-oriented panels makes an angle θ_o with the normal to the orbital plane which is also normal to the velocity vector.

A previous study of ANS-1 by Sehnal [47] has shown that θ_o is never much greater than 20° which suggests that the greatest shadowing is the shadowing of P_1 by P_2, with a small amount of shadowing by P_1 on P_2. Notice that the shadowing only occurs on the two sides of P_1 as shown in Figure 6.5 and not on their reverse faces, whereas shadowing may occur on both P_2 faces.

Consider first the shadowing of P_1 by P_2. This is shown in Figure 6.6 where $L_2 = 123$ cm and $L_1 = 42$ cm.

ϕ_o is the angle of the diagonal, given by

$$\tan\phi_o = \frac{L_2}{L_1}.$$

Now, if $\phi < \phi_o$ the area A shadowed is given by

$$A = L_1 L_2 - \frac{1}{2} L_1^2 \tan\phi$$

and if $\phi \geq \phi_o$

$$A = \frac{1}{2} L_2^2 \cot\phi.$$

Now if we average A over all values of ϕ given by $O \leq \phi \leq \frac{\pi}{2}$, then the mean area shadowed, $\overline{A}$, is given by

$$\overline{A} = \frac{2}{\pi}\left\{ L_1 L_2 \phi_o + \frac{1}{2} L_1^2 \ln(\cos\phi_o) - \frac{1}{2} L_2^2 \ln(\sin\phi_o) \right\} \qquad \text{..... (6.5)}$$

which means that the proportion shadowed is equal to

$$\frac{\overline{A}}{L_1 L_2} = 0.72 \quad \text{for ANS-1}.$$

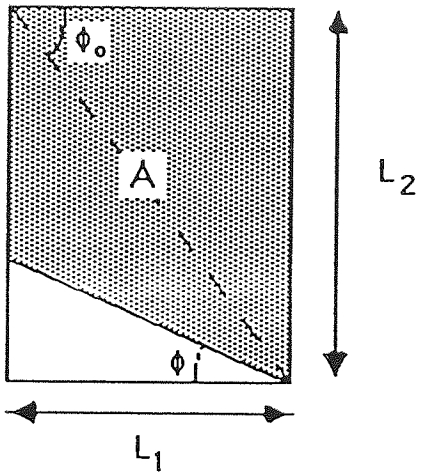

Figure 6.6 The shadowing of P_1

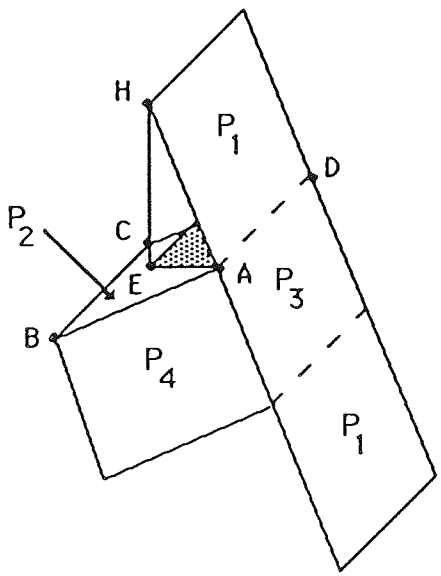

Figure 6.7 Shadowing of P_2 by P_1

The proportion of the Sun-oriented face P_1 represents is approximately 0.29, and we need to halve this as P_1 is only shadowed on one side. If we multiply these values together, this represents a reduction in the total Sun-oriented panel area of around 10%, which is the value used in the analysis.

In analogy with the above, the shadowing of plate P_2 is determined by taking values of L_1 and L_2 appropriate and averaging over the polar angle ϕ. However, we must remember that P_4 is at right angles to the Sun direction which lies very close to the orbital normal, whereas the normals of the P_2 faces have the possibility of falling close to the velocity vector of the satellite, meaning that shadowing may or may not occur depending on orientation and its occurrence may only be over a small portion of the possible area. We will consider that the shadowing of P_2 is due to P_1 and has the geometry shown in Figure 6.7.

How this manifests itself on the P_2 face is shown in Figure 6.8. If we assume that AF is constant, then we may proceed as before. If $\theta_\odot$, the angle between the orbital normal and the Sun direction, is 30° then it may be shown that AF $\leq$ 24 cm and if we use these dimensions we see that the maximum shadowing effect reduces the area by around 13%. However, this is a very extreme case, and in the absence of any further rigorous analysis we reduced the P_2 area by 5% which seems a little more realistic in the absence of detailed orientation parameters.

We have now dealt with the modelling of the satellite, having detailed its orientation in terms of angles $\theta_\odot$, $f_\odot$ and β and reduced the areas of the panels by amounts appropriate to the shadowing effects of shape. The next step in orbital analysis is to clear the orbital elements of effects not attributable to air drag alone.

6.5 Gravitational Perturbations and Resonance

The major gravitational perturbations affecting ANS-1 were removed using the Royal Aircraft Establishment software known as PROD (Program for Orbit Development), the basic theory outlined by Cook [48].

The theory is based on a spherical harmonic representation of a gravitational field. The disturbing function due to a body of Mass M_J at a distance r_J (> r, the distance to the satellite) is given by U, where

$$U = \mu_J \sum_{l=2}^{\infty} \frac{r^l}{r_J^{l+1}} P_l(\cos H) \qquad \text{..... (6.6)}$$

where $\mu_J = GM_J$, $P_l(\cos H)$ is the Legendre polynomial of degree l and H is the geocentric angle between the disturbing body and the satellite. For the analysis of ANS-1, the disturbing bodies were taken to be the Moon and the Sun.

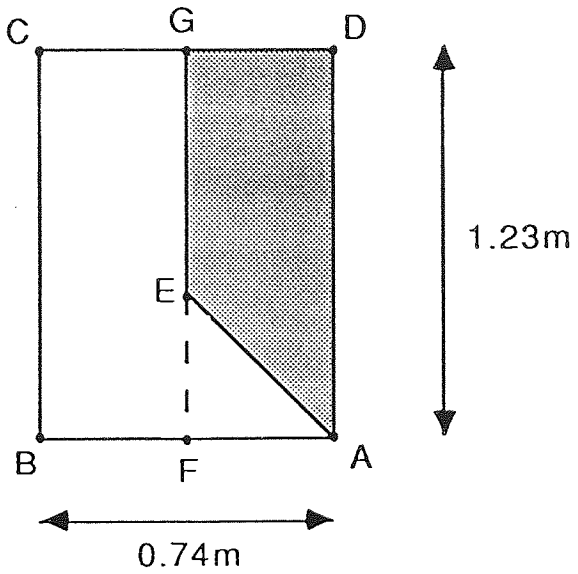

Figure 6.8 P_2 shadowing geometry

There are further perturbations due to the asphericity of the Earth. If we consider that the Earth is a spheroid of revolution and that there are no longitude dependent terms, then the Earth's gravitational potential may be given by

$$U = \frac{\mu}{r}\left\{1 - \sum_{l=2}^{\infty} J_l \left(\frac{R}{r}\right)^l P_l(\sin\phi)\right\} \qquad \text{..... (6.7)}$$

where R is the Earth's equatorial radius, ϕ is the geocentric latitude and the J_l are constants.

The effect that a disturbing potential has on elements a, e and i are described by Lagrange's Planetary Equations in the form below (Smart [49]).

$$\frac{da}{dt} = 2\left(\frac{a}{\mu}\right)^{\frac{1}{2}} \frac{\partial U}{\partial \chi}$$

$$\frac{de}{dt} = \frac{1}{e}\left(\frac{1-e^2}{\mu a}\right)^{\frac{1}{2}}\left[(1-e^2)^{\frac{1}{2}}\frac{\partial U}{\partial \chi} - \frac{\partial U}{\partial \omega}\right] \qquad \text{..... (6.8)}$$

$$\frac{di}{dt} = \{\mu a(1-e^2)\}^{\frac{1}{2}}\left[\cot i \frac{\partial U}{\partial \omega} - \operatorname{cosec} i \frac{\partial U}{\partial \Omega}\right]$$

where χ is the modified mean anomaly.

Applying the above equations to the disturbing potentials of the Earth, Sun and Moon is the function of the PROD software. However, the representation of the Earth's gravitational potential given in (6.7) is highly idealised in that it contains no longitude dependent terms. If we include such terms the potential may be written thus [58]:

$$U = \frac{\mu}{r}\sum_{l=2}^{\infty}\sum_{m=1}^{l}\left(\frac{R}{r}\right)^l P_{lm}(\cos\theta)\{\overline{C}_{lm}\cos m\lambda + \overline{S}_{lm}\sin m\lambda\}N_{lm} \qquad \text{..... (6.9)}$$

where θ is the co-latitude, λ is the longitude, N_{lm} is a normalising coefficient, $\overline{S}_{lm}$ and $\overline{C}_{lm}$ are constants and $P_{lm}(\cos\theta)$ is the associated Legendre function of order m and degree l.

For most of the time the effects of longitude dependence may be neglected. However, if a satellite has a repeating ground track, then the perturbations due to a specific location on the surface of the earth may build up over a number of orbits in a fashion that will not be negligible. Such an effect is known as resonance, the size of which depends on the specific terms in the geopotential involved which in turn are decided by the repeat period.

Now, for a satellite in a low Earth orbit the ground track repeat period will vary in time due to perturbing forces, mainly air drag, and hence will drift through many resonances throughout its lifetime. However, the largest resonant effects occur when the satellite has the shortest repeat period. If a satellite performs β revolutions while the Earth makes α revolutions, where β and α are both co-prime integers, then this is called a β/α resonance. Thus, we would expect a 15/1 resonance to have greater effect than a 29/2 or 31/2 resonance because it takes the former half the time to repeat than the latter two and hence the effects of the gravity anomalies specific to that ground track will build up faster. More important, however, is the diminuation of the gravity field coefficients with the degree l. A working approximation for the magnitude of $\overline{C}_{lm}, \overline{S}_{lm}$ is given by Kaula's rule of thumb [58]

$$\overline{C}_{lm}, \overline{S}_{lm} = 0\left(\frac{10^{-4}}{l^2}\right).$$

Thus, the geopotential coefficients for l = 29 and l = 31 are reduced by a factor of four from the dominant l = 15 resonant coefficients.

If we consider the lifetime of the ANS-1 satellite than we can quickly recognise that it passes through a 15/1 resonance at around MJD 42800. Indeed, if we look at the orbital elements we see that there is an abrupt effect on the inclination at around this time which is only really attributable to resonance. For the semi-major axis and eccentricity there is no noticeable corresponding effect and thus we will discuss resonance as it affects the inclination only.

The mathematics of resonance is discussed in many papers such as that by Allan [50] and is developed from an expansion of the geopotential form given in Equation (6.9) in terms of the Keplerian elements. From a substitution into Lagrange's planetary equations we find that the rate of change of inclination due to the geopotential is given by [51]

$$\frac{di}{dt} = \frac{n(1-e^2)^{\frac{1}{2}}}{\sin i}\sum\left(\frac{R}{a}\right)^l \overline{F}_{lmp} G_{lpq}(k\cos i - m) \qquad \text{..... (6.10)}$$

$$\times \Re[j^{l-m+1}(\overline{C}_{lm} - j\overline{S}_{lm})\exp\{j(\gamma\Phi - q\omega)\}]$$

where $\overline{F}_{lmp}$ is Allan's normalised inclination function, G_{lpq} is a function of eccentricity, $\Re$ denotes "the real part of" and j is the square root of -1. γ, p, k and q are integers, where $\gamma = 1, 2, 3, \ldots$, $q = 0, \pm 1, \pm 2, \ldots$, $m = \gamma\beta$, $k = \gamma\alpha - q$ and $2p = l - k$. Φ is the resonance angle given by

$$\Phi = \alpha(\omega + M) + \beta(\Omega - \upsilon) \qquad \text{..... (6.11)}$$

where υ is the sidereal angle.

For 15/1 resonance Equation (6.10) becomes [59]

$$\frac{di}{dt} = \frac{n}{\sin i}\left(\frac{R}{a}\right)^{15}\{(15-\cos i)\overline{F}_{15,15,7}\{\overline{C}_{15}^{0,1}\sin\Phi - \overline{S}_{15}^{0,1}\cos\Phi\}$$

$$+\frac{17e}{2}(15)\left(\frac{R}{a}\right)\overline{F}_{16,15,8}\{\overline{S}_{15}^{1,0}\sin(\Phi-\omega)+\overline{C}_{15}^{1,0}\cos(\Phi-\omega)\}$$

$$+\frac{13e}{2}(15-2\cos i)\left(\frac{R}{a}\right)\overline{F}_{16,15,7}\{\overline{S}_{15}^{-1,2}\sin(\Phi+\omega)+\overline{C}_{15}^{-1,2}\cos(\Phi+\omega)\}\ ]$$

$$+\text{terms in}\quad\left\{\frac{\left(\frac{1}{2}e\right)^{|q|}}{|q|!}\underset{\sin}{\cos}(\gamma\Phi - q\omega)\right\}, \qquad \text{..... (6.12)}$$

where

$$\overline{C}_m^{q,k} = \sum_l Q_l^{q,k}\overline{C}_{lm} \qquad \text{..... (6.13)}$$

and

$$\overline{S}_m^{q,k} = \sum_l Q_l^{q,k}\overline{S}_{lm} \qquad \text{..... (6.14)}$$

are "lumped" coefficients and in the above equations the $Q_l^{q,k}$ are inclination functions [52] and l increases in steps of 2 from a minimum value l_o.

Now, values of $\overline{C}_{lm}$ and $\overline{S}_{lm}$, or of the lumped harmonics, are crucial in defining Equation (6.12) and estimating the effects of resonance. To estimate this effect for ANS-1, gravity field coefficients were taken from the GEM 10B global model [53], whilst lumped harmonics were available from the satellite-derived coefficients of King-Hele and Walker [54] and from an analysis of ANS-1 itself as given by Klokocnik [55].

Analysis of the resonance effect on the inclination was undertaken using values from the above three sources. Although the results were in broad agreement with a 0.0065 to 0.0083 degree decrease in the inclination over the resonant period, the discrepancy between the results is relatively large in comparison with the likely perturbations due to atmospheric lift. This last point is particularly important given the sensitivity of the results to analysis of the inclination.

Thus, for the ANS-1 satellite we have not considered resonance and have used only values for the inclination that appear unaffected by resonance, i.e. we have analysed inclination up to MJD 42700 which is well before the resonance at around MJD 42800 and hence avoids contamination of the results. Resonance has not been applied to the semi-major axis or eccentricity as it appears to have no noticeable effect and thus we have used all elements up to and including the final values at MJD 42988.

6.6 Atmospheric Rotation

In Chapter 5 we have assumed that the velocity of a satellite relative to the atmosphere is simply the Keplerian velocity of two-body motion given in terms of the orbital elements. This is a false assumption as it ignores the fact that the Earth is a dynamic rotating body and that the atmosphere, to some extent, will adhere to the surface, rotating with the Earth. Also, the addition of zonal and meridional winds will further complicate the analysis causing further variations in the rotation rate with increasing height. The rotation rate of the atmosphere is given by Λ, the ratio of the angular velocity of the atmosphere to that of the Earth. The choice of Λ was taken from King-Hele and Walker [52], and needs to be that appropriate to a height of 3/4 H above perigee. For ANS-1 we took perigee height to be around 260 km and, from an inspection of the COSPAR International Reference Atmosphere 1972 (CIRA 1972) [3], we took H to be around 40 km, which led us to consider values of Λ between 1.10 and 1.15. For the analysis of the orbit of ANS-1 we considered separately the two cases of $\Lambda = 1.10$ and $\Lambda = 1.15$.

Obviously, a full aerodynamic study of a satellite would proceed to adjust the Keplerian velocity component of Chapter 5 by an amount appropriate to a choice of Λ and proceed with the same analysis. However, such a procedure would be highly demanding analytically and, for the purposes of this study, we will take the easier option by using a standard technique to remove atmospheric rotation effects separate from the Keplerian element. The analysis, developed by King-Hele [45], is quite neat and makes as few references to aerodynamic quantities, such as air density and drag coefficients, as possible.

The effect of atmospheric rotation on the a, e and i elements of ANS-1 is negligible, except for inclination where, because of the generally polar orbit, there is an increased drag component in the direction normal to the orbital plane which, from Equation (5.13), we see will perturb it further. The analysis is based on constant drag and lift coefficients over one orbit and involves expansions in increasing powers of c and e. For ANS-1 $c > 0.2$ and $e < 0.2$ and the particular expansion we used appropriate for this case is taken from Boulton and Swinerd [60], and is given by

$$\frac{\Delta i}{\Delta T} = \frac{\Lambda \sin i}{6\sqrt{F}} \cdot \frac{A}{B} \qquad \text{..... (6.15)}$$

where

$$A = [I_0 + I_2(1+c)\cos 2\omega + \frac{1}{2}c(I_0 + I_4\cos 4\omega)$$

$$-2eI_1(1+\cos 2\omega) + \frac{1}{4}c^2(I_0 + \frac{3}{2}I_2\cos 2\omega$$

$$+I_4\cos 4\omega + \frac{1}{2}I_6\cos 6\omega)$$

$$-ce\left\{I_1(1+2\cos 2\omega) + \frac{1}{2}(3I_3 - I_5)\cos 4\omega\right\}$$

$$-\frac{1}{4}c^2e\{2I_1 + 3I_1\cos 2\omega + (3I_3 - I_5)\cos 4\omega$$

$$+(2I_5 - I_7)\cos 6\omega\}] + 0(c^3, e^2),$$

and

$$B = [I_0 + cI_2\cos 2\omega + 2eI_1 + \frac{1}{4}c^2(I_0 + I_4\cos 4\omega)$$

$$+2ceI_3\cos 2\omega + \frac{1}{4}c^2e\{2I_1$$

$$-(I_3 - 3I_5)\cos 4\omega\}] + 0(c^3, e^2).$$

The I_n are the familiar Bessel functions of the first kind and imaginary argument of order n whose argument here is z = ae/H. F is a factor, numerically close to unity, given by

$$\sqrt{F} \sim 1 - \frac{V_A}{V}\cos i$$

where V_A is the rotational velocity of the atmosphere and V is the velocity of the satellite relative to the air.

ΔT is the change in orbital period from orbit to orbit, which may be quantified from the differences in the semi-major axis, and enables us to generate values of Δi with only few real unknowns.

6.7 Solar Radiation Pressure

The remaining perturbation to be considered in satellite dynamics is that caused by the impact of photons from solar radiation on the Sun-oriented surfaces of the orbiting body. This force is primarily important for very large, light satellites. However, ANS-1 is a small dense satellite and thus did not experience any overwhelming solar radiation pressure perturbations. This is borne out by considering a spherical satellite with the same Sun-oriented area-to-mass ratio as ANS-1 of 0.011 m^2/kg (from Sehnal [47]) in software supplied by Asknes, based on his paper of

1976 [56]. For the period from MJD 42290 to MJD 42700, the interval considered for inclination, the values of Δi obtained represents an oscillation of amplitude below 10^{-4} degrees, which is much less than the assumed accuracy of the ESOC data used for this study, which is around 1.5×10^{-3} degrees.

6.8 The Removal of The Known Perturbations of ANS-1

In the absence of any perturbations a satellite will continue in pure Keplerian motion ad infinitum. This means that each of the elements a, e and i will remain at their initial values for the whole period of observation. However, as already discussed, there are many sources of perturbation that will cause a real orbit to deviate from its initial course. It is clear that each of the perturbation sources discussed is independent of the others and their specific effects may simply be added to the rest when modelling the orbit.

Consider a general orbital element a_i. We will denote the initial value of a_i by a_{io} and the amounts by which it is perturbed by $\Delta_{GRAV}\, a_i$, $\Delta_{ROT}\, a_i$ and $\Delta_{DRAG}\, a_i$, corresponding to the perturbations of gravity, atmospheric rotation and the remaining effects of aerodynamic drag and lift, such that the observed value of a_i is given by

$$a_i = a_{io} + \Delta_{GRAV} a_i + \Delta_{ROT} a_i + \Delta_{DRAG} a_i$$

The remainder of this study is concerned solely with $\Delta_{DRAG}\, a_i$ and, assuming that the modelled perturbations of gravity and atmospheric rotation are accurate enough, this may be determined by

$$\Delta_{DRAG} a_i = a_i - a_{io} - \Delta_{GRAV} a_i - \Delta_{ROT} a_i .$$

The form of these equations for a, e and i are, respectively,

$$\Delta_{DRAG} a = a - a_o$$

$$\Delta_{DRAG} e = e - e_o - \Delta_{GRAV} e$$

$$\Delta_{DRAG} i = i - i_o - \Delta_{GRAV} i - \Delta_{ROT} i$$

where we have assumed that $\Delta_{GRAV}\, a$, $\Delta_{ROT}\, a$ and $\Delta_{ROT}\, e$ are negligible.

Thus, given adequate values of a_o, e_o and i_o we are able to proceed with an analysis of the aerodynamic drag and lift forces on ANS-1.

6.9 The Analysis of ANS-1

The first step in the analysis of the orbit of ANS-1 was the subtraction of each of the perturbative effects of the aforementioned sources from the orbital elements supplied to us by ESOC. The residual variations in a, e and i are then solely due to the aerodynamics of the satellite's motion through the upper atmosphere. We could then use the analysis of Chapter 5 to model this force and to derive values for the momentum accommodation coefficients in terms of the unknown constants σ, σ'_0 and

σ'_1. Only a single obstacle remains - the determination of the atmospheric density, ρ_0, at perigee which must be taken from one of the many thermospheric models that are available.

In deciding which density model to use, we must recognise that the lifetime of ANS-1 coincided with a minimum in the so-called 11-year cycle of solar activity, which is one of the major influences on thermospheric density. Models such as the DTM or the 1979 model derived from mass spectrometer and incoherent scatter measurements (MSIS79) used data from periods of moderate solar activity and so their use for ANS-1 would be questionable, particularly when a more comprehensive model by Jacchia, 1977, known as J77, has been developed from data spread over almost two solar cycles. J77 does differ from the DTM and MSIS79 models at the minimum but the later MSIS models of MSIS83 and MSIS86 appear to confirm the J77 model. Thus, in this study we have used the J77 model in the derivation of perigee density values. The importance of an accurate density model is illustrated by the equation for the change in inclination over a single orbit for the simple case of a circular orbit (e = 0) in a spherically symmetric atmosphere, which is

$$\Delta i = \rho_0 a A_m \sin\theta\cos\theta\sin(\omega + E_0) \times \left[\sigma'_1 \pi - \frac{8}{3}(2 - \sigma - \sigma'_0)\sin\theta \right]. \quad \text{..... (6.16)}$$

If a scale error occurs in the density component then, due to the presence of a term within σ, σ'_0 or σ'_1, the least squares adjustment will occur in a non-uniform manner on our three derived quantities causing any inferences about gas-surface interactions to be questionable.

A major problem in the numerical evaluation of Δi, Δa and Δe from Equations (5.42), (5.43) and (5.44) lay in their expansion after integration and reduction to a form that could be included in a computer program. To perform this function by hand would have been a considerable effort, particularly when the size of the equations necessitated many routine trigonometry and integration procedures, which would almost always amount in errors in the manual case. In these circumstances we were very pleased to be introduced to the automatic algebraic manipulation computer package REDUCE which could cope with large expressions and perform a comprehensive range of simple tasks from reductions and expansions to substitution and floating point arithmetic, converting the final expression to a form that could be directly pasted into a FORTRAN program.

The operator tasks were performed interactively and involved a simple statement of the task in terms of a series of operations to be performed on the expression. For instance, if we take Equation (5.42), given by

$$\frac{da}{dE} = -2\rho a^2 A_m (1 + 2e\cos E)[\sigma'_1 \sin^2\theta \,.\, \sin^2\phi$$

$$+ \varepsilon \sin\theta \sin\phi + \varepsilon(2 - \sigma'_0 - \sigma)\sin^3\theta \sin^3\phi]$$

as the starting point for the process (which was invariably the case) we can list the functions to be performed on it to find Δa in an efficient programmable form.

These were:

1. Let $\rho = \rho_p k_1 e^{2\cos E}[1 + c\cos 2(\omega + E)$

   $$-2ce\sin 2(\omega + E)\sin E + \frac{1}{4}c^2\{1 + \cos 4(\omega + E)\}]$$

   from Equation (5.21), and $\phi = f_\odot - E$ from Equations (5.39) and (5.40).

2. Use a series of trigonometric operations to expand $\frac{da}{dE}$ in order to determine the multiples of sin n E and cos n E, where n = 0, 1, 2, ...

3. Perform $\Delta a = \int_0^{2\pi} \frac{da}{dE} dE$.

   This was achieved by simply converting the cos n E and sin n E terms to Bessel functions and the C_n and S_n functions (see Appendix A), using the following scheme

   $\cos nE e^{z\cos E}$ becomes $2\pi I_n(z)$

   $\sin nE e^{z\cos E}$ becomes 0

   $\varepsilon\cos nE e^{z\cos E}$ becomes $2\pi[I_n(z) - C_n(z, f_A)]$

   $\varepsilon\sin nE e^{z\cos E}$ becomes $-2\pi S_n(z, f_A)$

   which was outlined in Section 5.5. Any terms with no E component were multiplied by 2π.

4. Use the difference equations

   $2_n I_n + z(I_{n+1} - I_{n-1}) = 0$

   $2_n C_n + z(C_{n+1} - C_{n-1}) = 2\phi_n$

   $2_n S_n + z(S_{n+1} - S_{n-1}) = -2\psi_n$

   to reduce the expression to include only I_0, I_1, C_0, C_1, S_1 and S_2 terms, where

   $$\phi_n = \frac{-\sin nf_\odot}{\pi}\left[e^{z\cos f_\odot} - (-1)^n e^{-z\cos f_\odot}\right]$$

   and

$$\Psi_n = \frac{-\cos nf_\odot}{\pi}\left[e^{z\cos f_\odot} - (-1)^n e^{-z\cos f_\odot}\right]$$

from Appendix A.

5. Convert to FORTRAN code

Thus, using this method, we could find the values of Δa. In fact Δi and Δe were found using the same process.

To illustrate the usefulness of REDUCE, it must be stated that the final reduced expression for Δa took up 120 lines of code, for Δi this was 117 lines and Δe took up 164 lines. The program that utilises these expressions will calculate Δa_i in the form

$$\Delta a_i = x_0 + x_1\sigma + x_2\sigma'_0 + x_3\sigma'_1 \qquad \text{..... (6.17)}$$

finding numerical values for x_0, x_1, x_2 and x_3. Δa_i is equal to the $\Delta_{DRAG}\, a_i$ found by the subtraction of the known perturbations and the initial value by the method explained in Section 5.8. The main output of the analysis are values of σ, σ'_0 and σ'_1, determined by a least squares regression in Equation (6.17).

The values of x_0, x_1, x_2 and x_3 are determined for each of the three orthogonal plates, corresponding to the Sun-oriented plate and the two side panels, the orientation of the side-panels being determined by β defined in Section 6.3. As we have no knowledge of its numerical value we have simply taken values for β of 0°, 30°, 60°, 90°, 120° and 150°, averaging the results. No greater values of β were used due to the rotational symmetry of the satellite geometry. Thus, addition of the effects for each panel in turn will give the total aerodynamic perturbation of ANS-1, from which we may determine values for the three unknown parameters σ, σ'_0 and σ'_1.

Although we consider J77 to be the most representative density model, we will also reproduce the numerical results of the MSIS79 model for comparison.

6.9.1 Analysis of Inclination

Due to the analytic form of the Δi Equation (5.42) it is impossible to derive separate numerical values for σ, σ'_0 and σ'_1 due to the fact that there are only two terms in the equation and three unknowns. This is illustrated by reproducing Equation (5.42) below where we can see a term in σ'_1 and a term in $2-\sigma'_0-\sigma$.

$$\frac{di}{dE} = -\rho a A_m (1 + e\cos E)\{\cos(\omega + E) - e\cos\omega\} \times$$

$$\times [\sigma'_1 \sin\theta \,.\, \cos\theta \,.\, \sin\phi + \varepsilon(2 - \sigma'_0 - \sigma)\sin^2\theta\cos\theta\sin^2\phi].$$

Therefore, we solved the numerical results for σ'_1, $2-\sigma'_0-\sigma$ and a linear shift in the original inclination value of Δi_o from MJD 42290 to MJD 42700.

For the J77 air density model, the results were, using $\Lambda = 1.10$

		Correlation Coefficients		
	Least Squares Results	$2-\sigma'_0-\sigma$	σ'_1	Δi_o
$2-\sigma'_0-\sigma$	-0.04 ± 0.07	-	-	-
σ'_1	0.17 ± 0.01	0.62	-	-
Δi_o	$1.26 \times 10^{-3} \pm 1.6 \times 10^{-4}$	-0.64	-0.16	-

Table 6.2 - Inclination Results using J77 Density Model and $\Lambda = 1.10$

The corresponding results using $\Lambda = 1.15$ are shown in Table 6.3.

		Correlation Coefficients		
	Least Squares Results	$2-\sigma'_0-\sigma$	σ'_1	Δi_o
$2-\sigma'_0-\sigma$	-0.13 ± 0.07	-	-	-
σ'_1	0.17 ± 0.01	0.62	-	-
Δi_o	$1.44 \times 10^{-3} \pm 1.6 \times 10^{-4}$	-0.64	-0.16	-

Table 6.3 - Inclination Results Using J77 Density Model and $\Lambda = 1.15$

Graphs of the above results showing the fit against the observed values are shown in Figures 6.9 and 6.10. The graphs show quite obviously that the fitted curve does not seem to be an ideal fit although it does demonstrate the general behaviour quite well. There are numerous reasons that may account for this. Firstly, we have assumed that the solar panels are always pointing in the Sun direction. As Wakker [46] pointed out, this may not always have been the case as it was relaxed occasionally to achieve the mission objectives.

Attitude is difficult to approximate for ANS-1 and so our assumptions about side-panel orientation, manifestly in the terms of the angle β, may also be erroneous.

Sehnal [47] recognised the difficulties in obtaining a good fit for ANS-1 when he attempted an aerodynamic analysis using Schambergs model based on a constant thermal energy accommodation coefficient, α. He found that if he allowed α to increase linearly from 0.1 at MJD 42290 to 1.0 at MJD 42550 a better fit could be obtained. However, due to the uncertainties in how α varies with angle of incidence and the accuracy of the ESOC data we find it difficult to interpret his results.

Despite difficulties in interpreting the graphical results, the numerical results present us with no difficulties at the moment as, currently, they do not seem unreasonable enough to reject. The test of these results comes in comparison with the results from the analysis of the semi-major axis and eccentricity.

For comparison the numerical results for inclination using the MSIS79 density model are presented in Tables 6.4 and 6.5.

		Correlation Coefficients		
	Least Squares Results	$2-\sigma'_0-\sigma$	σ'_1	Δi_o
$2-\sigma'_0-\sigma$	-0.08 ± 0.06	-	-	-
σ'_1	0.15 ± 0.01	0.58	-	-
Δi_o	$1.36 \times 10^{-3} \pm 1.5 \times 10^{-4}$	-0.60	-0.05	-

Table 6.4 - Inclination Results Using MSIS79 Density Model and $\Lambda = 1.10$

		Correlation Coefficients		
	Least Squares Results	$2-\sigma'_0-\sigma$	σ'_1	Δi_o
$2-\sigma'_0-\sigma$	-0.15 ± 0.06	-	-	-
σ'_1	0.15 ± 0.01	0.58	-	-
Δi_o	$1.55 \times 10^{-3} \pm 1.5 \times 10^{-4}$	-0.60	-0.05	-

Table 6.5 - Inclination Results Using MSIS79 Density Model and $\Lambda = 1.15$

Figure 6.9 The orbital inclination of ANS-1 cleared of zonal harmonics, atmospheric rotation and luni-solar gravitational effects with theoretical fit (continuous curve) using J77 density model and Λ=1.10

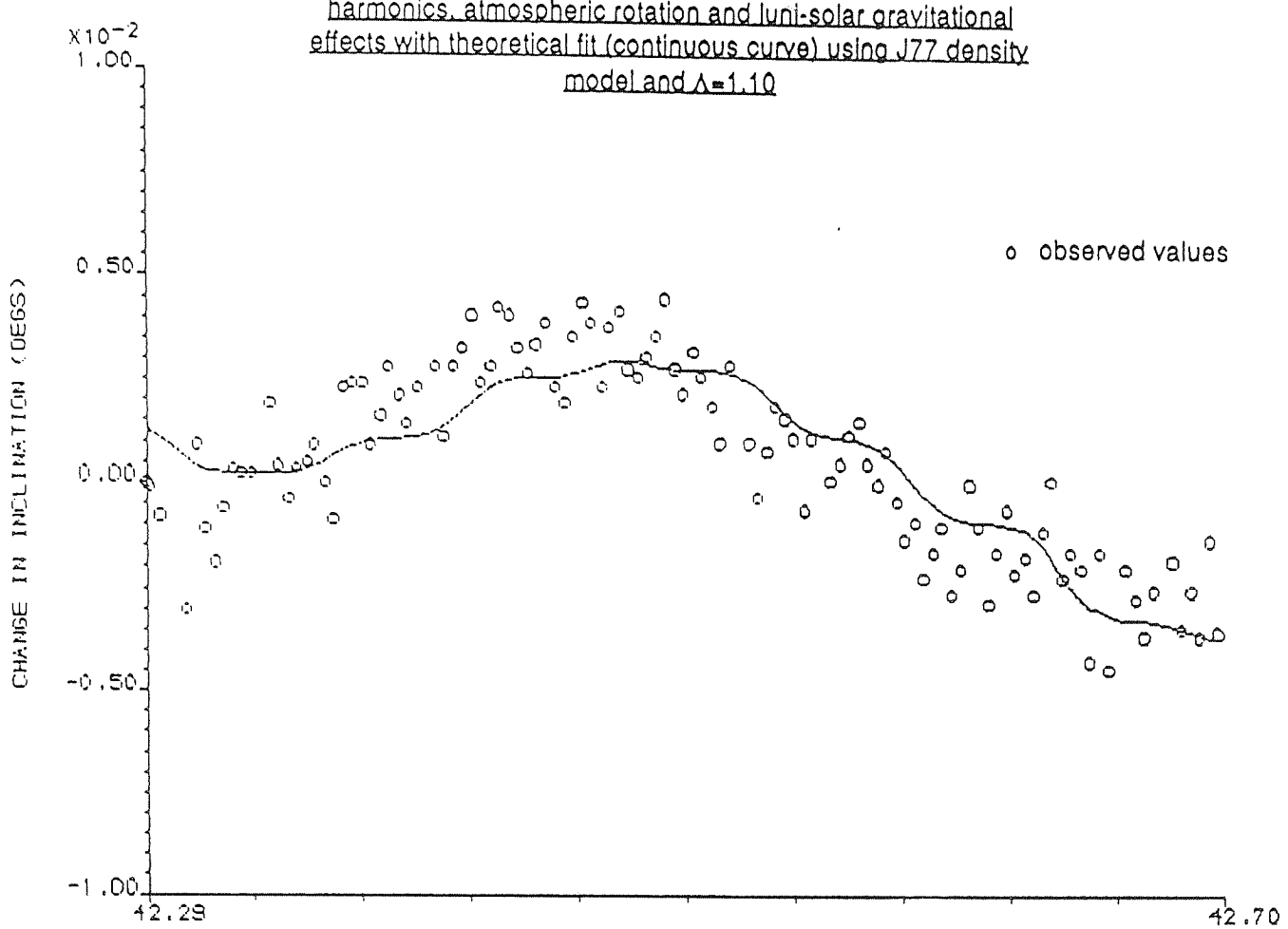

Figure 6.10 The orbital inclination of ANS-1 cleared of zonal harmonics, atmospheric rotation and luni-solar gravitational effects with theoretical fit (continuous curve) using J77 density model and Λ=1.15

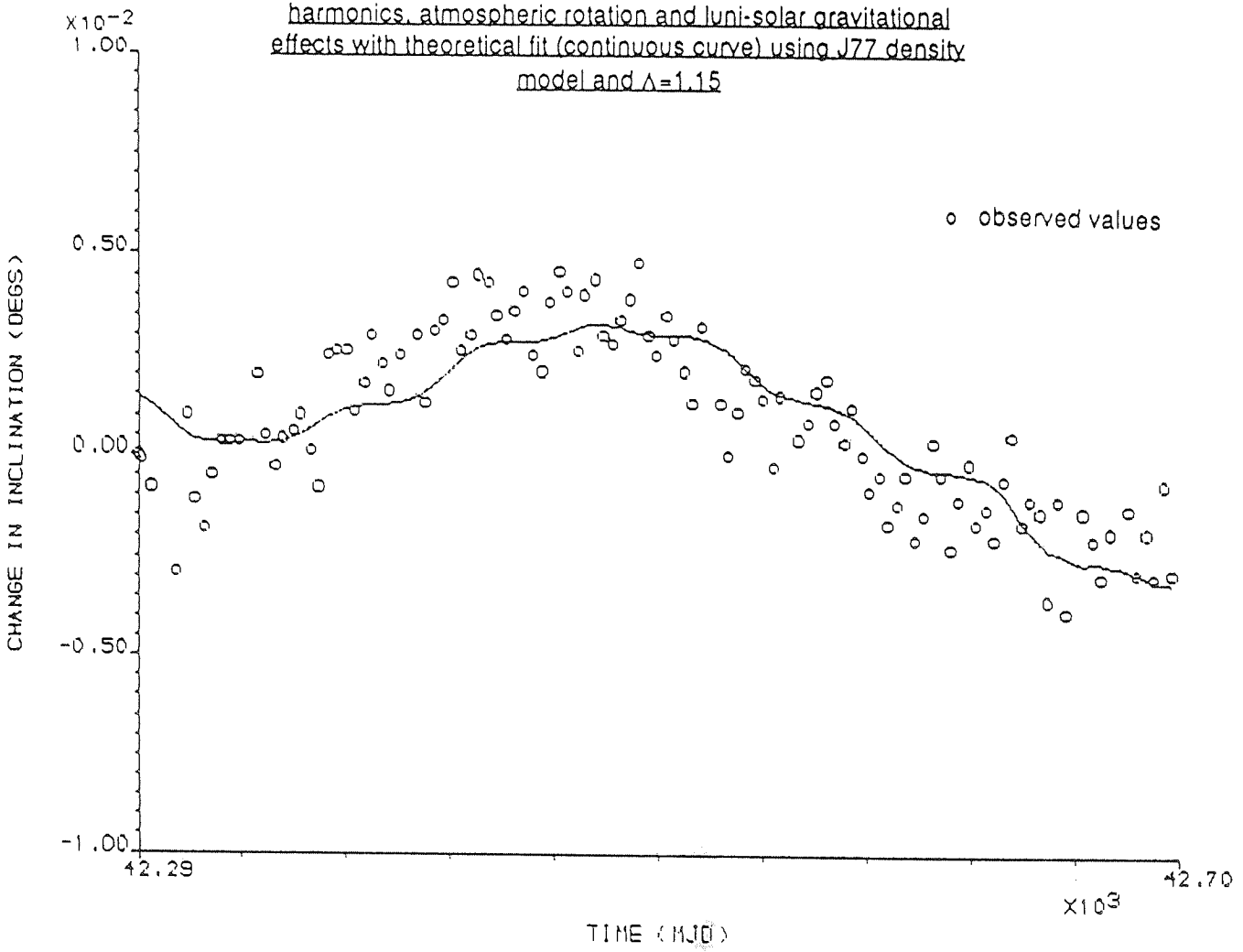

6.9.2 Analysis of Semi-Major Axis

The perturbation of the semi-major axis by aerodynamics was shown to be given in Equation (5.42) by

$$\frac{da}{dE} = 2\rho a^2 A_m (1 + 2e\cos E)[\sigma'_1 \sin^2\theta \sin^2\phi$$

$$+ \varepsilon\sigma \sin\theta \,.\, \sin\phi + \varepsilon(2 - \sigma'_0 - \sigma)\sin^3\theta \sin^3\phi].$$

Unlike the case for the inclination of ANS-1 the structure of the above equation allows us the possibility of solving separately for σ, σ'_0 and σ'_1. The results of the least squares fit using J77 gave three equations in σ, σ'_0 and σ'_1 for us to solve, given here in matrix form as

$$\begin{bmatrix} 1.0000 & -1.1781 & 1.6865 \\ 1.0000 & -1.1798 & 1.6882 \\ 1.0000 & -1.1793 & 1.6878 \end{bmatrix} \begin{bmatrix} \sigma \\ \sigma'_0 \\ \sigma'_1 \end{bmatrix} = \begin{bmatrix} -0.0887 \\ -0.0895 \\ -0.0888 \end{bmatrix}.$$

We can clearly see that, numerically, these three equations are almost the same and that the 3 x 3 matrix on the left will be almost singular. In fact if we follow the least squares procedure through we find very high correlation coefficients between the parameters, making the analysis highly suspect.

In order to derive a meaningful result from this we have tried to approximate the equation satisfied by σ, σ'_0 and σ'_1 simply by averaging the columns of the matrices. For the J77 case this equation is given by

$$\sigma - 1.1791\sigma'_0 + 1.6875\sigma'_1 = -0.0890.$$

On its own, this equation is meaningless. However, it is of a form for which we can use the inclination results of $2 - \sigma'_0 - \sigma$ and σ'_1 to solve for σ'_0 and σ. The results for the J77 density model and $\Lambda = 1.10$ are

$$\sigma = 0.93 \pm 0.04 \quad , \quad \sigma'_0 = 1.11 \pm 0.03 \quad , \quad \sigma'_1 = 0.17 \pm 0.01.$$

The results for the J77 density model using $\Lambda = 1.15$ are

$$\sigma = 0.98 \pm 0.04 \quad , \quad \sigma'_0 = 1.15 \pm 0.03 \quad , \quad \sigma'_1 = 0.17 \pm 0.01.$$

The graphs of the semi-major axis for each of the above cases are shown in Figures 6.11 and 6.12.

For the MSIS79 density model the equation from the analysis of the semi-major axis is

$$\sigma - 1.218\sigma'_0 + 1.733\sigma'_1 = -0.603$$

and combining with the MSIS79 inclination results we find, for $\Lambda = 1.10$,

$$\sigma = 0.75 \pm 0.03 \quad , \quad \sigma'_0 = 1.33 \pm 0.03 \quad , \quad \sigma'_1 = 0.15 \pm 0.01$$

and for $\Lambda = 1.15$

$$\sigma = 0.79 \pm 0.03 \quad , \quad \sigma'_0 = 1.36 \pm 0.03 \quad , \quad \sigma'_1 = 0.15 \pm 0.01.$$

Note here that, at a normal incidence angle ($\xi_i = 0$) $\sigma' > 1$ for MSIS79 which is clearly unacceptable.

6.9.3 Analysis of Eccentricity

The perturbations of the eccentricity due to aerodynamics is given in Equation (5.43), as

$$\begin{aligned}\frac{de}{dE} = -\rho a A_m [&\sigma'_1 \sin^2\theta \{2(1 + e\cos E)\cos E \sin^2\phi \\ &+ \sin E \sin\phi\cos\phi\} \\ &+ \varepsilon(2 - \sigma'_0 - \sigma)\sin^3\theta\{2(1 + e\cos E)\cos E \sin^3\phi \\ &+ \sin E \sin^2\phi\cos\phi\} \\ &+ 2\varepsilon\sigma \sin\theta(1 + e\cos E)\cos E \sin\phi].\end{aligned}$$

The form of this equation leads us to understand that we can solve for each of the coefficients σ, σ'_0 and σ'_1. However, in complete analogy with the semi-major axis case, the correlation coefficients are too high to be able to perform the least squares fit adequately and so we must proceed to find the most representative equation for the matrices involved.

For the J77 density model the equation from the analysis of eccentricity is

$$\sigma - 1.184\sigma'_0 + 1.609\sigma'_1 = -0.217$$

and combining with the J77 inclination results we find, for $\Lambda = 1.10$,

$$\sigma = 0.88 \pm 0.04 \quad , \quad \sigma'_0 = 1.16 \pm 0.03 \quad , \quad \sigma'_1 = 0.17 \pm 0.01$$

and for $\Lambda = 1.15$,

$$\sigma = 0.93 \pm 0.04 \quad , \quad \sigma'_0 = 1.20 \pm 0.03 \quad , \quad \sigma'_1 = 0.17 \pm 0.01.$$

The graphs showing the results of the above two cases are shown in Figures 6.13 and 6.14.

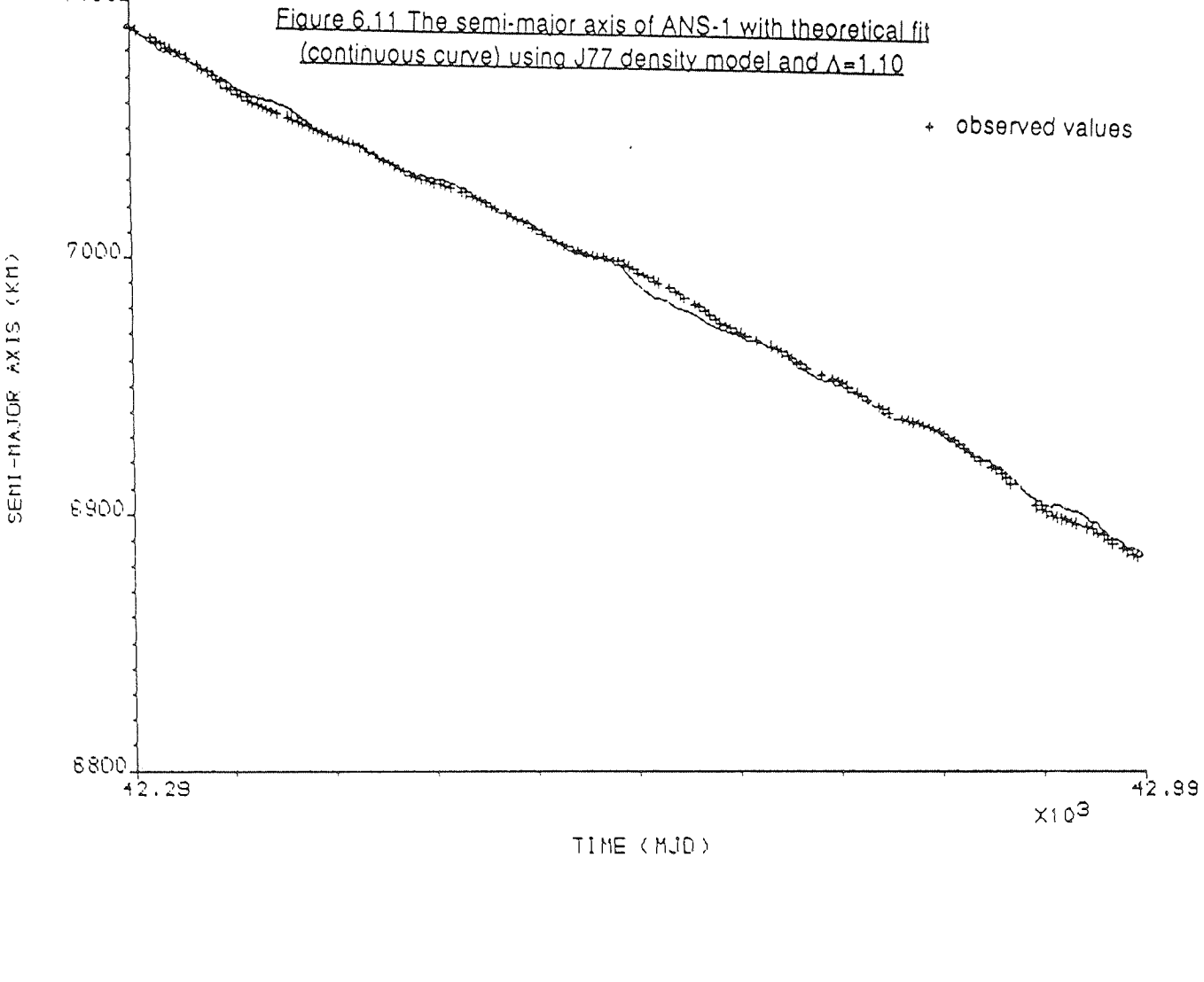

Figure 6.11 The semi-major axis of ANS-1 with theoretical fit (continuous curve) using J77 density model and Λ=1.10

Figure 6.12 The semi-major axis of ANS-1 with theoretical fit (continuous curve) using J77 density model and Λ=1.15

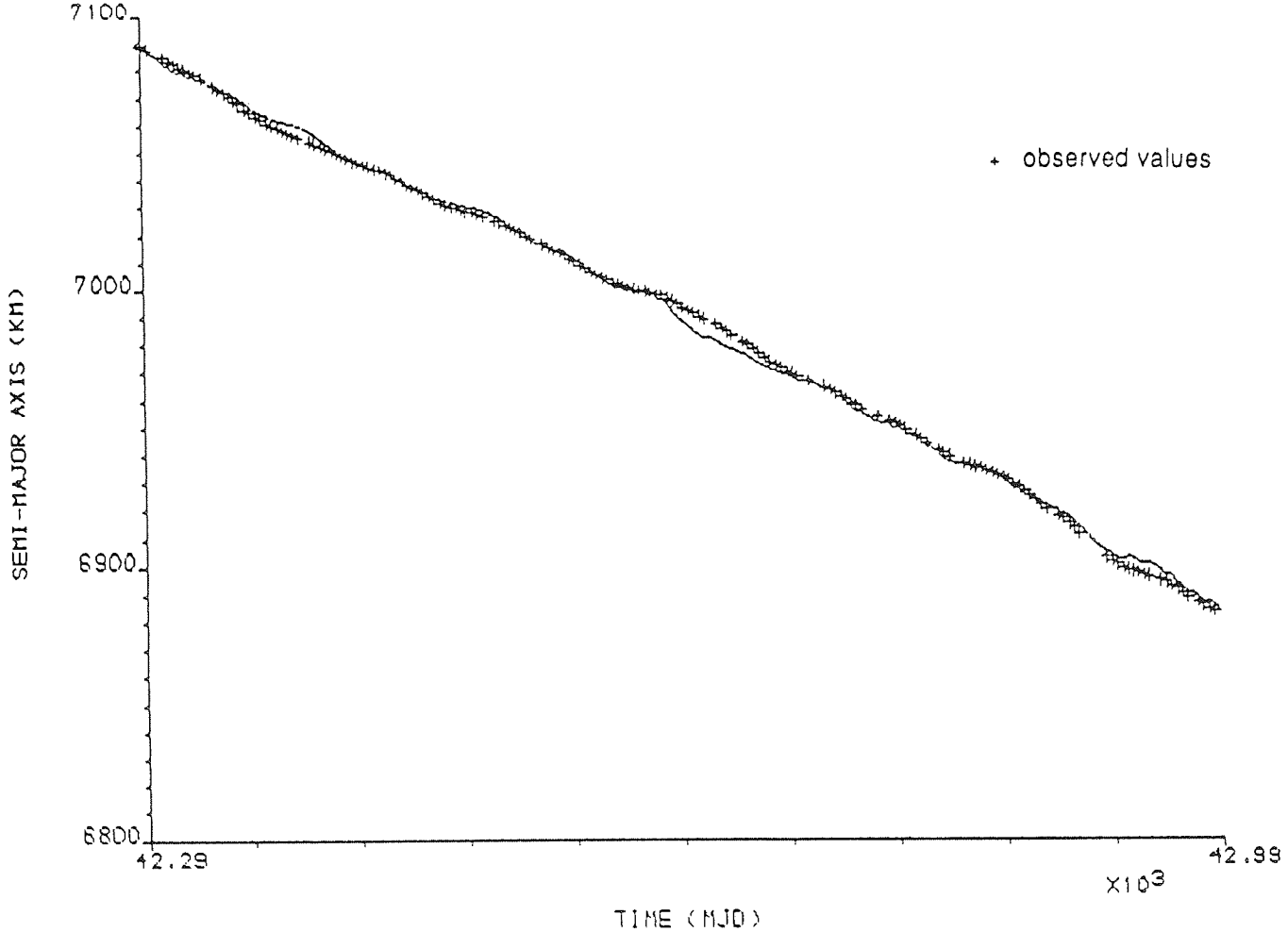

Notice that the results do not differ significantly from the results combining the semi-major axis and the inclination, which does show some uniformity of the analysis.

For the MSIS79 density model the equation from the analysis of eccentricity is

$$\sigma - 1.230\sigma'_0 + 1.659\sigma'_1 = -0.714$$

and combining with the MSIS79 inclination results, we find, for $\Lambda = 1.10$,

$$\sigma = 0.72 \pm 0.03 \quad , \quad \sigma'_0 = 1.36 \pm 0.03 \quad , \quad \sigma'_1 = 0.15 \pm 0.01$$

and for $\Lambda = 1.15$,

$$\sigma = 0.75 \pm 0.03 \quad , \quad \sigma'_0 = 1.40 \pm 0.03 \quad , \quad \sigma'_1 = 0.15 \pm 0.01.$$

Figure 6.13 The eccentricity of ANS-1 cleared of zonal harmonics and luni-solar gravitational effects with theoretical fit (continuous curve) using J77 density model and $\Lambda = 1.10$

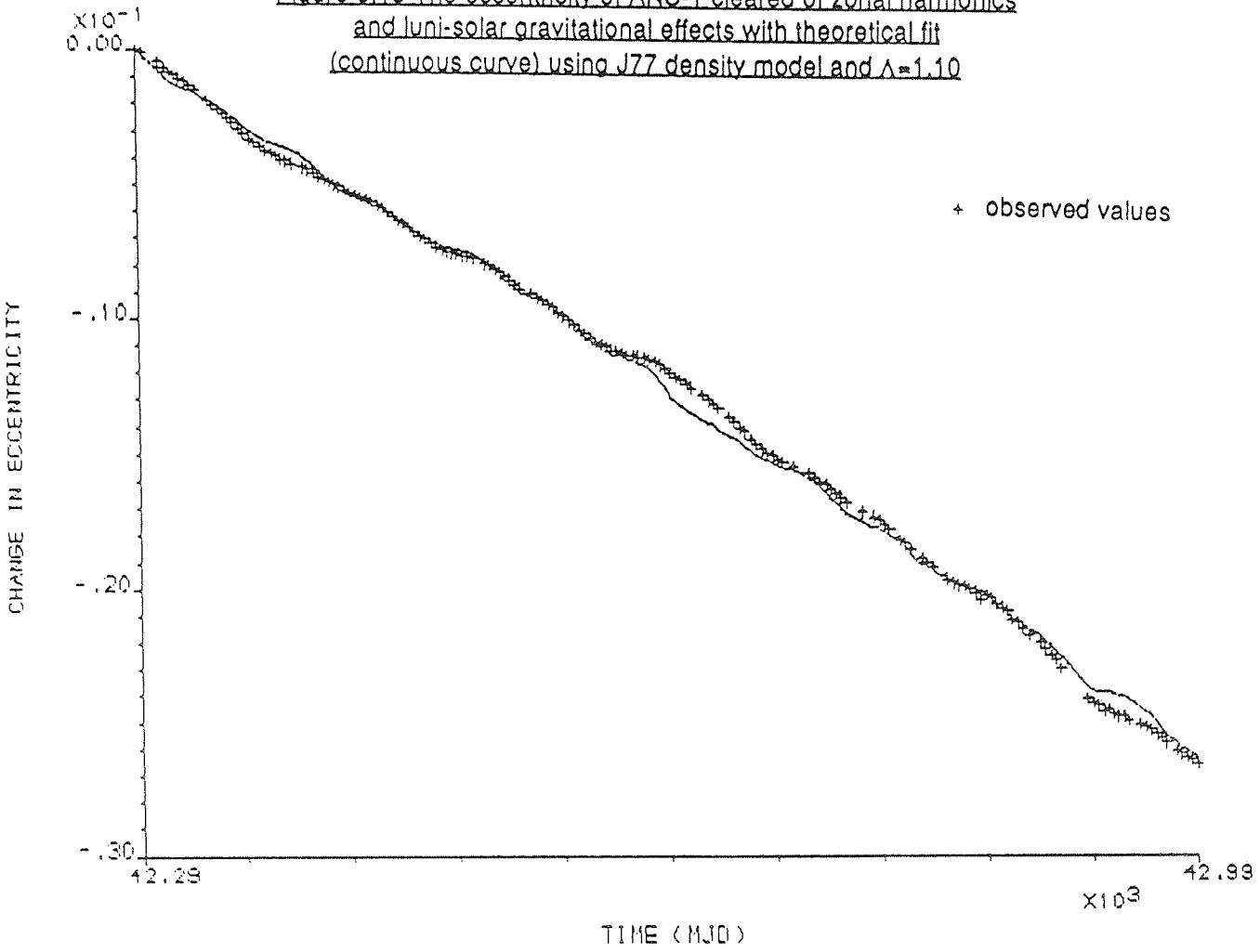

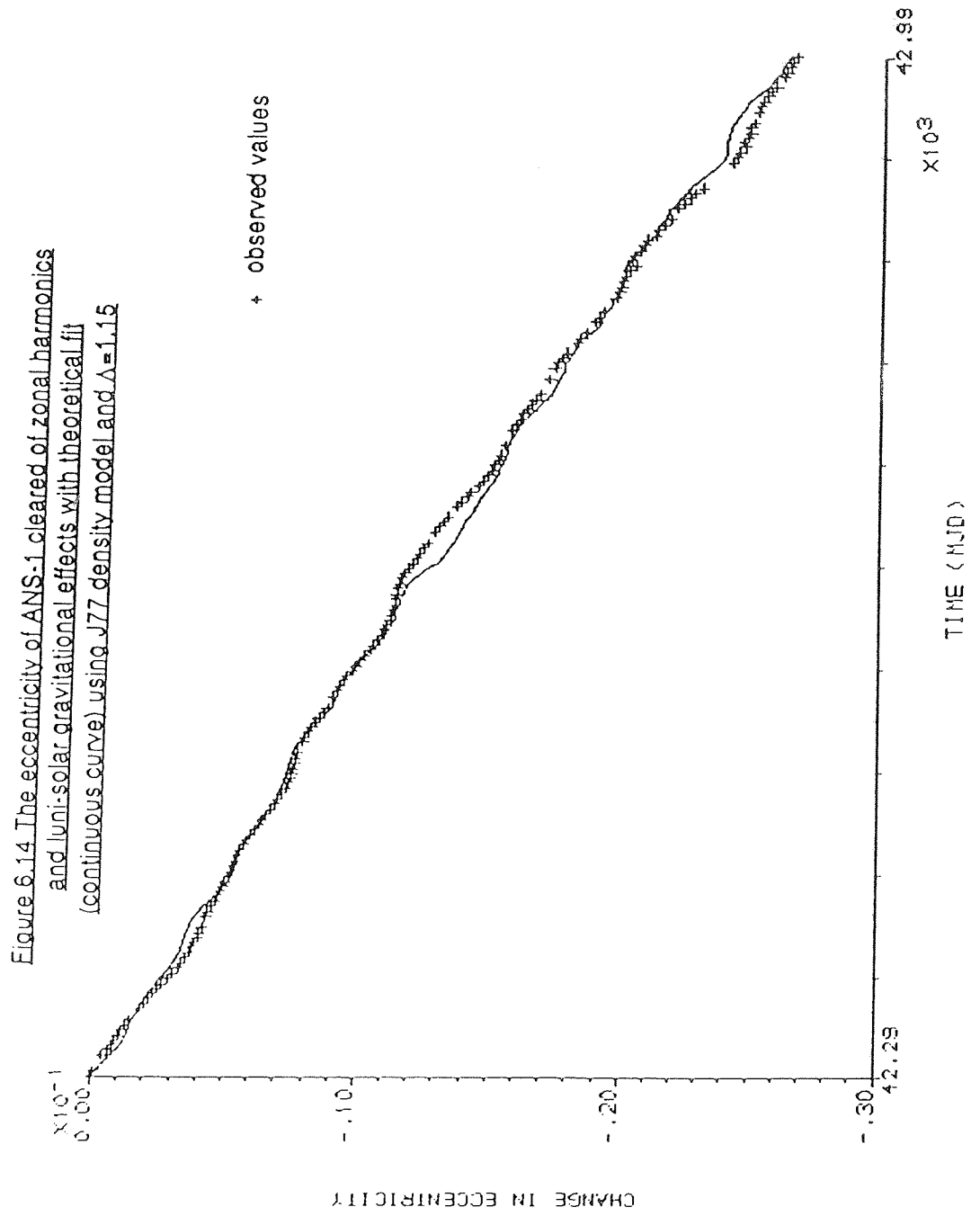

Figure 6.14 The eccentricity of ANS-1 cleared of zonal harmonics and luni-solar gravitational effects with theoretical fit (continuous curve) using J77 density model and Λ=1.15

CHAPTER 7
CONCLUSIONS

Throughout this thesis we have attempted to describe the aerodynamics of a satellite in a way that agrees with the accepted conventions of rarefied gas dynamics and surface science. There is a strong incentive in this, due to the fact that existing equations in rarefied gas dynamics allow a greater generalisation of the problem allowing an analysis that includes transitional flow such as anticipated at lower altitudes right up to re-entry. Up to now this has hardly been possible due to the restrictions of the mathematical models of satellite drag forces. A large portion of this thesis has been spent trying to develop a new model for the gas-surface interaction that allows this generalisation.

In Chapters 2 and 3 a full review of the relevant models available has been attempted. This has shown the deficiencies in current models and parameterisations of satellite drag and has consistently underlined the potentials behind adopting a scheme based on momentum accommodation coefficients. Experimental results on the behaviour of such parameters have been summarised and compared with the most acceptable model of the mechanics of such a scheme, that of Goodman.

Goodman's model was shown to be consistently in quantitative disagreement with experiment, particularly in predicting momentum transfer tangential to the surface. In Chapter 4 we attempted to correct this discrepancy by creating a new numerical model of the scenario, but with different models of the surface that enabled a degree of roughness superlative to that of Goodman's. The results, however, did not sufficiently improve on those already existing which restricted the remainder of the thesis to a quantitative analysis of the behaviour of momentum transfer at the surface of a satellite without the inferences on atmospheric composition and surface roughness desirable.

This has been the first occasion that momentum accommodation coefficients in the form

$$\sigma = const$$

$$\sigma' = \sigma'_0 - \sigma'_1 \sec \xi_i$$

have been used to theoretically predict the aerodynamics of satellite motion. The theory has been developed in Chapter 5 and applied to the orbit of ANS-1 in Chapter 6. The question to be raised in this chapter is whether the results have been successful, firstly in terms of the order of fit with the orbital elements and, secondly, if the values of σ, σ'_0 and σ'_1 found for ANS-1 are feasible for gas-surface interaction.

As far as the orbital fit is concerned, we have to study the graphs of Figures 6.9-6.14 in order to see if they are, visually, good fits. For each of the curves shown it is clear that the theoretical values show most of the general behaviour of the observed values and therefore display a good fit. This is certainly true for the semi-major axis and eccentricity

results and, even in the presence of many possible errors, the widely scattered observed values of inclination bear resemblance to the theoretical fit in qualitative terms and so we have little reason to reject the fit.

The numerical results for the momentum accommodation coefficients were necessarily restricted by the results of the inclination fit. The final results for the J77 density model were, using $\Lambda = 1.10$,

$$\sigma = 0.93$$

$$\sigma' = 1.11 - 0.17 \sec \xi_i$$

for the semi-major axis, and

$$\sigma = 0.88$$

$$\sigma' = 1.16 - 0.17 \sec \xi_i$$

for the eccentricity. The first of these results is illustrated in Figure 7.1.

The semi-major axis values used on a spherical body would produce a drag coefficient of

$$C_{D_{\text{SPHERE}}} \sim 2.05 \pm 0.03$$

which is less than 10% lower than the minimum values set by Cook [14, 22] using Schamberg's [12] model.

If the results are reasonable for the orbital elements and for gas-surface interactions, how may we interpret the use of this model in the future? One of the driving forces behind this thesis was to somehow relate the work of the rarefied gas dynamicist and surface analyst to the orbital dynamicist. Adopting earlier models of satellite aerodynamics, such as Schambergs, and, in particular, using the thermal energy accommodation coefficient, confines the range of relevant gas dynamics to hyperthermal free-molecular flow. Using momentum accommodation coefficients does not confine us to this and results can be better related to theoretical and laboratory studies. Also, given that the quasi-diffuse model used by Schamberg is exactly the equivalent of using

$$\sigma' = 1 - \frac{2}{3}(1-\alpha)^{\frac{1}{2}} \sec \xi_i$$

$$\sigma = 1$$

from Equation (2.39), we cannot say that the method recommended here diverges much from accepted practice anyway.

In the past, laboratory simulations of gas-surface interaction have been rejected simply because they have produced drag coefficients that are lower than the minimum values set by Cook. The results of this thesis show that this may have been an erroneous

criterion for rejecting the experiments as we have shown that, given the levels of uncertainty in much of the modelling and the data involved, a good theoretical fit may be achieved using drag coefficients closer to the laboratory results.

The results of this thesis have shown that a satellite aerodynamic model based on momentum accommodation coefficients is possible and desirable due to their wide acceptance by the gas dynamics and surface science fraternity.

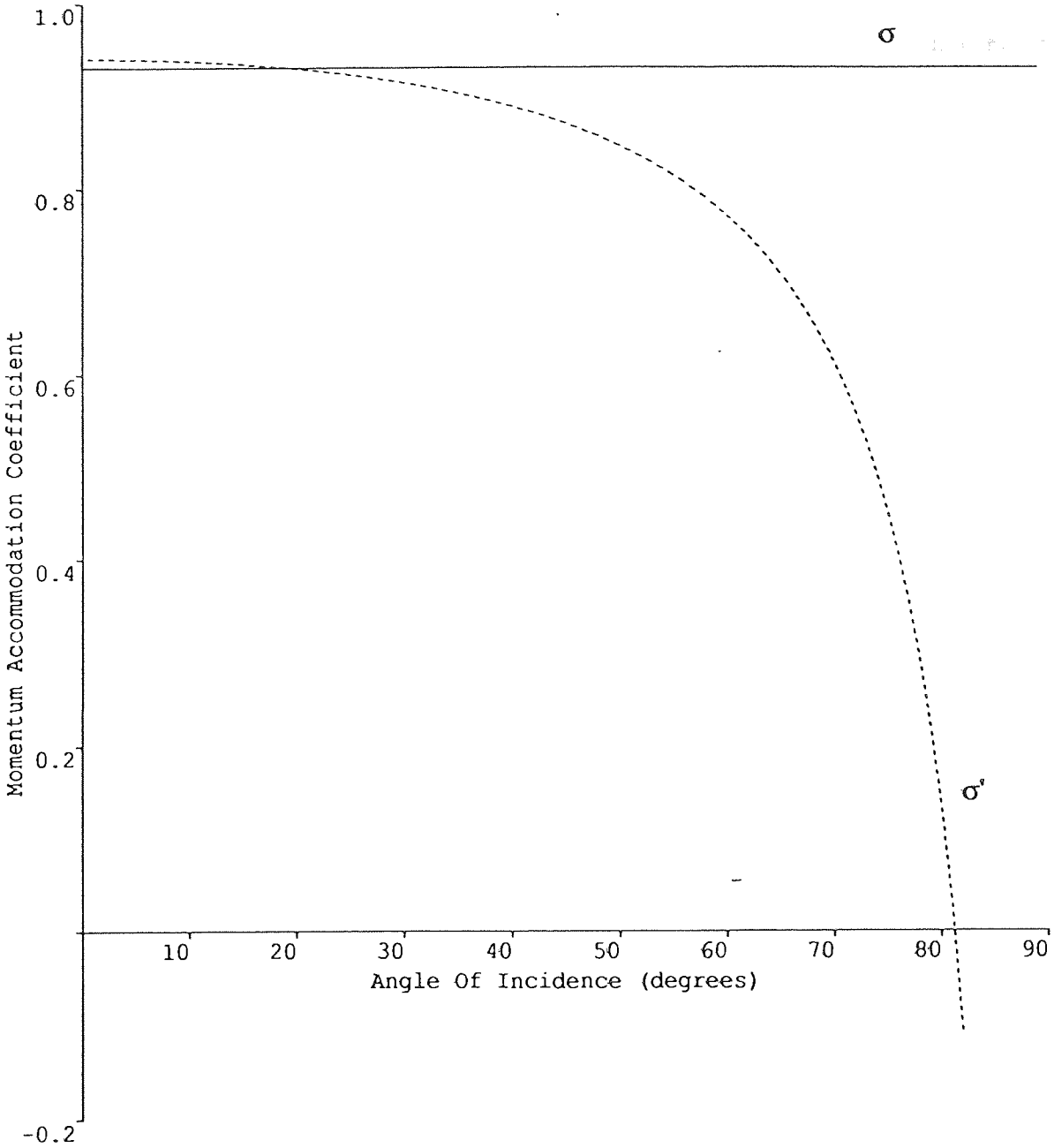

Figure 7.1 Graph showing σ and σ' behaviour from analysis of ANS-1

8 REFERENCES

1. Hargreaves, J.K., "The Upper Atmosphere and Solar-Terrestrial Relations", Van Nostrand Reinhold, 1979.
2. Chamberlain, J.W. and Hunter, D.M., "Theory of Planetary Atmospheres", Academic Press, 1987.
3. COSPAR Working Group 4, "COSPAR International Reference Atmosphere 1972", Akademie-Verlag, Berlin, 1972.
4. Boettcher, R.D., Koppenwallner, G. and Legge, H., ESA Journal, 4, p 357, 1980.
5. Shidlovskiy, V.P., "Introduction to the Dynamics of Rarefied Gases", American Elsevier Publishing Co. Inc., New York, 1967.
6. Bird, G.A., "Molecular Gas Dynamics", Clarendon Press, Oxford, 1976.
7. Cercignani, C., "Theory and Application of the Boltzmann Equation", Scottish Academic Press, 1975.
8. Maxwell, J.C., "The Scientific Papers of James Clerk Maxwell", Vol. 2, Cambridge University Press, 1980.
9. Schaaf, S.A. and Chambré, P.L., "Flow of Rarefied Gases", in "High Speed Aerodynamics and Jet Propulsion, Volume II, Fundamentals of Gas Dynamics", Oxford University Press, 1958.
10. Smoluchowski, M.V., Wied. Ann., 64, p 100, 1898.
11. Knudsen, M., Ann. Phys., 34, p 593, 1911.
12. Schamberg, R., Rand Corporation Report RM-2313, 1959.
13. Nocilla, S., Proceedings of the First International Symposium on Rarefied Gas Dynamics, 1963.
14. Cook, G.E., Annales de Geophysique, 22, p 53, 1966.
15. Goodman, F.O., in "The Structure and Chemistry of Solid Surfaces", ed. G. Somorjai, Wiley, New York, 1969.
16. Goodman, F.O., Surface Science, 26, p 327, 1971.
17. Calia, V.S. and Oman, R.A., J. Chem. Phys., 52, p 1684, 1970.
18. Romney, M.J. and Anderson, J.B., J. Chem. Phys., 51, p 2490, 1969.
19. Miller, D.R. and Subbarao, R.B., J. Chem. Phys., 52, p 425, 1970.
20. Hurlbut, F.C., RAND Report 339, 21-1, 1959.
21. Kogan, M.N., "Rarefied Gas Dynamics", Trans. Ed. L. Trilling, Plenum Press, New York, 1969.
22. Cook, G.E., Planetary and Space Science, 13, p 929, 1965.
23. Karr, G.R., University of Illinois Report R-435 (Ph.D Thesis), 1969.
24. Hurlbut, F.C. and Sherman, F.S., The Physics of Fluids, 11, p 486, 1968.
25. Tully, J.C., Ann. Rev. Phys. Chem., 31, p 319, 1980.
26. Oman, R.A., J. Chem. Phys., 48, p 3919, 1968.

27. Baule, B., Ann. Phys., 44, p 145, 1914.
28. Oman, R.A., Grumman Research Dept. Report RE-222, 1965.
29. Oman, R.A., Bogan, A. and Li, C.H., Proc. of the Fourth Int. Symp. on Rarefied Gas Dynamics, 1964.
30. Goodman, F.O., Surf. Sci., 7, p 391, 1967.
31. Goodman, F.O., NASA Report CR-933, 1967.
32. Millikan, R.A., Phys. Rev., 21, p 217, 1923.
33. Thomas, L.B. and Lord, R.G., Proc. Eighth Int. Symp. on Rarefied Gas Dynamics, 1974.
34. Steinheil, E., Scherber, M., Seidl, M. and Rieger, H., Proc. Tenth Int. Symp. on Rarefied Gas Dynamics, 1976.
35. Seidl, M. and Steinheil, E., in "Rarefied Gas Dynamics", ed. Becker and Fiebig, Vol. II, DFVLR-Press, Parc-Wahn, Germany, 1974.
36. Knechtel, E.D. and Pitts, W.C., in "Rarefied Gas Dynamics", ed. Trilling and Wachman, Vol. II, Academic Press, New York, 1969.
37. Doughty, R.O. and Schaetzle, W.J., as in Ref. 36.
38. Lui, S.M., Sharma, P.K. and Knuth, E.L., AIAA J., 17, p 1314, 1979.
39. Boring, J.W. and Humphris, R.R., AIAA J., 8, p 998, 1970.
40. Lord, R.G., Proc. Tenth Int. Symp. on Rarefied Gas Dynamics, 1976.
41. Moskal, E.J., University of Toronto Institute for Aerospace Studies, Toronto, UTIAS Rept. 166, 1971.
42. Knuth, E.L., AIAA J., 18, p 602, 1980.
43. Steinbruchel, C., Surf. Sci., 115, p 247, 1982.
44. Logan, R.M. and Stickney, R.E., J. Chem. Phys., 44, p 195, 1966.
45. King-Hele, D., "Satellite Orbits in an Atmosphere: Theory and Applications", Blackie, 1987.
46. Wakker, K.F., J. Brit. Interplanetary Soc., 31, p 387, 1978.
47. Sehnal, L., Bull. Astron. Inst. Czechosl., 33, p 244, 1982.
48. Cook, G.E., Celestial Mech., 7, p 301, 1972.
49. Smart, W.M., "Celestial Mechanics", Longmans, 1953.
50. Allan, R.R., Plan. Space Sci., 21, p 205, 1973.
51. King-Hele, D.G., Proc. Roy. Soc. A., 375, p 327, 1981.
52. King-Hele, D.G. and Walker, D.M.C., Proc. Roy. Soc. A., 379, p 247, 1982.
53. Lerch, F.J., Putney, B.H., Wagner, C.A. and Klosko, S.M., Marine Geodesy, 5, p 145, 1981.
54. King-Hele, D.G. and Walker, D.M.C., Plan. Space Sci., 35, p 79, 1987.
55. Klokocnik, J., Bull, Astron, Inst. Czechosl., 33, p 259, 1987.
56. Aksnes, K., Celestial Mech., 13, p 89, 1976.

57. Karr, G.R., NASA Report CR-2765, 1976.
58. Kaula, W.M., "Theory of Satellite Geodesy", Blaisdell Publishing Co., 1966.
59. Walker, D.M.C., Plan. Space Sci., 33, p 97, 1985.
60. Boulton, W.J. and Swinerd, G.G., Proc. R. Soc. Lond. A., 386, p 55, 1983.
61. Visentine, J.T., Leger, L.J., Kuminecz, J.F. and Spiker, I.K., AIAA 23rd Aerospace Sciences Meeting, Paper 85-0415-CP, 1985.

9 APPENDIX - SPECIAL FUNCTIONS

i) The Function $C_n(z, f_\odot)$

Let us define the function $C_n(z, f_\odot)$ by

$$C_n(z,f_\odot)=\frac{1}{\pi}\int_{f_\odot}^{f_\odot+\pi}\cos nE\,.\,e^{z\cos E}\,\mathrm{dE}\quad n=0,1,2,\ldots \qquad \text{..... (A1)}$$

The main recurrence relation for C_n is

$$2_nC_n+z(C_{n+1}-C_{n-1})=2\phi_n \qquad \text{..... (A2)}$$

where

$$\phi_n=-\frac{\sin nf_\odot}{\pi}\left[e^{z\cos f_\odot}-(-1)^n e^{-z\cos f_\odot}\right] \qquad \text{..... (A3)}$$

To initialise this equation, C_0 and C_1 have to be evaluated numerically.

If we adopt the notation $C'_n=\frac{\partial C_n}{\partial z}$, then

$$2C'_n=C_{n+1}+C_{n-1} \qquad \text{..... (A4)}$$

$$zC_{n-1}=zC'_n+nC_n-\phi_n \qquad \text{..... (A5)}$$

and

$$zC_{n+1}=zC'_n-nC_n+\phi_n \qquad \text{..... (A6)}$$

Thus, further manipulation shows that C_n satisfies the partial-differential equation

$$z(zC'_n)'-(n^2+z^2)C_n=z\phi_{n+1}-n\phi_n-z\phi'_n \qquad \text{..... (A7)}$$

Notice that, where $f_\odot = 0$, $C_n = I_n$, the modified Bessel function, which satisfies the O.D.E.

$$z(zI'_n)'-(n^2+z^2)I_n=0 \qquad \text{..... (A8)}$$

which is, thus, a complementary solution of Equation (7).

Expanding C_n as a Fourier Series, we find that

$$C_n(z, f_\odot) = I_n(z) - \sum_{r=1}^{\infty} \frac{[1-(-1)^r]}{r\pi} [I_{n+r}(z) + I_{n-r}(z)] \sin r f_\odot \qquad \text{..... (A9)}$$

ii) The Function $S_n(z, f_\odot)$

Let us define the function $S_n(z, f_\odot)$ by

$$S_n(z, f_\odot) = \frac{1}{\pi} \int_{f_\odot}^{f_\odot + \pi} \sin nE\, e^{z \cos E}\, dE \qquad n = 1, 2, \ldots \qquad \text{..... (A10)}$$

which satisfies the main recurrence relation

$$2_n S_n + z(S_{n+1} - S_{n-1}) = -2\psi_n \qquad \text{..... (A11)}$$

where

$$\psi_n = -\frac{\cos n f_\odot}{\pi} \left[e^{z \cos f_\odot} - (-1)^n e^{-z \cos f_\odot} \right]$$

This can be initialised to find general S_n by using

$$S_1 = \frac{2}{\pi z} \sinh(z \cos f_\odot) \quad \text{and} \quad S_2 = \frac{2}{z} \left[\frac{2}{\pi z} z \cos f_\odot \cosh(z \cos f_\odot) - S_1 \right]$$

Thus, we see that S_n differs from C_n only in the form of the function ϕ_n. Hence S_n satisfies the P.D.E.

$$z(zS'_n)' - (n^2 + z^2) S_n = -z\psi_n + n\psi_n + z\psi'_n \qquad \text{..... (A12)}$$

As a Fourier Series:

$$S_n(z, f_\odot) = -\sum_{r=1}^{\infty} \frac{1-(-1)^r}{r\pi} [I_{n+r}(z) - I_{n-r}(z)] \cos r f_\odot \qquad \text{..... (A13)}$$